

Structure-based modelling and dynamics of MurM, a *Streptococcus pneumoniae* penicillin resistance determinant that functions at the cytoplasmic membrane interface

Anna York^{a1,4*}, Adrian. J. Lloyd^{a1,4*}, Charo I. del Genio^{2b}, Jonathan Shearer^{3e}, Karen. J. Hinxman^{1a}, Konstantin Fritz^{1a}, Vilmos Fulop^{1a}, Christopher. G. Dowson^{1a}, Syma Khalid^{3e**}, David. I. Roper^{1,5a**}

^{1a}School of Life Science, University of Warwick, Coventry, West Midlands, CV4 7AL, U.K;

^{2b}Centre for Fluid and Complex Systems, School of Computing, Electronics and Mathematics, University of Coventry, West Midlands, CV1 5FB, U.K;

^{3e}School of Chemistry, University of Southampton, Southampton, Hampshire, SO17 1BJ, U.K.

^{4*}~~Joint first author~~ These authors contributed equally

⁵ Lead contact

^{**}Corresponding authors

Corresponding authors eEmail addresses: anna.york@yale.edu (Anna York), Adrian.Lloyd@warwick.ac.uk (Adrian. J. Lloyd), ad0364@coventry.ac.uk (Charo I. del Genio), jrws1m15@soton.ac.uk (Jonathan Shearer), k.hinxman@imperial.ac.uk (Karen. J. Hinxman), k.fritz@warwick.ac.uk (Konstantin Fritz), Vilmos.fulop@warwick.ac.uk (Vilmos Fulop), S.Khalid@soton.ac.uk (Syma Khalid), c.g.dowson@warwick.ac.uk (Christopher. G. Dowson), David.roper@warwick.ac.uk (David. I. Roper-) and S.Khalid@soton.ac.uk (Syma Khalid)

Summary

MurM, an aminoacyl-tRNA dependent ligase, generates branched Lipid II required for indirectly cross-linked peptidoglycan, and is essential for high-level penicillin resistance in the human pathogen *Streptococcus pneumoniae*. We have solved the X-ray crystal structure of *Staphylococcus aureus* FemX, an isofunctional homologue of MurM, and used this as a template to generate a MurM homology model. Using this model, we perform molecular docking and molecular dynamics to examine the interaction of MurM with the phospholipid bilayer and the membrane embedded Lipid II substrate. Our model suggests that MurM is associated with the major membrane phospholipid cardiolipin, and experimental evidence confirms that the activity of MurM is enhanced by this phospholipid and inhibited by its direct precursor phosphatidylglycerol. The spatial association of pneumococcal membrane phospholipids and their impact on MurM activity may therefore be critical to the final architecture of peptidoglycan and the expression of clinically relevant penicillin resistance in this pathogen.

Key Words

Streptococcus pneumoniae, MurM, penicillin resistance, peptidoglycan, indirect cross-links, lipid bilayer, homology modelling, molecular dynamics, molecular docking

Introduction

The peptidoglycan (PG) of the bacterial cell wall is a polymer consisting of alternating β -1,4 linked N-acetyl glucosamine (GlcNAc) and N-acetyl muramic acid (MurNAc) residues. Appended to the MurNAc sugar is a pentapeptide stem that can be cross-linked directly or indirectly to form a rigid mesh-like structure (Bugg et al., 2011). PG biosynthesis begins with the cytoplasmic formation of a Peptidoglycan nucleotide, which is subsequently converted into a lipid-linked PG precursor known as Lipid II. Lipid II is then transported across the membrane, where it is polymerized and cross-linked by the penicillin-binding proteins (PBPs) (Figure 1). PG is an essential component of the cell wall, involved in cell growth and division, maintaining structural integrity, and resisting high osmotic pressures. Inhibition of cell wall biosynthesis is a key mechanism for many antibiotics, including β -lactams, glycopeptides and amino acid analogues (Schneider and Sahl, 2010).

In *S. pneumoniae* and other Gram-positive bacteria, the glutamate at the second position of the Lipid II pentapeptide is α -amidated to form *iso*-glutamine by the essential GatT/MurD complex (Figueiredo et al., 2012, Münch et al., 2012, Zapun et al., 2013, Morlot et al., 2018). In addition, branched Lipid II, capable of generating indirect cross-links, can be formed by the non-essential MurM and MurN proteins. MurM and MurN are responsible for the sequential addition of amino acids to the third-position lysine of the pentapeptide stem of Lipid II (Filipe et al., 2000). MurM can append either L-serine or L-alanine at the first position of the dipeptide bridge, whilst MurN extends this modification by addition of an invariable L-alanyl moiety. Branched PG precursors are also found in several other Gram-positive bacterial pathogens, for example the glycyl-tRNA^{Gly} dependent enzymes FemX, A and B are responsible for the addition of a pentaglycyl bridge in *S. aureus* (Schneider et al., 2004). In comparison with other Gram positive organisms, the PG of *S. pneumoniae* is highly heterogeneous: the predominant C-terminal amino acid at position 1 of the dipeptide, and the proportion of indirect cross-links throughout the PG, vary significantly between different strains (Severin and Tomasz, 1996, Garcia-Bustos et al., 1987, Garcia-Bustos and Tomasz, 1990). *In vitro* and *in vivo* studies indicate that MurM from the penicillin-resistant strain *S. pneumoniae*(159) preferentially incorporates L-alanine, whilst MurM from a penicillin-sensitive strain *S. pneumoniae*(Pn16) preferentially incorporates L-serine (Lloyd et al., 2008). In addition, penicillin resistant strains demonstrated higher levels of indirect cross-linking in the PG compared to penicillin susceptible isolates, however the overall degree of cross-linking remained constant (Garcia-Bustos and Tomasz, 1990).

Resistance to β -lactam antibiotics in *S. pneumoniae* is characterised by extensive interspecies recombination of PBP transpeptidase domains, which results in sequence heterogeneity within and around the mosaic PBP active site with a consequential lowering of β -lactam binding affinity (Smith et al., 1991). This mechanism of resistance contrasts with that of many other bacteria that have acquired genes for β -lactamase enzymes which inactivate the antibiotic before it binds to and inhibits the PBPs.

1
2
3
4
5
6
7
8 Interestingly, deletion of the *murM* gene in *S. pneumoniae* eliminates indirect cross-links
9 from the PG and results in a complete loss of penicillin resistance (Filipe et al., 2001). It
10 has been proposed that the changes to the PBP active site which prevent β -lactam
11 binding, may also alter the Lipid II substrate specificity such that the PBPs bind branched
12 Lipid II more tightly than unbranched Lipid II. MurM is therefore necessary, but not
13 sufficient for resistance in clinical strains of *S. pneumoniae*, making it an interesting target
14 for the development of new inhibitors of antimicrobial resistance (Filipe and Tomasz,
15 2000).

16
17 The cytoplasmic membrane of *S. pneumoniae* contains two phospholipids,
18 phosphatidylglycerol (PhG) and cardiolipin (CL) (Trombe et al., 1979, Pesakhov et al.,
19 2007), where cardiolipin synthase is responsible for generating cardiolipin from two
20 molecules of phosphatidylglycerol (Schlame, 2008). The proportion of cardiolipin and
21 phosphatidylglycerol, as a percentage of the overall membrane lipids, varies in *S.*
22 *pneumoniae* between anaerobic and aerobic growth conditions. Cardiolipin was found to
23 decrease from 15.3 % to 8.3 %, whilst phosphatidylglycerol increased from 12.7 % to
24 16.3 % in anaerobic conditions compared to aerobic conditions (Pesakhov et al., 2007).
25 The peptidoglycan precursor, Lipid II is tethered to the cell membrane by virtue of its C55
26 Lipid II tail. Therefore, MurM acts on its lipid substrate in close proximity to the
27 cytoplasmic leaflet of the cell membrane and is potentially influenced by membrane
28 phospholipid composition.

29
30 Previously, MurM inhibitors have been identified; however, none have shown growth
31 inhibition or any effect on penicillin MIC, indicating that these compounds cannot
32 effectively cross the cytoplasmic membrane of *S. pneumoniae* (Cressina et al., 2007,
33 2009). MurM has thus far resisted extensive crystallization in our laboratory, and
34 consequently, its X-ray-solved structure is not available. However, in a related study we
35 were able to solve the X-ray structure of the isofunctional homologue of MurM from *S.*
36 *aureus* (FemX), which we have used here as a template for homology modelling of MurM.
37 Using this MurM homology model we have successfully identified the Lipid II binding site,
38 and used molecular dynamics (MD) simulations to investigate interactions between MurM
39 and both membrane phospholipids and its Lipid II substrate (Witzke et al., 2016). We
40 subsequently, studied the effects of these membrane embedded phospholipids, on the
41 enzymatic activity of MurM *in vitro*, corroborating our *in silico* analysis. These studies
42 provide new insights into the structure and activity of MurM, providing a link between
43 phospholipid membrane composition and peptidoglycan architecture. This may be useful
44 for the development of ~~novel~~ chemical probes for these ~~proteins, and~~ [proteins and](#) have
45 important implications for future studies on penicillin resistance mechanisms in *S.*
46 *pneumoniae*.

47 48 49 50 51 52 53 54 55 56 57 58 59 60 61 62 63 64 65 **Results**

X-ray crystallography and structure determination of *S. aureus* FemX

The crystal structure of *S. aureus* FemX was solved to a resolution of 1.62 Å and the structure was deposited in the PDB with accession number: 6SNR. A summary of the data collection and refinement statistics is given in Table 1.

The final solved structure of *S. aureus* FemX, contains a globular domain and a coiled-coil domain. Similar to FemA (Benson et al., 2002), the globular domain can be divided into two subdomains. Each subdomain contains a central five-stranded mixed polarity β -sheet surrounded by four α -helices. Subdomain 1A comprises residues 1-145 and 384-421 whilst subdomain 1B comprises residues 146-234 and 298-383. Unfortunately, residues 403-421 were not present in the density. The coiled-coil domain consists of two antiparallel α -helices, comprising residues 235-297. FemX and FemA can be superimposed onto each other with a root-mean-square deviation (RMSD) of ~2.7 Å over 384 residues. Similarly to FemA, FemX has a deep L-shaped channel of about 20 x 40 Å located alongside the globular domain and mainly in subdomain 1B. This channel comprises a peptidoglycan precursor binding site which was previously identified in *S. aureus* FemA (Benson et al., 2002). The identity of this peptidoglycan precursor binding site has been further confirmed by crystallograph analysis of *Weissella viridescens* FemX complexed with substrates (Biarrotte-Sorin et al., 2004).

Homology modelling of *S. pneumoniae* MurM

The structures of two MurM homologues, *S. aureus* FemA and *W. viridescens* FemX were solved previously by X-ray crystallography (Benson et al., 2002, Fonvielle et al., 2013, Biarrotte-Sorin et al., 2004). The *S. aureus* FemA structure was subsequently used as a template for homology modelling of MurM by Fiser et al. (2003). However, alignment of *S. aureus* FemA, *S. aureus* FemX, *S. pneumoniae* MurM and *W. viridescens* FemX (Supplemental Information: Figure S1) showed that *S. aureus* FemX possesses the highest sequence identity to MurM and is also more functionally homologous to *S. pneumoniae* MurM, as it appends the first amino acid of the cross-bridge to the Lipid II precursor (Matsuhashi et al., 1967, Schneider et al., 2004). In contrast *S. aureus* FemA appends the second and third amino acid residues of the cross-bridge to the α -amino group of a glycyl residue appended to the ϵ -amino group of the stem peptide L-lysyl residue of the Lipid II precursor. Therefore, given the difficulties in obtaining MurM crystals, we were motivated to solve the structure of its functional homologue (*S. aureus* FemX) by X-ray crystallography, to access the structure of MurM *in silico*.

Using the newly solved structure of *S. aureus* FemX, we generated a new homology model for MurM which consists of a globular domain comprising two subdomains and a coiled-coil helical arm (Figure 2). Each subdomain comprises two twisted β -sheet cores surrounded by α -helices; subdomain 1A is formed of residues 1-153 and 382-401, whilst subdomain 1B is made up of residues 154-241 and 294-381. The coiled-coil domain comprises residues 242-293. Whilst the new MurM homology model presented here is similar to the previous model (Fiser et al., 2003), the RMSD of the two models is 3.8 Å over 368 residues, indicating that there are some key structural differences, namely; loss of N-terminal β 1, and antiparallel β 6/ β 13 from the previous model; addition of α 5 and β 11/ β 12; and presence of α -helical secondary structure proximal to the C-terminal end of the new this MurM model.

Formatted: Not Highlight

Formatted: Not Highlight

Formatted: Not Highlight

Formatted: Not Highlight

Formatted: Not Highlight

Identification of a possible Lipid II binding site of MurM

The new MurM model revealed a binding pocket which was not present in the previous Fiser et al model of MurM. Structural comparison between *W. viridescens* FemX co-crystallised with its UDP-MurNAc-pentapeptide substrate and this new MurM model, allowed identification of a Lipid II binding site that corresponds with the peptidoglycan precursor binding sites identified previously in *S. aureus* FemA and *W. viridescens* FemX (Benson et al. 2002; Biarrotte-Sorin et al., 2004) and in our structure of *S. aureus* FemX. When the new MurM model and the *W. viridescens* FemX were aligned and overlaid, the newly identified MurM binding site appeared to easily accommodate the soluble UDP-MurNAc-pentapeptide substrate well (Figure 3A). The following 8 residues; Tyr103, Lys36, Asn38, Trp39, Thr209, Arg211, Try215 and Tyr256, were independently proposed to be involved in substrate binding in the peptidoglycan precursor and tRNA liganded *W. viridescens* FemX structures (Biarrotte-Sorin et al., 2004, Fonvielle et al., 2013). The corresponding MurM residues, defined as having residues which have similar properties, and occupying a similar location and orientation in physical space, with side chains facing the binding pocket, were identified in the MurM structure as Phe103, Lys35, Trp38, Arg215 and Tyr219, therefore these residues may also be important for substrate binding in MurM.

Next molecular docking using AutoDock Vina (Trott and Olson, 2010) was conducted to independently investigate docking of the Lipid II substrate to the new MurM model we generated. Lipid II is a large molecule that is, in general, unsuitable for molecular docking studies. In addition, the lipid tail is embedded in the membrane, and so is not itself available for binding to MurM. Therefore, a truncated Lipid II molecule, comprised of a methyl capped diphospho GlcNAc-MurNAc-pentapeptide, was used for these docking experiments (Supplemental Information: Figure S2).

When AutoDock Vina was allowed to search the entire protein surface of MurM, all docking results returned were within the identified binding site, indicating that there are no other suitable binding sites on the protein. The search was then restricted to the binding site and the top ten results were obtained. The top five results obtained all had identical binding affinities of $-7.3 \text{ kcal.mol}^{-1}$; however, two of these docking orientations, where the phosphates are located deep within the binding pocket, would be physically impossible for the natural substrate (Lipid II) *in vivo*, since the membrane-embedded prenyl lipid tail is appended via the phosphate. The remaining 3 docking orientations, all orient the phosphates close to the opening of the binding site with the pentapeptide chain disappearing deep into the binding pocket. The exact orientation of the pentapeptide chain is variable, indicating that the binding site is spacious and that Lipid II may be accommodated in a number of different possible orientations. Figure 3B shows one conformation in which the docking of truncated Lipid II is similar to the orientation of the soluble UDP-MurNAc-pentapeptide from *W. viridescens* FemX overlaid with MurM (Figure 3A), the remaining four substrate orientations with binding affinities of $-7.3 \text{ kcal.mol}^{-1}$ are shown in the Supplementary Information (Supplemental Information: Figure S3). A key limitation of docking is that it considers the protein as rigid; therefore, multiple substrate orientations may indicate that conformational changes within the binding site may occur upon substrate binding or during catalysis.

1
2
3
4
5
6
7
8
9
10
11
12
13
14
15
16
17
18
19
20
21
22
23
24
25
26
27
28
29
30
31
32
33
34
35
36
37
38
39
40
41
42
43
44
45
46
47
48
49
50
51
52
53
54
55
56
57
58
59
60
61
62
63
64
65

Additional docking studies were performed to further explore the lipid II binding pose in the putative MurM binding site and establish whether this binding site shows specific affinity for lipid II or is indiscriminate between different lipid species. Therefore, Lipid II, cardiolipin, phosphatidylglycerol and phosphatidylethanolamine lipids (full molecules) were docked into the putative binding site, where the binding site is defined by the residues Lys35, Trp38, Phe103, Arg215 and Tyr219. We found Lipid II bound into this site with atoms of the headgroup within 3 Å of the residues Lys35, Trp38, Phe215 and Arg219, and with the Lipid II tail outside of this site. In stark contrast the cardiolipin and phosphatidylethanolamine headgroups did not show any preference for this site, instead the binding poses showed their tails inserted into the cavity. There was one binding pose for phosphatidylglycerol in which the phospholipid headgroup was in the putative binding site, however a portion of the tail was also inside it; the remaining two phosphatidylglycerol poses had the tails inserted into this cavity. For each lipid type the top cluster of binding poses produced by HADDOCK2.4 (Van Zundert et al., 2016) were analysed, and the top 3 binding poses for each lipid are shown in the Supplemental Information (Figure S4).

Interactions between MurM and the lipid bilayer

Given the docking studies are performed in the absence of the membrane environment, a set of coarse-grained MD simulations was next performed to establish the likelihood of MurM being orientated on the membrane such that the putative binding site is available to Lipid II. Molecular dynamics simulations were used to model the interactions of MurM with the lipid bilayer. Six independent coarse-grained simulations were conducted for each of three membrane systems described in the Supplemental Information (Table S1). In 16 of these simulation runs MurM readily associated with the membrane in <3 µs and its orientation with respect to the membrane remained unchanged for the remaining 2 µs (Supplemental Information: Figure S5). In addition, in the same membrane leaflet as the peripheral MurM, more than 50 % of Lipid II molecules were located within 2 nm of the protein. MurM associated with the membrane in a number of different orientations which can be classified into two groups, those in which the binding site predicted from docking studies is available for lipid binding and those in which it is not. Table 2 shows that in 18 unbiased simulations; MurM adhered to the membrane in 16 of the simulations and of these, the binding site was available for Lipid II binding in 11 and unavailable in only 5. In 3 of these 18 unbiased simulations, MurM was oriented such that the Lipid II molecule was located in the putative binding site, which demonstrates that the Lipid II is able to successfully enter this binding site even on the short timescale of a MD simulation (Figure 4). Back mapping of one of these systems to all-atom resolution allowed the binding site to be explored in more detail. Three independent atomistic simulations each of 250 ns duration found Lipid II located in the same binding site of MurM that was identified during molecular docking of the truncated Lipid II substrate, and in the co-crystal structure of UDP-MurNAc-pentapeptide with *W. viridescens* FemX (Figure 3A). In both the molecular docking and atomistic simulations, the Lipid II headgroup forms stable interactions with Lys35, Trp38, Arg215 and Tyr219.

Similarly to the molecular docking findings, this MD simulation shows that the MurM binding site is flexible and allows the Lipid II molecule to adopt a wide variety of conformations (Figure 5). This may suggest that binding of a second substrate or a large conformational change may be required for catalysis.

Interactions between MurM and membrane phospholipids

Formatted: Not Highlight

Formatted: Not Highlight

Formatted: Not Highlight

Formatted: Not Highlight

Formatted: Not Highlight

Formatted: Not Highlight

Molecular dynamics simulations were used to investigate the effects of membrane phospholipids (cardiolipin and phosphatidylglycerol) on MurM at the cytoplasmic membrane interface. To investigate local lipid enrichment/depletion, we calculated 2D enrichment maps across the entire membrane and D-E indices within a 1.1 nm of MurM, as described by Corradi et al. (2018) (See STAR Methods). A D-E Index < 0 , or an enrichment percentage $< 0\%$, indicated that the specified lipid was depleted with respect to the bulk membrane composition. Figure 6 shows that upon association of MurM with the cytoplasmic membrane, there was no effect on the distribution of phosphatidylglycerol or phosphatidylethanolamine. However, in membranes containing 8 % or 16 % cardiolipin, cardiolipin was enriched at the MurM:membrane interface.

The importance of these observations were considered *in vitro* by measuring the enzymatic activity of MurM in the presence of varying concentrations of cardiolipin or phosphatidylglycerol. These enzymatic studies show that cardiolipin activates MurM, whilst phosphatidylglycerol inhibits MurM in a concentration dependent manner. Figure 6E shows the enzymatic activation of MurM with respect to cardiolipin concentration, a 9.1-fold activation of MurM was achieved, with 50 % activation occurring at 0.4 mM cardiolipin. Figure 6F shows that the activity of MurM could be completely inhibited by phosphatidylglycerol, with an IC_{50} of 0.2 mM. Furthermore, Hill coefficients of 2.7 ± 0.3 and 2.8 ± 0.2 for cardiolipin and phosphatidylglycerol respectively, indicate that both these phospholipids exhibit their effects on MurM in a cooperative manner. Phosphatidylethanolamine, used in the construction of the model pneumococcal membrane to which MurM bound, when tested at a concentration of 0.72 mM, only slightly activated MurM activity by 0.32-fold (duplicate determination with a difference of $< 10\%$). In comparison, 0.72 mM cardiolipin activated MurM by 8-fold (Figure 6E). Therefore, the impact of phosphatidylethanolamine on the disposition of MurM relative to its interaction with Lipid II and the phospholipid bilayer could be neglected.

Discussion

The crystal structure of *S. aureus* FemX has allowed the us to generate an improved homology model of MurM leading to the identification of a putative Lipid II binding site. Fiser et al. (2003) proposed a different MurM model and speculated about an alternative binding site based upon structural and functional analogy between MurM and N-myristoyltransferase (NMT) proteins. However, whilst the substrates of both NMT proteins and MurM are lipids, they are contextually very different. The NMT proteins are cytoplasmic proteins that contain a deep, narrow pocket which is highly specific for the myristoyl fatty acyl chain (Wright et al., 2010, Heuckeroth et al., 1988). In contrast, MurM binds the disaccharide head group and pentapeptide side chain of Lipid II, and the undecaprenyl C55 lipid tail is embedded in the membrane. Despite similarities with NMT proteins, our newly identified substrate binding site more closely resembles those of *W. viridescens* FemX, *S. aureus* FemX and FemA.

1
2
3
4
5
6
7
8
9
10
11
12
13
14
15
16
17
18
19
20
21
22
23
24
25
26
27
28
29
30
31
32
33
34
35
36
37
38
39
40
41
42
43
44
45
46
47
48
49
50
51
52
53
54
55
56
57
58
59
60
61
62
63
64
65

The orientations of truncated Lipid II in docking studies and Lipid II in molecular dynamics simulations are strikingly similar to each other and also the orientation of UDP-MurNAc-pentapeptide substrate co-crystallised in *W. viridescens* FemX. This is consistent with the observation that, although inefficient compared to Lipid II, UDP-MurNAc pentapeptide is a MurM substrate (Lloyd et al., 2008). In all cases, the diphosphates are near the surface of the protein, and the protruding pentapeptide reaches into the binding pocket with the third-position lysine on the left-hand side of the binding pocket. In addition, previous studies suggest that the height of the Lipid II head group is 19 Å (Ganchev et al., 2006), and the binding pocket of this model was measured to be 15 Å. Since the Lipid II head group is flexible, and the binding site provides enough room for the substrate to bend, these measurements are consistent. Together with our findings, this strongly supports the identification of this newly identified cavity as the Lipid II binding site and suggests that the Lipid II binds to MurM in an orientation similar to that of *W. viridescens* FemX binding to its substrate.

Alanyl-phosphatidylglycerol synthase (PDB ID 4v34) similarly to MurM, also utilizes both lipid and alanyl-tRNA^{Ala} substrates (Hebecker et al., 2015), in order to successfully bring these two substrates together for catalysis, it possesses two binding sites, located on opposite sides of the protein which are connected by a channel. The protein itself provides a barrier between the hydrophobic lipid and the hydrophilic tRNA, such that they do not come into close proximity with each other. The negatively charged surface patch identified previously (Fiser et al., 2003) remains present on this [new](#) homology model of MurM, and is located on the opposite side of the protein with respect to the Lipid II binding site, which is located within a positively charged surface patch (Supplemental Information: Figure S6). This negative patch is unsuitable for the binding of negatively charged tRNA and so it is unlikely that MurM shares the same mechanism of action as alanyl-phosphatidylglycerol synthase. The negatively charged surface patch may however be important for protein:protein interactions occurring either at the cell surface or in the cytoplasm.

These modelling studies reveal that the stem peptide protrudes perpendicular to the surface of the membrane into the active site of MurM. Therefore, in order for alanyl-tRNA^{Ala} to simultaneously interact with MurM, whilst it is located over its lipid substrate, the highly negatively charged hydrophilic tRNA would have to be brought into close proximity with the negatively charged phospholipid head groups and/or the hydrophobic phospholipid tails below them. Given that this would be a highly unfavourable interaction, we propose an alternative 'ping-pong' mechanism of action for MurM whereby MurM is initially aminoacylated by alanyl- or seryl-tRNA in the cytoplasm before translocation to the cell membrane for aminoacyl transfer to Lipid II. Whilst the MurM is in the cytoplasm and not interacting with the membrane, the positively charged patch, located at the newly proposed Lipid II binding site, may facilitate interaction with a polyanionic substrate such as tRNA. Once this has occurred, subsequent interaction of the aminoacyl-MurM with the surface of the membrane could accommodate the correct and catalytically productive interaction of aminoacylated-MurM with Lipid II. Although this proposed mechanism is at variance with the sequential mechanism of catalysis proposed for *W. viridescens* FemX (Hegde and Blanchard, 2003), here, both substrates are highly hydrophilic nucleotide or

1
2
3
4
5
6
7
8
9
10
11
12
13
14
15
16
17
18
19
20
21
22
23
24
25
26
27
28
29
30
31
32
33
34
35
36
37
38
39
40
41
42
43
44
45
46
47
48
49
50
51
52
53
54
55
56
57
58
59
60
61
62
63
64
65

polynucleotide derivatives in the same cellular sub-compartment and are therefore without biophysical impediment with regard to their proximity during catalysis. Here, with regard to MurM, the chemical properties and location of both substrates indicate an advantage to a mechanism which avoids their simultaneous binding.

The pneumococcal peptidoglycan is heterogeneous with respect to its composition of directly and indirectly cross-linked stem peptides. It remains unclear as to whether the activity of MurM, and therefore the generation of indirect cross-links is distributed equally around the entire cell surface, or whether it is localised to specific sites. Phospholipids are known to be involved in the spatial and temporal biochemistry of cells (Lin et al., 2019), and cardiolipin was shown to be enriched at the poles and septa of *Escherichia coli* and *Bacillus subtilis*, localising specific membrane-associated proteins to these regions (Bramkamp and Lopez, 2015). Our simulations indicate that, whilst cardiolipin enrichment occurs within the membrane in the presence of MurM, this phospholipid is not essential for membrane association of MurM to occur. Therefore, it remains uncertain as to whether *in vivo* cardiolipin is highly concentrated in patches in the membrane and is used to recruit MurM to that location, or whether association of MurM with the membrane drives the enrichment of cardiolipin in the membrane.

Despite this uncertainty, we show that cardiolipin stimulates the enzymatic activity of MurM, and whilst it is not clear if this increased activity is as a result of a direct effect on the protein or the Lipid II substrate, or both, the spatial association of cardiolipin to the MurM protein suggests that at least some of this effect may be due to direct interactions with the MurM protein.

Cardiolipin has previously been found to bind to and activate a wide range of proteins including MurG (van den Brink-van der Laan et al., 2003), rat liver protein kinase N (Morris et al., 1994, Peng et al., 1996), porcine heart AMP deaminase (Purzycka-Preis and Zydowo, 1987), rat liver multi-catalytic proteinase (Ruiz de Mena et al., 1993), *E. coli* glycerol-3-phosphate acyltransferase (Scheideler and Bell, 1989), *E. coli* dnaA (Sekimizu and Kornberg, 1988) and streptococcal hyaluronan synthases (Tlapak-Simmons et al., 1999a,b, 2004, Weigel et al., 2006, Tlapak-Simmons et al., 1998). This further supports the contention that cardiolipin affects MurM activity by directly interacting with MurM. Similar cardiolipin-mediated sigmoidal stimulatory effects have been seen with other streptococcal membrane proteins such as the hyaluronan synthases from *Streptococcus pyogenes* and *Streptococcus equismilis* (Tlapak-Simmons et al., 1999a,b, 2004, Weigel et al., 2006). In these examples, up to sixteen cardiolipin molecules are believed to associate with single hyaluronan synthase molecule (Tlapak-Simmons et al., 1998).

We also show that phosphatidylglycerol inhibits the catalytic activity of MurM, and that the concentration of this lipid in the membrane environment surrounding the MurM changes very little. Therefore, the inhibitory effect of phosphatidylglycerol may be exerted by altering the presentation of the Lipid II substrate to MurM, rather than by having a direct effect on the protein itself. It is possible that in *S. pneumoniae*, as in *E. coli* and *B. subtilis*, cardiolipin gathers in specific regions of the membrane, where in the

pneumococcus it localises and up-regulates the activity of MurM, resulting in higher levels of indirect cross-linking in these regions.

Whilst MurM alone is not sufficient for penicillin resistance, the enzyme is crucial together with mosaic *S. pneumoniae* PBPs for the generation of a highly resistant phenotype. Deletion of *murM* from resistant strains resulted in a virtual abolition of penicillin resistance that could not be restored by PBP DNA. Indeed, additional *murM* DNA from a resistant strain was required for full expression of donor level penicillin resistance (Filipe and Tomasz, 2000, Smith and Klugman, 2001). Given the importance of MurM for penicillin resistance, the enrichment of cardiolipin at the MurM:membrane interface which activates MurM, and the inhibition of MurM activity by phosphatidylglycerol, may regulate the penicillin resistance phenotype imparted by MurM activity which may therefore be regulated by cardiolipin synthase activity. These findings have therefore revealed a crucial and hitherto unexplored facet of penicillin resistance suggesting the involvement of other areas of pneumococcal metabolism in the expression of clinical antibiotic resistance.

Conclusions

This new MurM structural model presented in this work, allowed identification of the Lipid II binding site and the contextual presentation of this substrate to MurM, furthermore this work characterised the impact of membrane phospholipids on MurM at the MurM:membrane interface, and interface and may have spatial mechanistic implications for the catalytic activity of this protein. Molecular dynamics enabled the *in silico* investigation into MurM:membrane interactions, which are often overlooked when studying enzymes which act at the cytoplasmic membrane interface. The subsequent *in vitro* experiments on the importance of phospholipids for MurM activity, corroborate the *in silico* findings, supporting the role of phospholipids as an important contributor to the regulation of MurM at the membrane. These studies provide new insights into the structure of MurM which may guide future mutational studies, and studies and allow a more detailed analysis of the structure-function relationship of this protein. This research contributes important findings towards achieving a more complete understanding of its role in pneumococcal penicillin resistance mechanisms.

Acknowledgements

This research was supported in part by the Midlands Integrative Biosciences Training Partnership (MIBTP) BBSRC grant BB/J014532/1, and the Centre for Doctoral Training in Theory and Modelling in Chemical Sciences (TMCS DTC) EPSRC grant EP/L015722/1, as well as MRC grants G1100127, G0400848, MR/N002679/1 and BBSRC grant BB/N003241/1. The authors would like to acknowledge the help of the Media Preparation Facility in the School of Life Sciences at the University of Warwick. We would also like to thank Dr Allister Crow for his help and support with using PyMOL.

1
2
3
4
5
6
7
8
9
10
11
12
13
14
15
16
17
18
19
20
21
22
23
24
25
26
27
28
29
30
31
32
33
34
35
36
37
38
39
40
41
42
43
44
45
46
47
48
49
50
51
52
53
54
55
56
57
58
59
60
61
62
63
64
65

Author Contributions

Conceptualization, A.Y., A.J.L., D.I.R., and S.K.; Investigation, K.F., K.J.H., V.F., A.J.L., A.Y., J.S., C.I.G.; Methodology/Software/Formal Analysis, C.I.G., J.S., A.Y., and S.K.; Writing – Original Draft, A.Y., J.S., and C.I.G.; Writing – Review & Editing, A.Y., A.J.L., S.K., D.I.R.; and C.G.D.; Funding Acquisition, A.Y., J.S., and C.G.D.; Supervision, A.J.L., D.I.R., S.K., and C.G.D.; Project Administration, A.Y.; Visualization, A.Y., A.J.L., J.S., and S.K.

Declaration of Interests

The authors declare no competing interests.

Figure Titles and Legends

Figure 1. The PG biosynthesis pathway. 1) The cytoplasmic stage is characterised by the formation of UDP-MurNAc-pentapeptide (UDP-MurNAc-5P) by MurA-MurC. The pentapeptide stem peptide usually comprises L-Ala- γ -D-Glu-L-Lys-D-Ala-D-Ala in most Gram-positive organisms including the pneumococcus.. 2) At the internal face of the cytoplasmic membrane MraY catalyses the formation of Lipid I from UDP-MurNAc-5P to undecaprenyl-pyrophosphate, which is then converted to Lipid II by MurG. In *S. pneumoniae*, the second position D-glutamyl α -carboxyl is amidated to D-iso-glutamine (iGln) by the MurT/GatD complex, and in some cases a dipeptide branch of either L-Ser/L-Ala or L-Ala/L-Ala may be appended at the ϵ -amino group of the third position lysine by MurM and MurN, respectively. The exact order of the cytoplasmic membrane steps remains uncertain, but here for clarity, they appear as a linear sequence, with conversion to Lipid II occurring before peptide stem modifications, and amidation occurring before branching. Lipid II is translocated across the membrane by MurJ. 3) At the external face of the cytoplasmic membrane, PBPs form glycan chains by transglycosylation (TG), with the concomitant release of undecaprenyl-pyrophosphate, and form either direct or indirect cross-links throughout the PG layer via transpeptidation (TP). Nucleotide sugars UDP-GlcNAc and UDP-MurNAc and the sugars GlcNAc and MurNAc are signified by blue, violet, dark blue and purple elongated hexagons respectively. Figure created using BioRender.com.

Figure 2. Cartoon representation of MurM predicted structure. 14 α -helices (red), 12 β -sheet (yellow) and unstructured regions (green). Best model obtained based on SOAP and DOPE scores following homology modelling using MODELLER with *S. aureus* FemX as a template. The structure was rendered in PyMOL (Version 2.2.0).

Figure 3. Surface representation of MurM binding site. A) MurM₁₅₉ model aligned and overlaid with the UDP-MurNAc-pentapeptide substrate which was co-crystallised with *W. viridescens* FemX B) MurM₁₅₉ model with truncated Lipid II docked in the binding site, using AutoDock Vina C) MurM₁₅₉ model with Lipid II in the binding site, from membrane simulations. Figures were created with PyMOL (Version 2.2.0) and Chimera (Version 1.13.1).

Figure 4. Lipid II binding to the putative MurM binding site. Panels A, B and C show the three simulations where Lipid II was found to bind in the putative MurM binding site. Each panel shows the MurM binding to Lipid II with respect to the membrane (top), and an enlarged image of the MurM binding to Lipid II, with the membrane removed (bottom). MurM binding site residues F103, K35, W38, R215 and Y219 are depicted in yellow, where the Lipid II head group and prenyl chain are rendered in red and blue respectively.

Figure 5. Different conformations of Lipid II inside MurM binding site. MurM (grey) with Lipid II binding, coloured on a Blue to white to red scale with respect to simulation time, in system 5 (Table S2).

Figure 6. Interactions between MurM and membrane phospholipids. Depletion-enrichment (D-E) indices for phosphatidylethanolamine (PE), phosphatidylglycerol (PhG)

and cardiolipin (CL) occurring within a 1.1 nm perimeter of the MurM protein for A) Systems 4 and 5 (molar ratio of 75 % phosphatidylethanolamine and 25 % phosphatidylglycerol), B) System 6 and 7 (molar ratio of 76 % phosphatidylethanolamine, 16% phosphatidylglycerol and 8 % cardiolipin) and C) System 8 and 9 (molar ratio of 72 % phosphatidylethanolamine, 12 % phosphatidylglycerol and 16 % cardiolipin). The D-E index was determined from 150-250 ns in 50 ns blocks for all repeats for a total of 8 values per plot. D) Example of a depletion-enrichment map with MurM at the membrane. White dots represent the center of geometry of each protein amino acid residue, and the percentage enrichment of phospholipid is indicated by the colour. E) Activation of MurM was calculated as the product of subtraction of MurM velocity in the absence of cardiolipin ($v_{0(-C)}$) from MurM velocity in the presence of cardiolipin ($v_{0(+C)}$) divided by $v_{0(-C)}$ and was plotted versus cardiolipin concentration. F) Inhibition of MurM was calculated as $((v_{0(-PhG)} - (v_{0(+PhG)}))/v_{0(-PhG)}) \times 100$ (where PhG denotes phosphatidylglycerol) and was plotted versus phosphatidylglycerol concentration. Data were fitted as described in the text. GraphPad Prism (Version 8.4.1) and Matplotlib (Version 3.0.3) were used for data analysis and figure preparation.

Tables with Titles and Legends

Data collection	FemX
Synchrotron radiation, detector and wavelength (Å)	Pilatus 6M-F, 0.920
Unit cell (a, b, c (Å), α , β , γ (°))	45.01, 83.62, 133.93, 90.0
Space group	P2 ₁ 2 ₁ 2 ₁
Resolution (Å)	52.27-1.62 [1.66-1.62]
Observations	422,822 [29,596]
Unique reflections	65,058 [4,782]
$I/\sigma(I)$	15.7 [2.6]
R_{sym}^a	0.065 [0.567]
R_{meas}	0.078 [0.690]
R_{pim}	0.031 [0.273]
Completeness (%)	99.7 [99.8]
Refinement	
Non-hydrogen atoms	3,397 (including 177 waters)
R_{cryst}^b	0.221 [0.262]
Reflections used	61,691 [4,531]
R_{free}^c	0.262 [0.296]
Reflections used	3,294 [244]
R_{cryst} (all data) ^b	0.222
Average temperature factor (Å ²)	26
Rmsds from ideal values	
Bonds (Å)	0.013
Angles (°)	1.5
DPI coordinate error (Å) ^d	0.098
Ramachandran Plot ^e	
Favoured (%)	98.0
Outliers (%)	0.0

Table 1. Summary of crystallographic data collection and refinement statistics from the *S. aureus* FemX structure. The highest resolution bin of data is indicated by square parentheses. Numbers in square parentheses refer to values in the highest resolution shell. ^a $R_{sym} = \sum_j S_j S_h |I_{h,j} - \langle I_h \rangle| / \sum_j S_j S_h \langle I_h \rangle$ where $I_{h,j}$ is the j th observation of reflection h , and $\langle I_h \rangle$ is the mean intensity of that reflection. ^b $R_{cryst} = \sum |F_{obs}| - |F_{calc}| / \sum |F_{obs}|$ where F_{obs} and F_{calc} are the observed and calculated structure factor amplitudes, respectively. ^c R_{free} is equivalent to R_{cryst} for a 4% subset of reflections not used in the refinement (Brünger, 1992). ^dDPI refers to the diffraction component precision index (Cruickshank, 1999). ^eAs calculated by Molprobit (Williams et al., 2018).

Membrane	Available	Unavailable	Non-adherence	Lipid II in binding site
1 (0 % CL)	4	1	1	1
2 (12 % CL)	4	1	1	2
3 (16 % CL)	3	3	0	0

Table 2. Summary of MurM adherence to and orientation on the three different membrane systems. Orientation of MurM was categorized such that the putative binding site was either available for Lipid binding (facing/close to the membrane) or unavailable for Lipid II binding (facing away from the membrane).

STAR Methods

RESOURCE AVAILABILITY

Lead Contact

Further information and requests for resources and reagents should be directed to and will be fulfilled by the Lead Contact, David Roper (David.Roper@warwick.ac.uk).

Materials Availability

This study did not generate any new unique reagents. Plasmids will be available by Materials Transfer Agreement (MTA) request in line with University of Warwick IP requirements.

Data and Code Availability

No novel code was generated during this work. Modelling scripts and raw data are available from the authors upon request.

METHOD DETAILS

Cloning, overexpression and purification of *S. aureus* FemX

The *S. aureus* Mu50 FemX gene was amplified from chromosomal DNA using Oligonucleotides FemX forward: TTTGCGGGTGGTCTCCCATGGAAAAGATGCATATC ACTAATCAGG and FemX Reverse: TTTGCGCTCGAGGCCCTGAAAATACAGGTTTC TTTTCGTTTTAATTTACGAGATATTTAATTTAGC. The resulting PCR fragment was cleaved with *BsaI* and *XhoI* and cloned into pET28 between the *NcoI* and *XhoI* restriction sites to create pET28::FemX, containing a Tobacco Etch Virus (TEV) protease cleavable C-terminal hexa-histidine tag. *E. coli* B834 (DE3) harbouring plasmid pRARE2 (which supplies seven rare tRNAs to support expression of genes in *E. coli*) were transformed with pET28::FemX. Transformed *E. coli* B834 (DE3) pRARE2 were used to inoculate M9 media supplemented with all 19 L-amino acids and 40 mM L-selenomethionine in place

in L-methionine (Doubl  , 1997). Transformants were cultured at 37  C at 180 rpm until an optical density at 600 nm (OD₆₀₀) of 0.4-0.6 was reached. Protein expression was induced by 1 mM isopropyl-D-1-thiogalactopyranoside at 25  C for 4 hours. Cells were harvested by centrifugation at 6,000 *xg* for 15 minutes and cell pellets containing 4-6 g of cells were resuspended in 20 mL of 50 mM sodium phosphate pH 7.0, 1M NaCl and 2.5 mg.mL⁻¹ lysozyme to which one tablet of Pierce EDTA free Protease Inhibitor was added. The cell suspension was incubated with slow rotation for 30 minutes at 4  C before disruption using a Bandelin Sonopuls sonicator with 3 x 30 second bursts at 70 % power. The lysate was clarified by centrifugation at 50,000 *xg* at 4  C for 30 minutes. FemX was then purified by immobilised metal affinity chromatography (IMAC) using a 5 mL gravity fed column of cobalt Talon resin equilibrated with 50 mL of 50 mM sodium phosphate pH 7.0, 500 mM NaCl, 20 % (v/v) glycerol (equilibration buffer) supplemented with 10 mM imidazole. Once the 50,000 *xg* supernatant was loaded onto the column, it was eluted sequentially with 50 mL of equilibration buffer with 10 mM imidazole, 30 mL of equilibration buffer with 50 mM imidazole and 30 mL of equilibration buffer with 200 mM imidazole. 10 mL Fractions were analysed by SDS-PAGE and those containing FemX were pooled and concentrated, using a vivaspin 20 centrifugal concentrator (10,000 molecular weight cut off (MWCO), as required. Size exclusion chromatography in 50 mM sodium phosphate pH 7.0, 500 mM NaCl and 20 % (v/v) glycerol was used to further purify FemX on a Superdex 75 10/300 column. The histidine tag was then removed from the FemX protein by digestion with histidine-tagged TEV protease at a molar ratio of 100:1 FemX : TEV protease at 4  C overnight. Cleaved and uncleaved protein were separated by a reverse IMAC following the procedure described above.

FemX crystallisation and data collection

FemX was exchanged into 50 mM ethanolamine pH 10.0, 100 mM NaCl and 20 % (v/v) glycerol, concentrated to 15 mg.mL⁻¹ using a vivaspin 20 centrifugal concentrator column with a 10,000 MWCO and screened for suitable crystallisation conditions using a honeybee 963 crystallisation robot against JCSG plus, PACT primer and Morpheus crystallisation screens. Crystals obtained from the Morpheus screen were used directly for data collection experiments, although crystallization conditions were further refined to 0.12 M ethylene glycol, 0.1 M MES/imidazole pH 6.3 and 28 % (w/v) ethylene glycol-PEG 8000. Crystals were frozen directly for X-ray diffraction data experiments on the I04-1 beamline at the Diamond synchrotron (Didcot, UK) using a Pilatus 6M-F detector. Data were processed automatically using Xia2 (Winter, 2010) to 1.62  . Molecular replacement was not successful so selenomethionine containing FemX protein was produced and used to obtain FemX crystals (FemX-SeMet) in the same crystallisation conditions and the structure was solved by single anomalous diffraction (Leahy et al., 1992). X-ray data from the FemX-SeMet crystal were collected on the I02 beamline at the Diamond synchrotron (Didcot, UK) using a Pilatus 6M detector. All data were indexed, integrated and scaled using the XDS package (Kabsch, 2010). All 10 of expected selenium atoms in the asymmetric unit were located and refined by the SHELX suite

(Sheldrick, 2010). These sites were used to obtain preliminary phases. The starting model was built by ARP/wARP (Langer et al., 2008). This model was used to refine the higher resolution data. The structure was refined using iterative cycles of REFMAC (Vagin et al., 2004) and model building/solvent addition with COOT (Emsley et al., 2010).

Cloning, Overexpression and Purification of *S. pneumoniae*(159) MurM

As described in Lloyd et al. (2008), the MurM allele of *S. pneumoniae*(159) was cloned with a C-terminal histidine tag into pET21b and over-expressed in *E. coli* C41 (DE3)/pRIL. Cells were harvested by centrifugation and treated with 2.5 mg.mL⁻¹ hen egg white lysozyme prior sonication. MurM was solubilised with 1 M NaCl and fractionated between 25 % and 50 % of saturation ammonium sulfate followed by purification by size exclusion chromatography with Sephacryl S-200 and by immobilized metal affinity chromatography (IMAC) using cobalt Talon resin. The purity and identity of the final products of these purifications were assessed by SDS-PAGE.

Cloning, Overexpression and Purification of *S. pneumoniae*(Pn16) AlaRS

As described in Lloyd et al. (2008), the AlaRS allele of *S. pneumoniae*(Pn16) was cloned into pET26a and over-expressed in *E. coli* BL21(DE3) star/pRARE. The soluble protein was purified using nickel-chelated Chelating sepharose, desalted and further purified by anion exchange chromatography on a 0.98 ml MonoQTM column. The purity and identity of the final products of these purifications were assessed by SDS-PAGE.

Preparation of MurM substrates

The substrates used for assays of MurM were prepared as follows:

Lipid II(Lys): The peptidoglycan intermediate Lipid II(Lys) (undecaprenyl pyrophosphoryl N-N-acetyl muramyl (N-acetyl glucosaminy) L-alanyl- γ -D-glutamyl-L-lysyl-D-alanyl-D-alanine) was prepared by re-capitulation of the peptidoglycan synthesis pathway as described (Lloyd et al. 2008).

[³H]-Alanyl-tRNA^{Ala}: *Micrococcus flavus* tRNA was isolated from cell pellets of *M. flavus* cultures grown to late exponential phase by phenol extraction followed by isopropanol precipitation, anion exchange chromatography and ethanol precipitation as described by Zubay (1962) as adapted by Lloyd et al. (2008). tRNAs were renatured in 2 mM MgCl₂ at 60°C and aminoacylated with [2,3-³H]-L-alanine *S. pneumoniae* (Pn16) AlaRS as described by Lloyd et al. (2008) and quantitated by liquid scintillation counting.

***S. pneumoniae* MurM enzymology**

MurM was assayed as described by Lloyd et al. (2008) in duplicate in a final volume of 35 μ l of 50 mM 3-(N-morpholino)-propane sulphonic acid adjusted to pH 6.8, 30 mM KCl, 10 mM MgCl₂, 1.5 % (w/v) CHAPS (Assay Buffer), 1 mM DTT, 1 mM L-alanine, 10 μ M Lipid II-Lys and 24.3 nM MurM. Reactions were initiated by the addition of 0.45 M [³H]-alanyl-tRNA^{Ala} (1000 cpm.pmol⁻¹) and were incubated at 37 °C for two minutes, over which time frame, product accumulation was linear with respect to time. Where the impact of cardiolipin or phosphatidylglycerol on MurM activity was assessed, the required

amounts of 10 mg/mL stocks of each phospholipid in ethanol or chloroform/methanol (49:1) were dried down in the reaction vials the assays were to be performed in, and solubilised by addition of assay buffer. Reactions were terminated by the addition of 35 µl of ice-cold 6 M pyridinium acetate pH 4.5 and 70 µl ice-cold n-butanol. The incubations were rapidly mixed and centrifuged for 5 minutes at 1 °C at 13,000 xg, after which time the n-butanol phase was washed with 70 µl of water and then assayed for [³H]-Lipid II-L-Ala by liquid scintillation counting. Tritium counts accumulated in control reactions performed without Lipid II(Lys) were subtracted from corresponding data acquired in the presence of this substrate. MurM activities in the presence of phospholipid were related to the activity of the enzyme in the absence of phospholipid and plotted as fold activation or percentage inhibition vs phospholipid concentration. The data were then fitted using GraphPad Prism (Version 8.4.1) to either of equations 1 or 2 as appropriate:

Equation 1

$$\text{Fold Activation} = \frac{\text{Maximum Activation} \cdot [\text{Cardiolipin}]^h}{S_{0.5(\text{Activation})}^h + [\text{Cardiolipin}]^h}$$

Equation 2

$$\% \text{ Inhibition} = \frac{100 \cdot [\text{Phosphatidylglycerol}]^h}{IC_{50}^h + [\text{Phosphatidylglycerol}]^h}$$

Maximum activation and $S_{0.5}$ (Activation) (Equation 1) corresponded to the degree of activation at infinite cardiolipin concentration and the cardiolipin concentration required to elicit half maximal activation respectively. IC_{50} (Equation 2) corresponds to the phosphatidylglycerol concentration that elicited half maximal inhibition. For both equations, h denoted the Hill coefficient.

Computational Studies Overview

A number of computational techniques were used in this study, to assist the reader in understanding the logistics of these methods, we have provided a summary flowchart (Supplemental Information: Figure S7).

Homology Modelling of MurM

Due to the natural ability of streptococci to undergo homologous recombination, *S. pneumoniae* MurM genes are highly mosaic, and so, in line with the enzymology studies, the MurM sequence used for homology modelling was that of *S. pneumoniae* MurM₁₅₉, *S. pneumoniae* MurM, *S. aureus* FemX (PDB ID: 6SNR) and FemA (PDB ID: 1LRZ), and *Weissella viridescens* FemX (PDB ID: 3GKR) were aligned (Supplemental Information:

Formatted: Not Highlight

Formatted: Not Highlight

Figure S1) by multiple sequence alignment using Clustal Omega to determine sequence identity (Sievers et al., 2011).

The structure of *S. aureus* FemX was used as the template for homology modelling due to its high relatedness with MurM. *S. aureus* FemX and MurM₁₅₉ sequences were aligned, and using MODELLER (Eswar et al., 2006, Martí-Renom et al., 2000, Šali and Blundell, 1993, Fiser et al., 2000) a test model was generated to verify the validity of the template and the alignment. This model was evaluated by computing its energy profile according to the DOPE-HR (high-resolution version of the Discrete Optimized Protein Energy) (Shen and Sali, 2006), smoothed via window averaging with a size of 15 residues. The profiles of template and model were compared (Supplemental Information: Figure S8), and further refinement was conducted in the region between Lys230 and Pro299, as well as in all loop regions. This optimisation was conducted by performing a very slow MD annealing on the selected regions, whilst maintaining the remaining structure. The scoring of the resulting conformations was obtained via a function built specifically to evaluate the geometry of loops. For this step, 64 different base models were created and their secondary structure was refined independently 16 times. The resulting 1024 models were evaluated and ranked using DOPE-HR as well as the SOAP (Statistically Optimized Atomic Potentials) (Dong et al., 2013). The 10 best scoring models for each score were selected and evaluated based on the number of physical constraint violations present.

The best model of MurM₁₅₉ was aligned with the previously published MurM model (Fiser et al., 2003) or *W. viridescens* Femx homologues (Fonvielle et al., 2013, Biarrotte-Sorin et al., 2004) for visualisation and analysis in PyMOL (Version 2.1.0).

Molecular docking of truncated Lipid II to MurM

A truncated Lipid II substrate (Supplemental Information: Figure S2) was created for initial molecular docking simulations. The truncated Lipid II was drawn in ChemDraw Professional (Version 17.1) and converted to a pdb file using Avogadro (Version 1.2.0). To prepare the ligand file for docking, the protonation state in H₂O at pH 7.4 was computed. Subsequently the equilibrium geometry minimizing the potential energy was computed using the general amber force field (GAFF) (Wang et al., 2004) from within the Avogadro2 software (Hanwell et al., 2012). Molecular docking was conducted using AutoDock Vina (Trott and Olson, 2010), for which pdbqt files were generated from the pdb files of receptor model and ligands using AutoDock Tools (Morris et al., 2009). Initially the location of the binding site was verified by providing the algorithm with a search space that included the entire protein. Docking was then repeated by restricting the search space to the identified binding site, in order to obtain the final docked conformation.

Molecular docking of Lipid II, Cardiolipin, Phosphatidylglycerol and Phosphatidylethanolamine to the putative MurM binding site.

Using the HADDOCK2.4 web server (Van Zundert et al., 2016), full length Lipid II, cardiolipin and phosphatidylglycerol and phosphatidylethanolamine were docked into the putative MurM binding site, where the binding site is defined by the residues Lys35, Trp38, Phe103, Arg215 and Tyr21 (Van Zundert et al., 2016).

Coarse-grained molecular dynamics simulations

All coarse-grained simulations were carried out with the GROMACS package (Version 2018) and the Martini (Version 2.2) forcefield (Abraham et al., 2015, de Jong et al., 2012). Simulations at the coarse-grained and atomistic resolutions were carried out at 313 K. For coarse-grained simulations, a stochastic velocity rescale thermostat with a coupling constant of 1:0 ps controlled the temperature.

The coordinates of the MurM homology model were used to generate a coarse-grained model using the 'martinise.py' script (de Jong et al., 2013). The protein was coarse grained to the EINE Dyn model (Periole et al., 2009) with an elastic network strength and cutoff of 500 kJmol⁻¹nm⁻² and 0.9 nm, respectively. The Lipid II model for inclusion in the membrane was parameterised using a united atom model (Gromos 53a6) generated by the Auto-mated topology builder (ATB) web-interface. Following this, the coarse-grained mapping was pursued iteratively, and the bonded terms were fitted with PyCGTOOL (Graham et al., 2017).

Since the pneumococcal membrane comprises a complex mixture of lipids, a simplified membrane composition was required for the simulations. In order to elucidate the effects of phosphatidylglycerol and cardiolipin on MurM, a non-pneumococcal lipid, phosphatidylethanolamine, was used as the majority lipid. Simulations were conducted with three different membrane systems (Supplemental Information: Table S1). System 1 comprised phosphatidylethanolamine and phosphatidylglycerol in a molar ratio of 75 % and 25 % respectively, system 2 contained phosphatidylethanolamine, phosphatidylglycerol and cardiolipin in a molar ratio of 76 %, 16 % and 8 % respectively and system 3 comprised phosphatidylethanolamine, phosphatidylglycerol and cardiolipin at a molar ratio of 72 %, 12 % and 16 % respectively. The membrane systems of size ~16x16x11:5 nm were generated with the CHARMM-GUI web interface (Jo et al., 2017). Each system was relaxed with a series of minimisation and equilibration steps with timesteps of 5-20 fs, for up to 30 ns. The equilibration steps utilised a semi-isotropic Berendsen barostat, with a 4:0 ps coupling constant (Berendsen et al., 1984). Following equilibration, Lipid II molecules (10 in total) were added to each membrane. The systems were then minimised and equilibrated (for 10 ns), followed by a 2 μ s production run to ensure sufficient mixing of all the lipid components. All production runs were carried out using a 10 fs timestep and a Parrinello-Rahman semi-isotropic barostat with a 12 ps coupling constant (Parrinello and Rahman, 1981). The Lennard-Jones potential was cutoff using the Potential shift Verlet scheme at long ranges. The reaction field method (Tironi et al., 1995) was used for electrostatics calculations, with dielectric constants of

Formatted: Not Highlight

15 and infinity for charge screening in the short- and long-range regimes, respectively. The short-range cutoff for non-bonded and electrostatic interactions was 1:2 nm. Once lipid mixing was ensured, the size of each system was increased to ~32 nm in the dimension perpendicular to the membrane and MurM was added in a random orientation around 8 nm above each membrane. Biologically relevant salt concentrations (0.15 M NaCl) were added and 10 % of the water molecules were changed to antifreeze particles to prevent localised freezing during simulations. After minimisation and 1 ns of equilibration, during which the protein backbone was restrained with 1000 kJmol⁻¹nm⁻² harmonic restraints, 6x5 μ s production runs were generated per membrane composition (Supplemental Information: Table S1).

All-atom molecular dynamics simulations

Atomistic simulations were conducted using the CHARMM36m forcefield (Huang et al., 2017). The Lipid II model used here was also used in previous work (Witzke et al., 2016), while all other lipid models were obtained from the CHARMM-GUI membrane builder module (Jo et al., 2008). For each coarse-grained membrane system, two repeats were chosen where: 1) the last frame of the production run had a distinct orientation of MurM relative to the membrane 2) MurM adhered to the membrane surface (Supplemental Information: Table S2). The last frame of the chosen coarse-grained repeats were then backmapped to the all-atom model, using the backward script (Wassenaar et al., 2014). Unfavourable ring conformers were corrected by carrying out minimisation and equilibration steps with dihedral restraints of 25000 kJmol⁻¹rad⁻² on key ring torsions. After the transformation was carried out, each system was cropped in the z dimension to a height of 16:5 nm, to remove unnecessary H₂O molecules.

Each system was minimised and equilibrated for a total of 1 ns, while the backbone of the protein was restrained with 1000 kJmol⁻¹nm⁻² harmonic restraints. Two production runs of 250 ns were carried out for each system. During the production runs a timestep of 2 fs was used, and the pressure (1 bar) regulated with a semi-isotropic Parrinello-Rahman barostat, with a coupling constant of 5:0 ps. The Lennard-Jones potential was cutoff with the Force-switch modifier from 1:0 to 1:2 nm. The short range cutoff for the electrostatic interaction was also 1:2 nm and the Particle mesh Ewald (PME) algorithm (Darden et al., 1993) was used for the long-range regime.

Analysis was carried out over the final 100 ns of each simulation, unless stated otherwise. All simulations were visualised using Visual Molecular Dynamics (VMD) or PyMOL (Version 2.2.0). Other analysis tools were written with a combination of GROMACS tools and in house scripts, that utilised the python module MDAnalysis (Gowers et al., 2016). The depletion/enrichment (D-E) indices were determined by first counting the number of lipids with a centre of geometry within 1.1 nm of the protein and then comparing this number to the number expected in the bulk of the membrane, using the procedure described by Corradi et al. (2018). The D-E index was obtained by dividing the lipid

composition in the 1.1 nm shell around the protein by the bulk membrane composition. Thus a D-E index >1 indicates enrichment, while a D-E index <1 indicates depletion. The D-E index was determined for the last 100 ns of each simulation in 50 ns blocks for all repeats. For a given membrane composition, 8 D-E indices were obtained for each lipid, from which the average and standard errors were calculated. The enrichment maps were generated by first determining the 2D density map of the membrane using the GROMACS tool densmap. Following this, the enrichment percentage was determined using the procedure described by Corradi et al. (2018). An enrichment percentage <0 % indicated that local membrane composition was depleted with respect to the bulk membrane composition. The code for the 2D enrichment maps and D-E indices was reported in Shearer et al. (2019).

QUATIFICATION AND STATISTICAL ANALYSIS

Crystallographic statistics were calculated using software/programs as described in the methods, and values are reported in Table 1. Enzyme assays were performed in duplicate, generating data that differed by no more than 10%. Average values were then plotted. The standard errors of the fits of constants defining the relationships between the response of MurM to phospholipid and phospholipid concentration according to equations 1 and 2 were calculated by GraphPad Prism (Version 8.4.1).

Supplemental Information titles and legends

Table S1. Summary of course grained simulations

Table S2. Summary of atomistic simulations. CG label refers to the coarse grained system (Table S1) from which the simulations were constructed.

Figure S1. Sequence alignment showing putative MurM binding site residues.

Alignment of *W. viridescens* FemX, *S. pneumoniae* MurM, *S. aureus* FemA and *S. aureus* FemX using CLUSTAL Omega (1.2.4). The sequence identity between MurM and *S. aureus* FemA, *S. aureus* FemX and *W. viridescens* FemX was 20.25 %, 26.93 % and 24.38 % respectively. Residues of the putative MurM binding site, proposed to interact with the Lipid II substrate are indicated by red boxes.

Figure S2: Structures of lipids investigated in these studies. A) UDP-MurNAc-pentapeptide (Lysine variant), B) Lipid II, C) Truncated Lipid II structure where the C55 prenyl chain has been replaced with a methyl group, D) cardiolipin, E) phosphatidyl-glycerol and F) phosphatidylethanolamine. All Lipid II precursors and variants contain L-Lysine at the third position of the pentapeptide chain. Structures produced in ChemDraw (Version 19.1).

Figure S3. The remaining four highest scoring poses from molecular docking of truncated Lipid II to MurM using AutoDock Vina. All possessed identical binding affinities of $-7.3 \text{ kcal}\cdot\text{mol}^{-1}$. A) and B) show the phosphate group located near the

1
2
3
4
5
6
7
8
9
10
11
12
13
14
15
16
17
18
19
20
21
22
23
24
25
26
27
28
29
30
31
32
33
34
35
36
37
38
39
40
41
42
43
44
45
46
47
48
49
50
51
52
53
54
55
56
57
58
59
60
61
62
63
64
65

entrance of the cavity, with the pentapeptide located deeper into the pocket. C) and D) show orientations that are not considered possible, since the phosphate group would be linked to the membrane embedded Lipid II, and this would prevent the phosphate from being located deep in the binding site as shown.

Figure S4. Top 3 binding poses for the docking of different lipids to the MurM binding site. Docking of A) Lipid II, B) cardiolipin, C) phosphatidylglycerol and D) phosphatidylethanolamine to the MurM binding site, where residues F103, K35, W38, R215 and Y219 are shown in yellow.

Figure S5. The association of coarse-grained MurM to the surface of the membrane. A) The minimum distance between MurM and the membrane surface for System 1 (top), System 2 (middle) and System 3 (bottom). Snapshots taken of the B) first and C) last frame of repeat 2 (r2), for System 1 (Supplemental Information: Table S1) Colour key: red = Lipid II, blue = protein, and grey = membrane.

Figure S6. Electrostatic surface representation of MurM. A) MurM showing the proposed Lipid II binding site to be positively charged (blue) B) MurM rotated 180°, showing a negatively charged surface patch. Figure prepared in PyMOL (Version 2.2.0) using the APBS Electrostatics Plugin.

Figure S7. Flow chart showing the logistics of the computational studies

Figure S8. Discrete Optimized Protein Energy Profile for MurM and FemX. Comparison of DOPE-HR profiles for MurM model (red) and FemX template (green).

References

- Abraham, M. J., Murtola, T., Schulz, R., Páll, S., Smith, J. C., Hess, B., and Lindahl, E. (2015). GROMACS: High performance molecular simulations through multi-level parallelism from laptops to supercomputers. *SoftwareX* 1, 19–25.
- Benson, T.E., Prince, D.B., Mutchler, V.T., Curry, K.A., Ho, A.M., Sarver, R.W., Hagadorn, J.C., Choi, G.H., and Garlick, R. L. (2002). X-ray crystal structure of *Staphylococcus aureus* FemA. *Structure* 10, 1107–1115.
- Berendsen, H.J., Postma, J.V., van Gunsteren, W.F., DiNola, A., and Haak, J. (1984). Molecular dynamics with coupling to an external bath. *J. Chem. Phys.* 81, 3684–3690.
- Biarrotte-Sorin, S., Maillard, A.P., Delettré, J., Sougakoff, W., Arthur, M., and Mayer, C. (2004). Crystal structures of *Weissella viridescens* FemX and its complex with UDP-MurNAc-pentapeptide: insights into FemABX family substrates recognition. *Structure* 12, 257–267.
- Bramkamp, M. and Lopez, D. (2015). Exploring the existence of lipid rafts in bacteria. *Microbiol. Mol. Biol. Rev.* R value: a novel statistical quantity for assessing the accuracy of crystal structures.
- Brünger, A.T., Free R value: a novel statistical quantity for assessing the accuracy of crystal structures. *Nature*, 355(6359):472–475, 1992.
- Bugg, T.D.H., Braddick, D., Dowson, C.G., and Roper, D.I. (2011). Bacterial cell wall assembly: still an attractive antibacterial target. *Trends Biotechnol.* 29, 167–173.
- Corradi, V., Mendez-Villuendas, E., Ingólfsson, H.I., Gu, R.-X., Siuda, I., Melo, M.N., Moussatova, A., DeGagné, L.J., Sejdiu, B.I., and Singh, G. et al. (2018). Lipid–protein interactions are unique fingerprints for membrane proteins. *ACS Cent. Sci.* 4, 709–717.
- Cressina, E., Lloyd, A.J., De Pascale, G., Roper, D.I., Dowson, C.G., and Bugg, T.D.H. (2007). Adenosine phosphonate inhibitors of lipid II: alanyl tRNA ligase MurM from *Streptococcus pneumoniae*. *Bioorg. Med. Chem. Lett.* 17, 4654–4656.
- Cressina, E., Lloyd, A.J., De Pascale, G., Mok, B.J., Caddick, S., Roper, D.I., Dowson, C.G., and Bugg, T.D.H. (2009). Inhibition of tRNA-dependent ligase MurM from *Streptococcus pneumoniae* by phosphonate and sulfonamide inhibitors. *Bioorg. Med. Chem.* 17, 3443–3455.
- Cruickshank, D. (1999). Remarks about protein structure precision. *Acta Crystallogr. D Biol. Crystallogr.* 55, 583–601.
- Darden, T., York, D., and Pedersen, L. (1993). Particle mesh Ewald: An N log (N) method for Ewald sums in large systems. *J. Chem. Phys.* 98, 10089–10092.
- de Jong, D.H., Singh, G., Bennett, W.D., Arnarez, C., Wassenaar, T.A., Schäfer, L.V., Periole, X., Tieleman, D.P., and Marrink, S.J. (2012). Improved parameters for the martini coarse-grained protein force field. *J. Chem. Theory Comput.* 9, 687–697.
- Dong, G.Q., Fan, H., Schneidman-Duhovny, D., Webb, B., and Šali, A. (2013). Optimized atomic statistical potentials: assessment of protein interfaces and loops. *Bioinformatics* 29, 3158–3166.
- Doublé, S. (1997). Preparation of selenomethionyl proteins for phase determination. *Methods Enzymol.* 276, 523–530.
- Emsley, P., Lohkamp, B., Scott, W.G., and Cowtan, K. (2010). Features and development of Coot. *Acta Crystallogr. D Biol. Crystallogr.* 66, 486–501.
- Eswar, N., Webb, B., Marti-Renom, M.A., Madhusudhan, M., Eramian, D., Shen, M.-Y., Pieper, U., and Šali, A. (2006). Comparative protein structure modeling using Modeller. *Curr. Protoc. Bioinformatics* 15, 5–6.

- 1
 - 2
 - 3
 - 4
 - 5
 - 6
 - 7
 - 8
 - 9
 - 10
 - 11
 - 12
 - 13
 - 14
 - 15
 - 16
 - 17
 - 18
 - 19
 - 20
 - 21
 - 22
 - 23
 - 24
 - 25
 - 26
 - 27
 - 28
 - 29
 - 30
 - 31
 - 32
 - 33
 - 34
 - 35
 - 36
 - 37
 - 38
 - 39
 - 40
 - 41
 - 42
 - 43
 - 44
 - 45
 - 46
 - 47
 - 48
 - 49
 - 50
 - 51
 - 52
 - 53
 - 54
 - 55
 - 56
 - 57
 - 58
 - 59
 - 60
 - 61
 - 62
 - 63
 - 64
 - 65
- Figueiredo, T.A., Sobral, R.G., Ludovice, A.M., de Almeida, J.M.F., Bui, N.K., Vollmer, W., de Lencastre, H., and Tomasz, A. (2012). Identification of genetic determinants and enzymes involved with the amidation of glutamic acid residues in the peptidoglycan of *Staphylococcus aureus*. PLoS pathog. 8, e1002508.
- Filipe S.R., and Tomasz, A. (2000). Inhibition of the Expression of Penicillin Resistance in *Streptococcus Pneumoniae* by Inactivation of Cell Wall Muropeptide Branching Genes. Proc. Natl. Acad. Sci. U S A 97, 4891–4896.
- Filipe, S.R., Pinho, M.G., and Tomasz, A. (2000). Characterization of the murMN operon involved in the synthesis of branched peptidoglycan peptides in *Streptococcus pneumoniae*. J. Biol. Chem. 275, 27768–27774.
- Filipe, S.R., Severina, E., and Tomasz, A. (2001). The role of murMN operon in penicillin resistance and antibiotic tolerance of *Streptococcus pneumoniae*. Microb. Drug Resist. 7, 303–316.
- Fiser, A., Do, R.K.G., and Šali, A. (2000). Modeling of loops in protein structures. Protein Sci. 9, 1753–1773.
- Fiser, A., Filipe, S.R., and Tomasz, A. (2003). Cell wall branches, penicillin resistance and the secrets of the MurM protein. Trends Microbiol. 11, 547–553.
- Fonvielle, M., Li de La Sierra-Gallay, I., El-Sagheer, A. H., Lecerf, M., Patin, D., Mellal, D., Mayer, C., Blanot, D., Gale, N., and Brown, T. et al. (2013). The Structure of FemXWv in Complex with a Peptidyl-RNA Conjugate: Mechanism of Aminoacyl Transfer from Ala-tRNA^{Ala} to Peptidoglycan Precursors. Angew. Chem. Int. Ed. Engl. 125, 7419–7422.
- Ganchev, D., Hasper, H., Breukink, E., and de Kruijff, B. (2006). Size and orientation of the lipid II headgroup as revealed by AFM imaging. Biochemistry, 45, 6195–6202.
- Garcia-Bustos J., and Tomasz, A. (1990). A Biological Price of Antibiotic Resistance: Major Changes in the Peptidoglycan Structure of Penicillin-Resistant pneumococci. Proc. Natl. Acad. Sci. U S A 87, 5415–5419.
- Garcia-Bustos, J., Chait, B.T. and Tomasz, A. (1987). Structure of the peptide network of pneumococcal peptidoglycan. J. Biol. Chem. 262, 15400–15405.
- Gowers, R.J., Linke, M., Barnoud, J., Reddy, T.J., Melo, M.N., Seyler, S.L., Domański, J., Dotson, D.L., Buchoux, S., and Kenney, I.M. et al. (2016). MDAnalysis: a Python package for the rapid analysis of molecular dynamics simulations. In Proceedings of the 15th Python in Science Conference (Benthall, S., and Rostrup, S. Eds.) volume 98, SciPy Austin, TX.
- Graham, J.A., Essex, J.W., and Khalid, S. (2017). PyCGTOOL: automated generation of coarse-grained molecular dynamics models from atomistic trajectories. J. Chem. Inf. Model. 57, 650–656.
- Hanwell, M.D., Curtis, D.E., Lnie, D.C., Vandermeersch, T., Zurek, E., and Hutchison, G.R. (2012). Avogadro: an advanced semantic chemical editor, visualization, and analysis platform. J. Cheminform. 4, 17.
- Hebecker, S., Krausze, J., Hasenkampf, T., Schneider, J., Groenewold, M., Reichelt, J. Jahn, D., Heinz, D.W., and Moser, J. (2015). Structures of two bacterial resistance factors mediating tRNA-dependent aminoacylation of phosphatidylglycerol with lysine or alanine. Proc. Natl. Acad. Sci. U S A 112, 10691–10696.
- Hegde, S.S., and Blanchard, J.S. (2003). Kinetic and mechanistic characterization of recombinant *Lactobacillus viridescens* FemX (UDP-N-acetylmuramoyl pentapeptide-lysine N6-alanyltransferase). J. Biol. Chem. 278, 22861–22867.

1
2
3
4
5
6
7
1041 Heuckeroth, R.O., Glaser, L., and Gordon, J.I. (1988). Heteroatom-substituted fatty acid
1042 analogs as substrates for N-myristoyltransferase: an approach for studying both the
1043 enzymology and function of protein acylation. *Proc. Natl. Acad. Sci. U S A* 85, 8795–
1044 8799.
1045
1046 Huang, J., Rauscher, S., Nawrocki, G., Ran, T., Feig, M., de Groot, B.L., Grubmüller,
1047 H., and MacKerell Jr., A.D. (2017). CHARMM36m: an improved force field for folded
1048 and intrinsically disordered proteins. *Nat. Methods* 14, 71-73.
1049 Jo, S., Kim, T., Iyer, V.G. and Im, W. (2008). CHARMM-GUI: a web-based graphical user
1050 interface for CHARMM.
1051 *J. Comput. Chem.* 29, 1859–1865.
1052
1053 Jo, S., Cheng, X., Lee, J., Kim, S., Park, S.J., Patel, D.S., Beaven, A.H., Lee, K.I., Rui,
1054 H., and Park, S. et al. CHARMM-GUI 10 years for biomolecular modeling and
1055 simulation. *J. Comput. Chem.* 38, 1114–1124.
1056
1057 Kabsch, W. (2010). XDS. *Acta Crystallogr. D Biol. Crystallogr.* 66,125–132.
1058
1059 Langer, G., Cohen, S.X., Lamzin, V.S., and Perrakis, A. (2008). Automated
1060 macromolecular model building for X-ray crystallography using ARP/wARP version 7.
1061 *Nature Protoc.* 3, 1171.
1062
1063 Lin, T.Y., Gross, W.S., Auer, G.K., and Weibel, D.B. (2019). Cardiolipin Alters
1064 *Rhodobacter sphaeroides* Cell Shape by Affecting Peptidoglycan Precursor
1065 Biosynthesis. *mBio* 10, e02401–18.
1066
1067 Lloyd, A.J., Gilbey, A.M., Blewett, A.M., De Pascale, G., El Zoeiby, A., Levesque, R.C.
1068 Catherwood, A.C., Tomasz, A., Bugg, T.D., and Roper, D.I. et al. Characterization of
1069 tRNA-dependent peptide bond formation by MurM in the synthesis of *Streptococcus*
1070 *pneumoniae* peptidoglycan. *J. Biol. Chem.* 283, 6402–6417.
1071
1072 Madeira, F., Lee, J., Buso, N., Gur, T., Madhusoodanan, N., Basutkar, P., Tivey, A.,
1073 Potter, S.C., Finn, R.D., and Lopez, R. et al. The EMBL-EBI search and sequence
1074 analysis tools APIs in 2019. (2019). *Nucleic Acids Res.* 47, W636-W641.
1075
1076 Martí-Renom, M.A., Stuart, A.C., Fiser, A., Sánchez, R., Melo, F., and Šali, A. (2000).
1077 Comparative protein structure modeling of genes and genomes. *Annu. Rev. Biophys.*
1078 *Biomol. Struct.* 29, 291–325.
1079
1080 Matsushashi, M., Dietrich, C.P., and Strominger, J.L. (1967). Biosynthesis of the
1081 Peptidoglycan of Bacterial Cell Walls III. THE ROLE OF SOLUBLE RIBONUCLEIC
1082 ACID AND OF LIPID INTERMEDIATES IN GLYCINE INCORPORATION IN
1083 *STAPHYLOCOCCUS AUREUS*. *J. Biol. Chem.* 242, 3191–3206.
1084
1085 Morlot, C., Straume, D., Peters, K., Hegnar, O.A., Simon, N., Villard, A.M., Contreras-
1086 Martel, C., Leisico, F., Breukink, E., and Gravier-Pelletier, C. et al. (2018). Structure of
1087 the essential peptidoglycan amidotransferase MurT/GatD complex from *Streptococcus*
1088 *pneumoniae*. *Nat. Commun.* 9, 3180.
1089
1090 Morrice, N.A., Gabrielli, B., Kemp, B.E., and Wettenhall, R. A cardiolipin-activated protein
1091 kinase from rat liver structurally distinct from the protein kinases C. (1994). *J. Biol.*
1092 *Chem.* 269, 20040– 20046.
1093
1094 Morris, G.M., Huey, R., Lindstrom, W., Sanner, M.F., Belew, R.K., Goodsell, D.S., and
1095 Olson, A.J. (2009). Autodock4 and AutoDockTools4: automated docking with selective
1096 receptor flexibility. *J. Comput. Chem.* 16, 2785-2791.
1097
1098 Münch, D. Roemer, T., Lee, S.H., Engeser, M., Sahl, H.G., and Schneider, T. (2012).
1099 Identification and *in vitro* analysis of the GatD/MurT enzyme-complex catalyzing lipid II
1100 amidation in *Staphylococcus aureus*. *PLoS pathog.* 8, e1002509.

1
2
3
4
5
6
7
8
9
10
11
12
13
14
15
16
17
18
19
20
21
22
23
24
25
26
27
28
29
30
31
32
33
34
35
36
37
38
39
40
41
42
43
44
45
46
47
48
49
50
51
52
53
54
55
56
57
58
59
60
61
62
63
64
65

Parrinello, M. and Rahman, A. (1981). Polymorphic transitions in single crystals: A new molecular dynamics method. *J. Appl. Phys.* 52, 7182–7190.

Peng, B., Morrice, N.A., Groenen, L.C., and Wettenhall, R.E. (1996). Phosphorylation Events Associated with Different States of Activation of a Hepatic Cardiolipin/Protease-activated Protein Kinase STRUCTURAL IDENTITY TO THE PROTEIN KINASE N-TYPE PROTEIN KINASES. *J. Biol. Chem.* 271, 32233–32240.

Periole, X., Cavalli, M., Marrink, S.J. and Ceruso, M.A. (2009). Combining an Elastic Network With a Coarse-Grained Molecular Force Field: Structure, Dynamics, and Intermolecular Recognition. *J. Chem. Theory Comput.* 5, 2531–2543.

Pesakhov, S., Benisty, R., Sikron, N., Cohen, Z., Gomelsky, P., Khozin-Goldberg, I., Dagan, R., and Porat, N. (2007). Effect of hydrogen peroxide production and the Fenton reaction on membrane composition of *Streptococcus pneumoniae*. *Biochim. Biophys. Acta* 1768, 590–597.

Purzycka-Preis, J., and Zydowo, M. (1987). Regulatory effect of pig heart phospholipids on heart muscle AMP-deaminase. *Int. J. Biochem.* 19, 565–568.

Ruiz de Mena, I., Mahillo, E., Arribas, J., and Castano, J. (1993). Kinetic mechanism of activation by cardiolipin (diphosphatidylglycerol) of the rat liver multicatalytic proteinase. *Biochem. J.* 296, 93–97.

Šali, A., and Blundell, T.L. (1993). Comparative protein modelling by satisfaction of spatial restraints. *J. Mol. Biol.* 234, 779–815.

Scheideler M., and Bell, R.M. Phospholipid dependence of homogeneous, reconstituted sn-glycerol-3-phosphate acyltransferase of *Escherichia coli*. *J. Biol. Chem.* 264, 12455–12461.

Schlame, M. (2008). Thematic Review Series: Glycerolipids. Cardiolipin synthesis for the assembly of bacterial and mitochondrial membranes. *J. Lipid Res.* 49, 1607–1620.

Schneider T., and Sahl, H.G. (2010). An oldie but a goodie – cell wall biosynthesis as antibiotic target pathway. *Int. J. Med. Microbiol.* 300, 161 – 169.

Schneider, T., Senn, M.M., Berger-Bächi, B., Tossi, A., Sahl, H.G., and Wiedemann, I. (2004). *In vitro* assembly of a complete, pentaglycine interpeptide bridge containing cell wall precursor (lipid II-Gly5) of *Staphylococcus aureus*. *Mol. Microbiol.* 53, 675–685.

Sekimizu K., and Kornberg, A. (1988). Cardiolipin activation of dnaA protein, the initiation protein of replication in *Escherichia coli*. *J. Biol. Chem.* 263, 7131–7135.

Severin A., and Tomasz, A. (1996). Naturally occurring peptidoglycan variants of *Streptococcus pneumoniae*. *J. Bacteriol.* 178, 168–174.

Shearer, J., Jefferies, D., and Khalid, S. (2019). Outer membrane proteins ompa, fhua, ompf, esta, btub, and ompx have unique lipopolysaccharide fingerprints. *J. Chem. Theory Comput.* 15, 2608–2619.

Sheldrick, G.M. (2010). Experimental phasing with SHELXC/D/E: combining chain tracing with density modification. *Acta Crystallogr. D Biol. Crystallogr.* 66, 479–485.

Shen, M.Y., and Šali, A. (2006). Statistical potential for assessment and prediction of protein structures. *Protein Sci.* 15, 2507–2524.

Sievers, F., Wilm, A., Dineen, D., Gibson, T.J., Karplus, K., Li, W., Lopez, R., McWilliam, H., Remmert, M., and Söding, J. et al. (2011). Fast, scalable generation of high-quality protein multiple sequence alignments using Clustal Omega. *Mol. Syst. Biol.* 7, 539.

Smith, A.M., and Klugman, K.P. (2001). Alterations in MurM, a cell wall mureptide branching enzyme, increase high-level penicillin and cephalosporin resistance in *Streptococcus pneumoniae*. *Antimicrob. Agents Chemother.* 45, 2393–2396.

1
2
3
4
5
6
7
1161 Smith, J.M., Dowson, C.G., and Spratt, B.G. (1991). Localized sex in bacteria. *Nature*
1162 349, 29–31.
1163
1164 Tironi, I.G., Sperb, R., Smith, P.E., and van Gunsteren, W.F. (1995). A generalized
1165 reaction field method for molecular dynamics simulations. *J. Chem. Phys.* 102, 5451–
1166 5459.
1167
1168 Tlapak-Simmons, V.L., Kempner, E.S., Baggenstoss, B.A., and Weigel, P.H. (1998).
1169 The active streptococcal hyaluronan synthases (HASs) contain a single HAS monomer
1170 and multiple cardiolipin molecules. *J. Biol. Chem.* 273, 26100–26109.
1171
1172 Tlapak-Simmons, V.L., Baggenstoss, B.A., Clyne, T., and Weigel, P.H. (1999a).
1173 Purification and lipid dependence of the recombinant hyaluronan synthases from
1174 *Streptococcus pyogenes* and *Streptococcus equisimilis*. *J. Biol. Chem.* 274, 4239–
1175 4245.
1176
1177 Tlapak-Simmons, V.L., Baggenstoss, B.A., Kumari, K., Heldermon, C. and Weigel, P.H.
1178 (1999b). Kinetic characterization of the recombinant hyaluronan synthases from
1179 *Streptococcus pyogenes* and *Streptococcus equisimilis*. *J. Biol. Chem.* 274, 4246–
1180 4253.
1181
1182 Tlapak-Simmons, V.L., Baron, C.A., and Weigel, P.H. (2004). Characterization of the
1183 purified hyaluronan synthase from *Streptococcus equisimilis*. *Biochemistry*, 43, 9234–
1184 9242.
1185
1186 Trombe, M.C., Lan  elle, M.A., and Lan  elle, G. (1979). Lipid composition of aminopterin-
1187 resistant and sensitive strains of *Streptococcus pneumoniae*. Effect of aminopterin
1188 inhibition. *Biochim. Biophys. Acta* 574, 290–300.
1189
1190 Trott, O., and Olson, A.J. (2010). AutoDock Vina: improving the speed and accuracy of
1191 docking with a new scoring function, efficient optimization, and multithreading. *J.*
1192 *Comput. Chem.* 31, 455–461.
1193
1194 Vagin, A.A., Steiner, R.A., Lebedev, A.A., Potterton, L., McNicholas, S., Long, F., and
1195 Murshudov, G.N. (2004). REFMAC5 dictionary: organization of prior chemical
1196 knowledge and guidelines for its use. *Acta Crystallogr. D Biol. Crystallogr.* 60, 2184–
1197 2195.
1198
1199 van den Brink-van der Laan, E., Boots, J.-W.P., Spelbrink, R.E., Kool, G.M., Breukink,
1200 E., Killian, J.A., and de Kruijff, B. (2003). Membrane interaction of the glycosyl-
1201 transferase MurG: a special role for cardiolipin. *J. Bacteriol.* 185, 3773–3779.
1202
1203 Van Zundert, G., Rodrigues, J., Trellet, M., Schmitz, C., Kastitis, P., Karaca, E.,
1204 Melquiond, A., vanDijk, M., De Vries, S., and Bonvin, A. (2016). The haddock2. 2 web
1205 server: user-friendly integrative modeling of biomolecular complexes. *J. Mol. Biol.* 428,
1206 720–725.
1207
1208 Wang, J., Wolf, R.M., Caldwell, J.W., Kollman, P.A., and Case, D.A. (2004). Development
1209 and testing of a general amber force field. *J. Comput. Chem.* 25, 1157–1174.
1210
1211 Wassenaar, T.A., Pluhackova, K., Bockmann, R.A., Marrink, S.J., and Tieleman, D.P.
1212 (2014). Going Backward: A Flexible Geometric Approach to Reverse Transformation
1213 from Coarse Grained to Atomistic Models. *J. Chem. Theory Comput.* 10, 676–690.
1214
1215 Weigel, P.H., Kyosseff, Z., and Torres, L.C. (2006). Phospholipid dependence and
1216 liposome reconstitution of purified hyaluronan synthase. *J. Biol. Chem.* 281, 36542–
1217 36551.
1218
1219 Williams, C.J., Headd, J.J., Moriarty, N.W., Prisant, M.G., Videau, L.L., , Deis, L.N.,
1220 Verma, V., Keedy, D.A., Hintze, B.J., and Chen, V.B. et al. (2008) MolProbity: More
1221 and better reference data for improved all-atom structure validation. *Protein Sci.* 27,
1222 293–315.

1
2
3
4
5
6
7
8
9
10
11
12
13
14
15
16
17
18
19
20
21
22
23
24
25
26
27
28
29
30
31
32
33
34
35
36
37
38
39
40
41
42
43
44
45
46
47
48
49
50
51
52
53
54
55
56
57
58
59
60
61
62
63
64
65

Winter, G. (2010) xia2: an expert system for macromolecular crystallography data reduction. J. Appl. Cryst. 43, 186–190.

Witzke, S., Petersen, M., Carpenter, T.S., and Khalid, S. (2016). Molecular Dynamics Simulations Reveal the Conformational Flexibility of Lipid II and Its Loose Association with the Defensin Plectasin in the *Staphylococcus aureus* Membrane. Biochemistry, 55, 3303–3314.

Wright, M.H., Heal, W.P., Mann, D.J., and Tate, E.W. (2010). Protein myristoylation in health and disease. J. Chem. Biol. 3, 19–35.

Zapun, A., Philippe, J., Abrahams, K.A., Signor, L., Roper, D.I., Breukink, E., and Vernet, T. (2013). *In vitro* reconstitution of peptidoglycan assembly from the Gram-positive pathogen *Streptococcus pneumoniae*. ACS Chem. Biol. 8, 2688–2696.

Figure Titles and Legends

Figure 1. The PG biosynthesis pathway. 1) The cytoplasmic stage is characterised by the formation of UDP-MurNAc-pentapeptide (UDP-MurNAc-5P) by MurA-MurC. The pentapeptide stem-peptide usually comprises L-Ala- γ -D-Glu-L-Lys-D-Ala-D-Ala in most Gram-positive organisms including the pneumococcus. 2) At the internal face of the cytoplasmic membrane MraY catalyses the formation of Lipid I from UDP-MurNAc-5P to undecaprenyl pyrophosphate, which is then converted to Lipid II by MurG. In *S. pneumoniae*, the second position D-glutamyl- α -carboxyl is amidated to D-iso-glutamine (γ -Gln) by the MurT/CatD-complex, and in some cases a dipeptide branch of either L-Ser/L-Ala or L-Ala/L-Ala may be appended at the ϵ -amino group of the third position lysine by MurM and MurN, respectively. The exact order of the cytoplasmic membrane steps remains uncertain, but here for clarity, they appear as a linear sequence, with conversion to Lipid II occurring before peptide-stem modifications, and amidation occurring before branching. Lipid II is translocated across the membrane by MurJ. 3) At the external face of the cytoplasmic membrane, PBPs form glycan chains by transglycosylation (TG), with the concomitant release of undecaprenyl pyrophosphate, and form either direct or indirect cross-links throughout the PG layer via transpeptidation (TP). Nucleotide sugars UDP-GlcNAc and UDP-MurNAc and the sugars GlcNAc and MurNAc are signified by blue, violet, dark blue and purple elongated hexagons respectively. Figure created using BioRender.com.

Figure 2. Cartoon representation of MurM predicted structure. 14 α -helices (red), 12 β -sheet (yellow) and unstructured regions (green). Best model obtained based on SOAP and DOPE scores following homology modelling using MODELLER with *S. aureus* FemX as a template. The structure was rendered in PyMOL (Version 2.2.0).

Figure 3. Surface representation of MurM binding site. A) MurM₁₅₀-model aligned and overlaid with the UDP-MurNAc-pentapeptide substrate which was co-crystallised with *W. viridescens* FemX. B) MurM₁₅₀-model with truncated Lipid II docked in the binding site, using AutoDock Vina. C) MurM₁₅₀-model with Lipid II in the binding site, from membrane simulations. Figures were created with PyMOL (Version 2.2.0) and Chimera (Version 1.13.1).

Figure 4. Lipid II binding to the putative MurM binding site. Panels A, B and C show the three simulations where Lipid II was found to bind in the putative MurM binding site. Each panel shows the MurM binding to Lipid II with respect to the membrane (top), and an enlarged image of the MurM binding to Lipid II, with the membrane removed (bottom). MurM binding site residues F103, K35, W38, R215 and Y210 are depicted in yellow, where the Lipid II head-group and prenyl chain are rendered in red and blue respectively.

Figure 5. Different conformations of Lipid II inside MurM binding site. MurM (grey) with Lipid II binding, coloured on a Blue to white to red scale with respect to simulation time, in system 5 (Table S2).

Figure 6. Interactions between MurM and membrane phospholipids. Depletion-enrichment (D-E) indices for phosphatidylethanolamine (PE), phosphatidylglycerol (PhG) and cardiolipin (CL) occurring within a 1.1 nm perimeter of the MurM protein for A) Systems 4 and 5 (molar ratio of 75 % phosphatidylethanolamine and 25 % phosphatidylglycerol), B) System 6 and 7 (molar ratio of 76 % phosphatidylethanolamine, 16% phosphatidylglycerol and 8 % cardiolipin) and C) System 8 and 9 (molar ratio of 72 % phosphatidylethanolamine, 12 % phosphatidylglycerol and 16 % cardiolipin). The D-E index was determined from 150-250 ns in 50 ns blocks for all repeats for a total of 8 values per plot. D) Example of a depletion-enrichment map with MurM at the membrane. White dots represent the center of geometry of each protein-amino acid residue, and the percentage enrichment of phospholipid is indicated by the colour. E) Activation of MurM was calculated as the product of subtraction of MurM velocity in the absence of cardiolipin ($v_{0(-C)}$) from MurM velocity in the presence of cardiolipin ($v_{0(+C)}$) divided by $v_{0(-C)}$ and was plotted versus cardiolipin concentration. F) Inhibition of MurM was calculated as $((v_{0(-PhG)}) - (v_{0(+PhG)})) / v_{0(-PhG)} \times 100$ (where PhG denotes phosphatidylglycerol) and was plotted versus phosphatidylglycerol concentration. Data were fitted as described in the text. GraphPad Prism (Version 8.4.1) and Matplotlib (Version 3.0.3) were used for data analysis and figure preparation.

Tables with Titles and Legends

Data-collection	FemX
Synchrotron radiation, detector and wavelength (Å)	Pilatus 6M-F, 0.920
Unit cell (a, b, c (Å), α , β , γ (°))	45.01, 83.62, 133.93, 90.0
Space group	P2 ₁ 2 ₁ 2 ₁
Resolution (Å)	52.27-1.62 [1.66-1.62]
Observations	422,822 [20,696]
Unique reflections	65,058 [4,782]
$I/\sigma(I)$	15.7 [2.6]
R_{sym}^a	0.065 [0.567]
R_{meas}^a	0.078 [0.600]
R_{pim}^a	0.031 [0.273]
Completeness (%)	99.7 [99.8]
Refinement	
Non-hydrogen atoms	3,307 (including 177 waters)
R_{cryst}^b	0.221 [0.262]
Reflections used	61,691 [4,531]
R_{free}^c	0.262 [0.296]
Reflections used	3,294 [244]
R_{cryst}^b (all data) ^b	0.222
Average temperature factor (Å ²)	26
Rmsds from ideal values	
Bonds (Å)	0.013
Angles (°)	1.5
DPI coordinate error (Å) ^d	0.008
Ramachandran Plot ^e	
Favoured (%)	98.0
Outliers (%)	0.0

Table 1. Summary of crystallographic data collection and refinement statistics from the *S. aureus* FemX structure. The highest resolution bin of data is indicated by square parentheses. Numbers in square

parentheses refer to values in the highest resolution shell. ^a $R_{\text{sym}} = \sum_j S_j S_h / I_{h,j} < I_h > / \sum_j S_j S_h < I_h >$ where $I_{h,j}$ is the j th observation of reflection h , and I_h is the mean intensity of that reflection. ^b $R_{\text{cytle}} = \sum_j ||F_{\text{obs}}| - |F_{\text{calc}}|| / \sum_j |F_{\text{obs}}|$ where F_{obs} and F_{calc} are the observed and calculated structure factor amplitudes, respectively. ^c R_{free} is equivalent to R_{cytle} for a 4% subset of reflections not used in the refinement (Brünger, 1992). ^dDPI refers to the diffraction component precision index (Cruickshank, 1999). ^eAs calculated by Molprobity (Williams et al., 2018).

Membrane	Available	Unavailable	Non-adherence	Lipid II in-binding site
1 (0 % CL)	4	4	4	4
2 (12 % CL)	4	4	4	2
3 (16 % CL)	3	3	0	0

Table 2. Summary of MurM adherence to and orientation on the three different membrane systems. Orientation of MurM was categorized such that the putative binding site was either available for Lipid binding (facing/close to the membrane) or unavailable for Lipid II binding (facing away from the membrane).

STAR Methods

RESOURCE AVAILABILITY

Lead Contact

Further information and requests for resources and reagents should be directed to and will be fulfilled by the Lead Contact, David Roper (David.Roper@warwick.ac.uk).

Materials Availability

This study did not generate any new unique reagents. Plasmids will be available by Materials Transfer Agreement (MTA) request in line with University of Warwick IP requirements.

Data and Code Availability

No novel code was generated during this work. Modelling scripts and raw data are available from the authors upon request.

METHOD DETAILS

Cloning, overexpression and purification of *S. aureus* FemX

The *S. aureus* Mu60 FemX gene was amplified from chromosomal DNA using Oligonucleotides FemX forward: TTTGCGGCTGCTCTCCCATGCCAAAAGATGCATATC

~~ACTAATCAGG and FemX Reverse: TTTCCGCTCCAGCCGCTGAAAATACAGCTTTC
TTTTCGTTTTTAATTTACGACATATTTTAATTTTACC. The resulting PCR fragment was
cleaved with BsaI and XhoI and cloned into pET28 between the NcoI and XhoI restriction
sites to create pET28::FemX, containing a Tobacco Etch Virus (TEV) protease cleavable
C-terminal hexa histidine tag. E. coli B834 (DE3) harbouring plasmid pRARE2 (which
supplies seven rare tRNAs to support expression of genes in E. coli) were transformed
with pET28::FemX. Transformed E. coli B834 (DE3) pRARE2 were used to inoculate M9
media supplemented with all 10 L-amino acids and 40 mM L-selenomethionine in place
in L-methionine (Doublié, 1997). Transformants were cultured at 37 °C at 180 rpm until
an optical density at 600 nm (OD₆₀₀) of 0.4–0.6 was reached. Protein expression was
induced by 1 mM isopropyl D-1-thiogalactopyranoside at 25 °C for 4 hours. Cells were
harvested by centrifugation at 6,000 xg for 15 minutes and cell pellets containing 4–6 g of
cells were resuspended in 20 mL of 50 mM sodium phosphate pH 7.0, 1M NaCl and 2.5
mg mL⁻¹ lysozyme to which one tablet of Pierce EDTA free Protease Inhibitor was added.
The cell suspension was incubated with slow rotation for 30 minutes at 4 °C before
disruption using a Bioruptor Sonopulser sonicator with 3 x 30 second bursts at 70 % power.
The lysate was clarified by centrifugation at 50,000 xg at 4 °C for 30 minutes. FemX was
then purified by immobilised metal affinity chromatography (IMAC) using a 5 mL gravity
fed column of cobalt Talon resin equilibrated with 50 mL of 50 mM sodium phosphate pH
7.0, 500 mM NaCl, 20 % (v/v) glycerol (equilibration buffer) supplemented with 10 mM
imidazole. Once the 50,000 xg supernatant was loaded onto the column, it was eluted
sequentially with 50 mL of equilibration buffer with 10 mM imidazole, 30 mL of
equilibration buffer with 50 mM imidazole and 30 mL of equilibration buffer with 200 mM
imidazole. 10 mL fractions were analysed by SDS-PAGE and those containing FemX
were pooled and concentrated, using a vivaspin 20 centrifugal concentrator (10,000
molecular weight cut off (MWCO), as required. Size exclusion chromatography in 50 mM
sodium phosphate pH 7.0, 500 mM NaCl and 20 % (v/v) glycerol was used to further
purify FemX on a Superdex 75 10/300 column. The histidine tag was then removed from
the FemX protein by digestion with histidine tagged TEV protease at a molar ratio of 100:1
FemX : TEV protease at 4 °C overnight. Cleaved and uncleaved protein were separated
by a reverse IMAC following the procedure described above.~~

FemX crystallisation and data collection

~~FemX was exchanged into 50 mM ethanolamine pH 10.0, 100 mM NaCl and 20 % (v/v)
glycerol, concentrated to 15 mg mL⁻¹ using a vivaspin 20 centrifugal concentrator column
with a 10,000 MWCO and screened for suitable crystallisation conditions using a
honeybee 063 crystallisation robot against JCSG plus, PACT primer and Morphous
crystallisation screens. Crystals obtained from the Morphous screen were used directly
for data collection experiments, although crystallization conditions were further refined to~~

0.12 M ethylene glycol, 0.1 M MES/imidazole pH 6.3 and 28 % (w/v) ethylene glycol PEG 8000. Crystals were frozen directly for X-ray diffraction data experiments on the I04-1 beamline at the Diamond synchrotron (Didcot, UK) using a Pilatus 6M F detector. Data were processed automatically using Xia2 (Winter, 2010) to 1.62 Å. Molecular replacement was not successful so selenomethionine-containing FemX protein was produced and used to obtain FemX crystals (FemX-SeMet) in the same crystallisation conditions and the structure was solved by single anomalous diffraction (Leahy et al., 1992). X-ray data from the FemX-SeMet crystal were collected on the I02 beamline at the Diamond synchrotron (Didcot, UK) using a Pilatus 6M detector. All data were indexed, integrated and scaled using the XDS package (Kabsch, 2010). All 10 of expected selenium atoms in the asymmetric unit were located and refined by the SHELX suite (Sheldrick, 2010). These sites were used to obtain preliminary phases. The starting model was built by ARP/wARP (Langer et al., 2008). This model was used to refine the higher resolution data. The structure was refined using iterative cycles of REFMAC (Vagin et al., 2004) and model building/solvent addition with COOT (Emsley et al., 2010).

Cloning, Overexpression and Purification of *S. pneumoniae*(159) MurM

As described in Lloyd et al. (2008), the MurM allele of *S. pneumoniae*(159) was cloned with a C-terminal histidine tag into pET21b and over-expressed in *E. coli* C41 (DE3)/pRIL. Cells were harvested by centrifugation and treated with 2.5 mg.mL⁻¹ non-egg white lysozyme prior to lysis. MurM was solubilised with 1 M NaCl and fractionated between 25 % and 50 % of saturation ammonium sulfate followed by purification by size exclusion chromatography with Sephacryl S-200 and by immobilized metal affinity chromatography (IMAC) using cobalt Talon resin. The purity and identity of the final products of these purifications were assessed by SDS-PAGE.

Cloning, Overexpression and Purification of *S. pneumoniae*(Pn16) AlaRS

As described in Lloyd et al. (2008), the AlaRS allele of *S. pneumoniae*(Pn16) was cloned into pET26a and over-expressed in *E. coli* BL21(DE3)-star/pRARE. The soluble protein was purified using nickel-chelated Chelating Sepharose, desalted and further purified by anion exchange chromatography on a 0.08 ml MonoQTM column. The purity and identity of the final products of these purifications were assessed by SDS-PAGE.

Preparation of MurM substrates

The substrates used for assays of MurM were prepared as follows:

Lipid II(Lys): The peptidoglycan intermediate Lipid II(Lys) (undecaprenyl pyrophosphoryl-N,N-acetyl-muramyl-(N-acetyl-glucosaminyl)-L-alanyl-γ-D-glutamyl-L-lysyl-D-alanyl-D-alanine) was prepared by re-capitulation of the peptidoglycan synthesis pathway as described (Lloyd et al. 2008).

~~[³H]-Alanyl-tRNA^{Ala}: *Micrococcus flavus* tRNA was isolated from cell pellets of *M. flavus* cultures grown to late exponential phase by phenol extraction followed by isopropanol precipitation, anion-exchange chromatography and ethanol precipitation as described by Zubay (1962) as adapted by Lloyd et al. (2008). tRNAs were renatured in 2 mM MgCl₂ at 60°C and aminoacylated with [2,3-³H] L-alanine *S. pneumoniae* (Pn16) AlaRS as described by Lloyd et al. (2008) and quantitated by liquid scintillation counting.~~

~~***S. pneumoniae* MurM-enzymology**~~

~~MurM was assayed as described by Lloyd et al. (2008) in duplicate in a final volume of 35 µl of 50 mM 3-(N-morpholino) propane sulphonic acid adjusted to pH 6.8, 30 mM KCl, 40 mM MgCl₂, 1.5 % (w/v) CHAPS (Assay Buffer), 1 mM DTT, 1 mM L-alanine, 10 µM Lipid II-Lys and 24.3 nM MurM. Reactions were initiated by the addition of 0.45 M [³H]-alanyl-tRNA^{Ala} (1000 cpm.pmol⁻¹) and were incubated at 37 °C for two minutes, over which time frame, product accumulation was linear with respect to time. Where the impact of cardiolipin or phosphatidylglycerol on MurM activity was assessed, the required amounts of 10 mg/mL stocks of each phospholipid in ethanol or chloroform/methanol (40:1) were dried down in the reaction vials the assays were to be performed in, and solubilised by addition of assay buffer. Reactions were terminated by the addition of 35 µl of ice-cold 6 M pyridinium acetate pH 4.5 and 70 µl ice-cold n-butanol. The incubations were rapidly mixed and centrifuged for 5 minutes at 1 °C at 13,000 xg, after which time the n-butanol phase was washed with 70 µl of water and then assayed for [³H]-Lipid II-L-Ala by liquid scintillation counting. Tritium counts accumulated in control reactions performed without Lipid II(Lys) were subtracted from corresponding data acquired in the presence of this substrate. MurM activities in the presence of phospholipid were related to the activity of the enzyme in the absence of phospholipid and plotted as fold activation or percentage inhibition vs phospholipid concentration. The data were then fitted using GraphPad Prism (Version 8.4.1) to either of equations 1 or 2 as appropriate:~~

~~Equation 1~~

$$\text{Fold Activation} = \frac{\text{Maximum Activation} \cdot [\text{Cardiolipin}]^h}{S_{0.5(\text{activation})}^h + [\text{Cardiolipin}]^h}$$

~~Equation 2~~

$$\% \text{ Inhibition} = \frac{100 \cdot [\text{Phosphatidylglycerol}]^h}{IC_{50}^h + [\text{Phosphatidylglycerol}]^h}$$

Maximum activation and $S_{0.5}$ (Activation) (Equation 1) corresponded to the degree of activation at infinite cardiolipin concentration and the cardiolipin concentration required to elicit half maximal activation respectively. IC_{50} (Equation 2) corresponds to the phosphatidylglycerol concentration that elicited half maximal inhibition. For both equations, h denoted the Hill coefficient.

Computational Studies Overview

A number of computational techniques were used in this study, to assist the reader in understanding the logistics of these methods, we have provided a summary flowchart (Supplemental Information: Figure S7).

Homology Modelling of MurM

Due to the natural ability of streptococci to undergo homologous recombination, *S. pneumoniae* MurM genes are highly mosaic, and so, in line with the enzymology studies, the MurM sequence used for homology modelling was that of *S. pneumoniae* MurM₁₅₀, *S. pneumoniae* MurM, *S. aureus* FemX (PDB ID: 6SNR) and FemA (PDB ID: 1LRZ), and *Weissella viridescens* FemX (PDB ID: 3GKR) were aligned (Supplemental Information: Figure S1) by multiple sequence alignment using Clustal Omega to determine sequence identity (Sievers et al., 2011).

The structure of *S. aureus* FemX was used as the template for homology modelling due to its high relatedness with MurM. *S. aureus* FemX and MurM₁₅₀ sequences were aligned, and using MODELLER (Eswar et al., 2006, Martí-Renom et al., 2000, Šali and Blundell, 1993, Fiser et al., 2000) a test model was generated to verify the validity of the template and the alignment. This model was evaluated by computing its energy profile according to the DOPE-HR (high resolution version of the Discrete Optimized Protein Energy) (Shen and Šali, 2006), smoothed via window averaging with a size of 15 residues. The profiles of template and model were compared (Supplemental Information: Figure S8), and further refinement was conducted in the region between Lys230 and Pro290, as well as in all loop regions. This optimisation was conducted by performing a very slow MD annealing on the selected regions, whilst maintaining the remaining structure. The scoring of the resulting conformations was obtained via a function built specifically to evaluate the geometry of loops. For this step, 64 different base models were created and their secondary structure was refined independently 16 times. The resulting 1024 models were evaluated and ranked using DOPE-HR as well as the SOAP (Statistically Optimized Atomic Potentials) (Dong et al., 2013). The 10 best scoring models for each score were selected and evaluated based on the number of physical constraint violations present.

The best model of MurM₁₋₁₆₀ was aligned with the previously published MurM model (Fiscor et al., 2003) or *W. viridescens* FemX homologues (Fonvielle et al., 2013; Biarrotte-Sorin et al., 2004) for visualisation and analysis in PyMOL (Version 2.1.0).

Molecular docking of truncated Lipid II to MurM

A truncated Lipid II substrate (Supplemental Information: Figure S2) was created for initial molecular docking simulations. The truncated Lipid II was drawn in ChemDraw Professional (Version 17.1) and converted to a pdb file using Avogadro (Version 1.2.0). To prepare the ligand file for docking, the protonation state in H₂O at pH 7.4 was computed. Subsequently the equilibrium geometry minimizing the potential energy was computed using the general amber force field (GAFF) (Wang et al., 2004) from within the Avogadro2 software (Hanwell et al., 2012). Molecular docking was conducted using AutoDock Vina (Trott and Olson, 2010), for which pdbqt files were generated from the pdb files of receptor model and ligands using AutoDock Tools (Morris et al., 2009). Initially the location of the binding site was verified by providing the algorithm with a search space that included the entire protein. Docking was then repeated by restricting the search space to the identified binding site, in order to obtain the final docked conformation.

Molecular docking of Lipid II, Cardiolipin, Phosphatidylglycerol and Phosphatidylethanolamine to the putative MurM binding site.

Using the HADDOCK2.4 web server (Van Zundert et al., 2016), full-length Lipid II, cardiolipin and phosphatidylglycerol and phosphatidylethanolamine were docked into the putative MurM binding site, where the binding site is defined by the residues Lys35, Trp38, Phe103, Arg215 and Tyr21 (Van Zundert et al., 2016).

Coarse-grained molecular dynamics simulations

All coarse-grained simulations were carried out with the GROMACS package (Version 2018) and the Martini (Version 2.2) forcefield (Abraham et al., 2015; de Jong et al., 2012). Simulations at the coarse-grained and atomic resolutions were carried out at 313 K. For coarse-grained simulations, a stochastic velocity rescale thermostat with a coupling constant of 1.0 ps controlled the temperature.

The coordinates of the MurM homology model were used to generate a coarse-grained model using the 'martinize.py' script (de Jong et al., 2013). The protein was coarse-grained to the ElNéDyn model (Periole et al., 2009) with an elastic network strength and cutoff of 500 kJmol⁻¹nm⁻² and 0.9 nm, respectively. The Lipid II model for inclusion in the membrane was parameterised using a united atom model (Gromos 53a6) generated by

the Automated topology builder (ATB) web interface. Following this, the coarse-grained mapping was pursued iteratively, and the bonded terms were fitted with PyCGTOOL (Graham et al., 2017).

Since the pneumococcal membrane comprises a complex mixture of lipids, a simplified membrane composition was required for the simulations. In order to elucidate the effects of phosphatidylglycerol and cardiolipin on MurM, a non-pneumococcal lipid, phosphatidylethanolamine, was used as the majority lipid. Simulations were conducted with three different membrane systems (Supplemental Information: Table S1). System 1 comprised phosphatidylethanolamine and phosphatidylglycerol in a molar ratio of 75 % and 25 % respectively, system 2 contained phosphatidylethanolamine, phosphatidylglycerol and cardiolipin in a molar ratio of 76 %, 16 % and 8 % respectively and system 3 comprised phosphatidylethanolamine, phosphatidylglycerol and cardiolipin at a molar ratio of 72 %, 12 % and 16 % respectively. The membrane systems of size $\sim 16 \times 16 \times 11.5$ nm were generated with the CHARMM-GUI web interface (Jo et al., 2017). Each system was relaxed with a series of minimisation and equilibration steps with timesteps of 5–20 fs, for up to 30 ns. The equilibration steps utilised a semi-isotropic Berendsen barostat, with a 4.0 ps coupling constant (Berendsen et al., 1984). Following equilibration, Lipid II molecules (10 in total) were added to each membrane. The systems were then minimised and equilibrated (for 10 ns), followed by a 2 μ s production run to ensure sufficient mixing of all the lipid components. All production runs were carried out using a 10 fs timestep and a Parrinello-Rahman semi-isotropic barostat with a 12 ps coupling constant (Parrinello and Rahman, 1981). The Lennard-Jones potential was cutoff using the Potential shift Verlet scheme at long ranges. The reaction field method (Tironi et al., 1995) was used for electrostatics calculations, with dielectric constants of 15 and infinity for charge screening in the short and long-range regimes, respectively. The short range cutoff for non-bonded and electrostatic interactions was 1.2 nm. Once lipid mixing was ensured, the size of each system was increased to ~ 32 nm in the dimension perpendicular to the membrane and MurM was added in a random orientation around 8 nm above each membrane. Biologically relevant salt concentrations (0.15 M NaCl) were added and 10 % of the water molecules were changed to antifreeze particles to prevent localised freezing during simulations. After minimisation and 1 ns of equilibration, during which the protein backbone was restrained with $1000 \text{ kJ mol}^{-1} \text{ nm}^{-2}$ harmonic restraints, 6 \times 5 μ s production runs were generated per membrane composition (Supplemental Information: Table S1).

All atom molecular dynamics simulations

Atomistic simulations were conducted using the CHARMM36m forcefield (Huang et al., 2017). The Lipid II model used here was also used in previous work (Witzke et al., 2016), while all other lipid models were obtained from the CHARMM-GUI membrane builder module (Jo et al., 2008). For each coarse-grained membrane system, two repeats were chosen where: 1) the last frame of the production run had a distinct orientation of MurM, relative to the membrane 2) MurM adhered to the membrane surface (Supplemental Information: Table S2). The last frame of the chosen coarse-grained repeats were then backmapped to the all-atom model, using the backward script (Wassenaar et al., 2014). Unfavourable ring conformers were corrected by carrying out minimisation and equilibration steps with dihedral restraints of $25000 \text{ kJmol}^{-1}\text{rad}^{-2}$ on key ring torsions. After the transformation was carried out, each system was cropped in the z-dimension to a height of 16.6 nm, to remove unnecessary H_2O molecules.

Each system was minimised and equilibrated for a total of 1 ns, while the backbone of the protein was restrained with $1000 \text{ kJmol}^{-1}\text{nm}^{-2}$ harmonic restraints. Two production runs of 250 ns were carried out for each system. During the production runs a timestep of 2 fs was used, and the pressure (1 bar) regulated with a semi-isotropic Parrinello-Rahman barostat, with a coupling constant of 5.0 ps. The Lennard-Jones potential was cutoff with the Force-switch modifier from 1.0 to 1.2 nm. The short range cutoff for the electrostatic interaction was also 1.2 nm and the Particle-mesh Ewald (PME) algorithm (Darden et al., 1993) was used for the long-range regime.

Analysis was carried out over the final 100 ns of each simulation, unless stated otherwise. All simulations were visualised using Visual Molecular Dynamics (VMD) or PyMOL (Version 2.2.0). Other analysis tools were written with a combination of GROMACS tools and in-house scripts, that utilised the python module MDAnalysis (Gowers et al., 2016). The depletion/enrichment (D-E) indices were determined by first counting the number of lipids with a centre of geometry within 1.1 nm of the protein and then comparing this number to the number expected in the bulk of the membrane, using the procedure described by Corradi et al. (2018). The D-E index was obtained by dividing the lipid composition in the 1.1 nm shell around the protein by the bulk membrane composition. Thus a D-E index >1 indicates enrichment, while a D-E index <1 indicates depletion. The D-E index was determined for the last 100 ns of each simulation in 50 ns blocks for all repeats. For a given membrane composition, 8 D-E indices were obtained for each lipid, from which the average and standard errors were calculated. The enrichment maps were generated by first determining the 2D density map of the membrane using the GROMACS tool densmap. Following this, the enrichment percentage was determined using the procedure described by Corradi et al. (2018). An enrichment percentage $<0\%$ indicated that local membrane composition was depleted with respect to the bulk membrane.

composition. The code for the 2D enrichment maps and D-E indices was reported in Shearer et al. (2010).

QUATIFICATION AND STATISTICAL ANALYSIS

Crystallographic statistics were calculated using software/programs as described in the methods, and values are reported in Table 1. Enzyme assays were performed in duplicate, generating data that differed by no more than 10%. Average values were then plotted. The standard errors of the fits of constants defining the relationships between the response of MurM to phospholipid and phospholipid concentration according to equations 1 and 2 were calculated by GraphPad Prism (Version 8.4.1).

Supplemental Information titles and legends

Table S1. Summary of coarse-grained simulations

Table S2. Summary of atomistic simulations. CG label refers to the coarse-grained system (Table S1) from which the simulations were constructed.

Figure S1. Sequence alignment showing putative MurM binding site residues.

Alignment of *W. viridescens* FemX, *S. pneumoniae* MurM, *S. aureus* FemA and *S. aureus* FemX using CLUSTAL Omega (1.2.4). The sequence identity between MurM and *S. aureus* FemA, *S. aureus* FemX and *W. viridescens* FemX was 20.25 %, 26.03 % and 24.38 % respectively. Residues of the putative MurM binding site, proposed to interact with the Lipid II substrate are indicated by red boxes.

Figure S2: Structures of lipids investigated in these studies. A) UDP-MurNAc-

pentapeptide (Lysine variant), B) Lipid II, C) Truncated Lipid II structure where the C55 prenyl chain has been replaced with a methyl group, D) cardiolipin, E) phosphatidyl-glycerol and F) phosphatidylethanolamine. All Lipid II precursors and variants contain Lysine at the third position of the pentapeptide chain. Structures produced in ChemDraw (Version 10.1).

Figure S3. The remaining four highest scoring poses from molecular docking of

truncated Lipid II to MurM using AutoDock Vina. All possessed identical binding affinities of $-7.3 \text{ kcal.mol}^{-1}$. A) and B) show the phosphate group located near the entrance of the cavity, with the pentapeptide located deeper into the pocket. C) and D) show orientations that are not considered possible, since the phosphate group would be linked to the membrane-embedded Lipid II, and this would prevent the phosphate from being located deep in the binding site as shown.

Figure S4. Top 3 binding poses for the docking of different lipids to the MurM binding site. Docking of A) Lipid II, B) cardiolipin, C) phosphatidylglycerol and D) phosphatidylethanolamine to the MurM binding site, where residues F103, K35, W38, R215 and Y219 are shown in yellow.

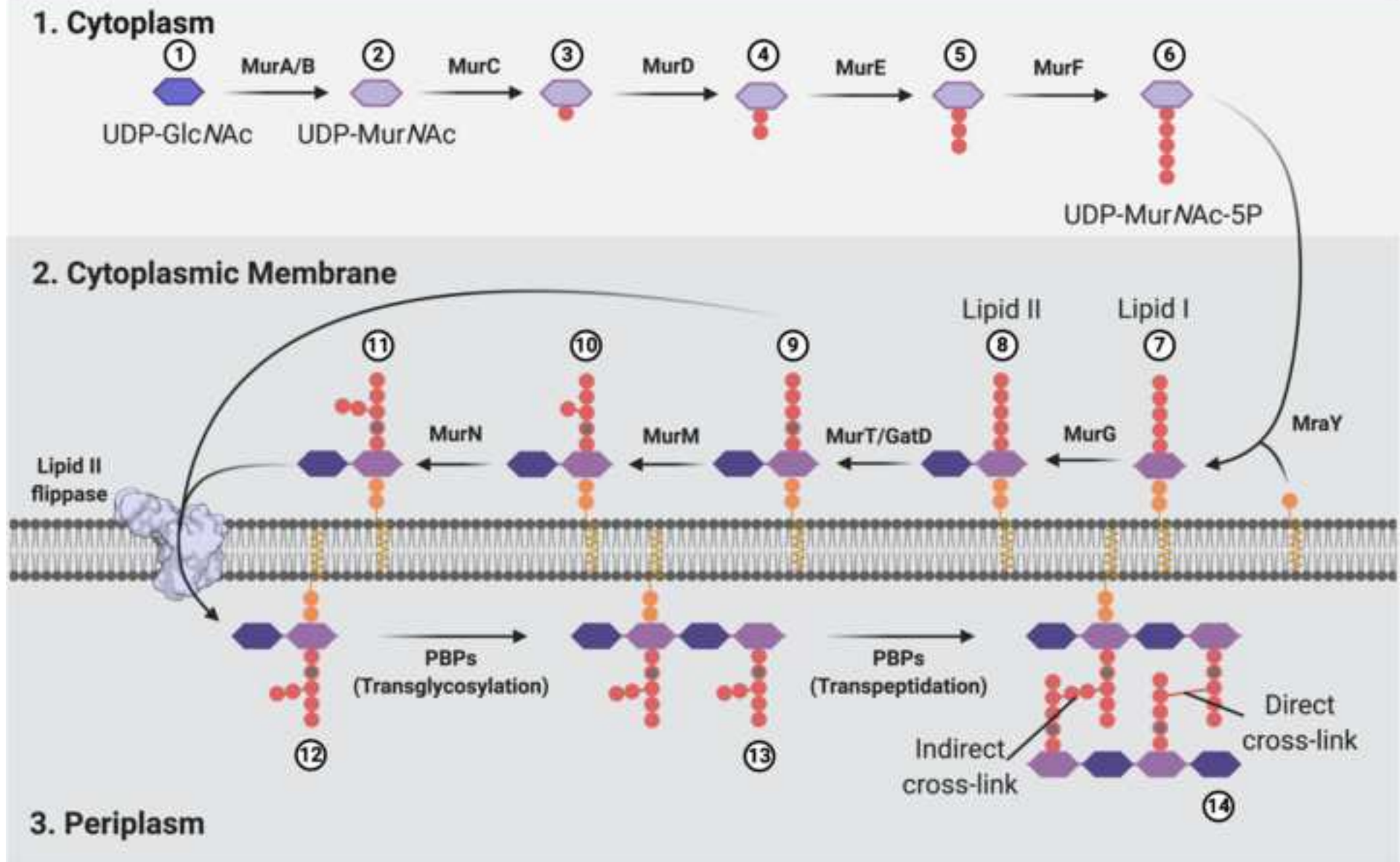
Figure S5. The association of coarse grained MurM to the surface of the membrane. A) The minimum distance between MurM and the membrane surface for System 1 (top), System 2 (middle) and System 3 (bottom). Snapshots taken of the B) first and C) last frame of repeat 2 (r2), for System 1 (Supplemental Information: Table S1) Colour key: red = Lipid II, blue = protein, and grey = membrane.

Figure S6. Electrostatic surface representation of MurM. A) MurM showing the proposed Lipid II binding site to be positively charged (blue) B) MurM rotated 180°, showing a negatively charged surface patch. Figure prepared in PyMOL (Version 2.2.0) using the APBS Electrostatics Plugin.

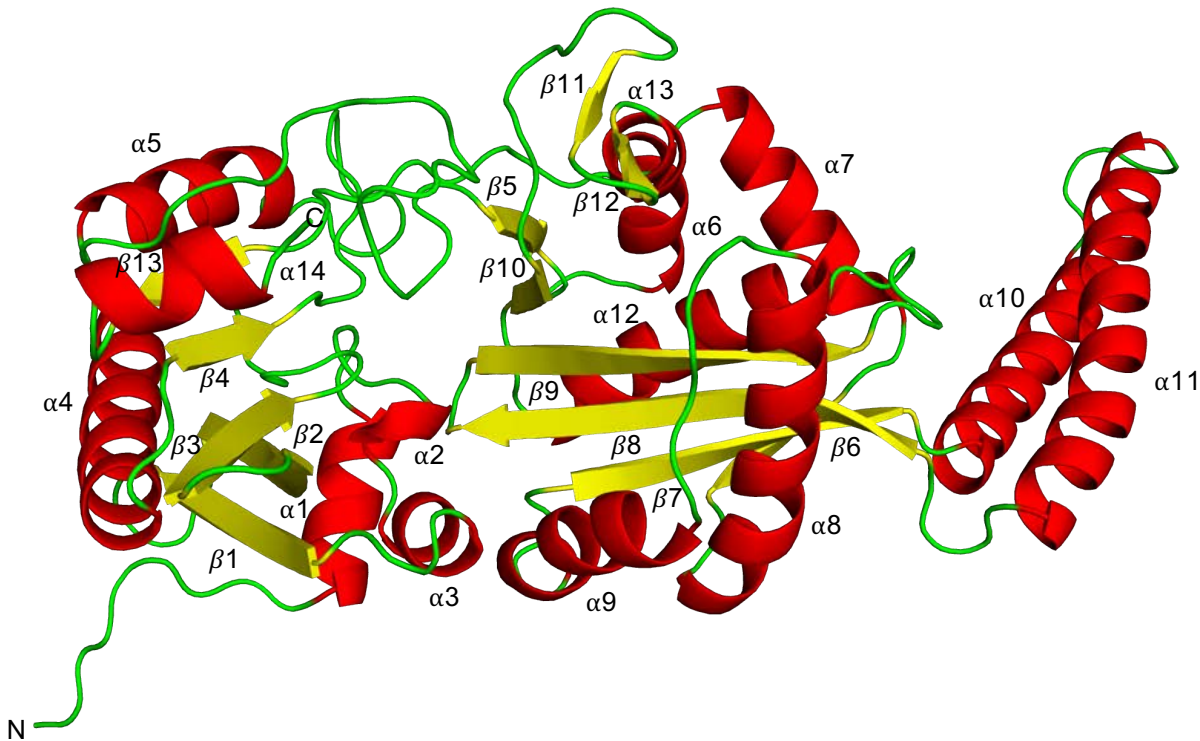
Figure S7. Flow chart showing the logistics of the computational studies

Figure S8. Discrete Optimized Protein Energy Profile for MurM and FomX. Comparison of DOPE-HP profiles for MurM model (red) and FomX template (green).

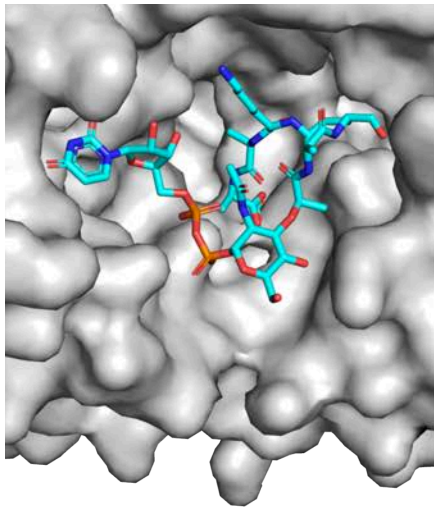
Peptidoglycan Biosynthesis Pathway in *Streptococcus pneumoniae*



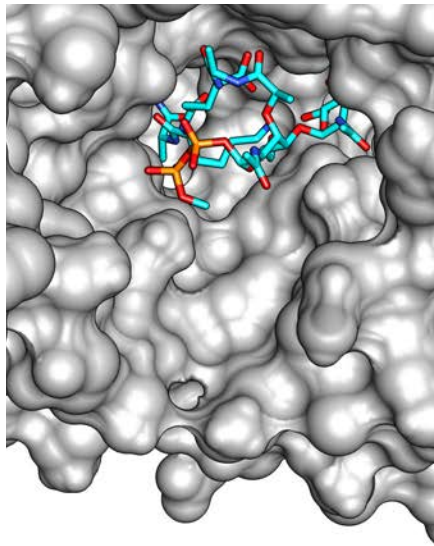
Figure



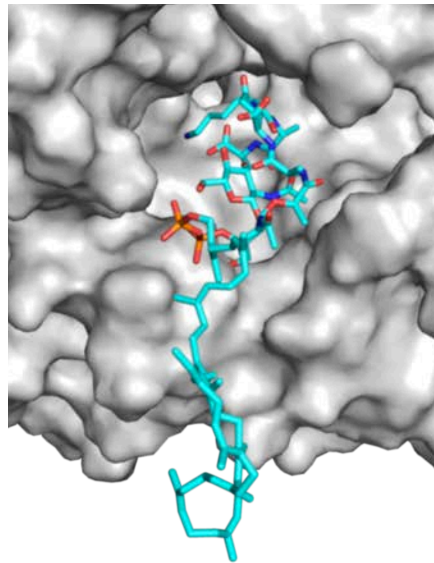
Figure



B

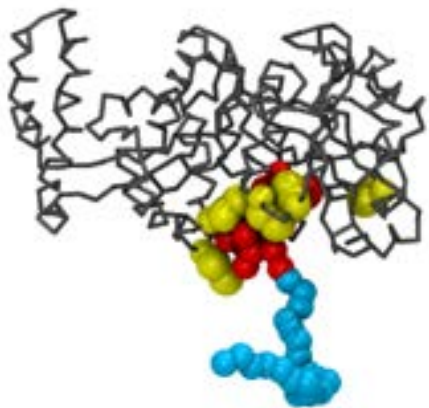
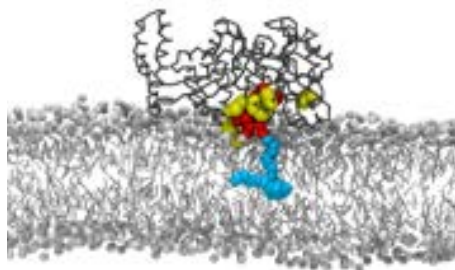


C

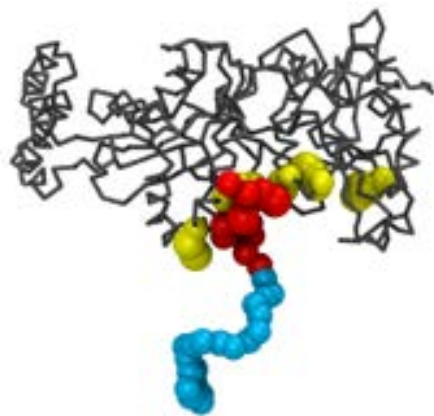


Figure

A



B



C

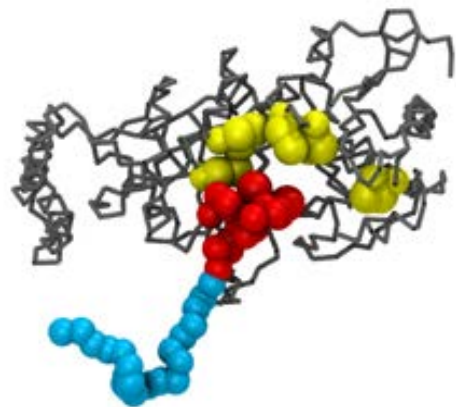
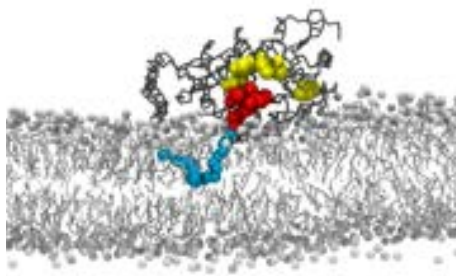
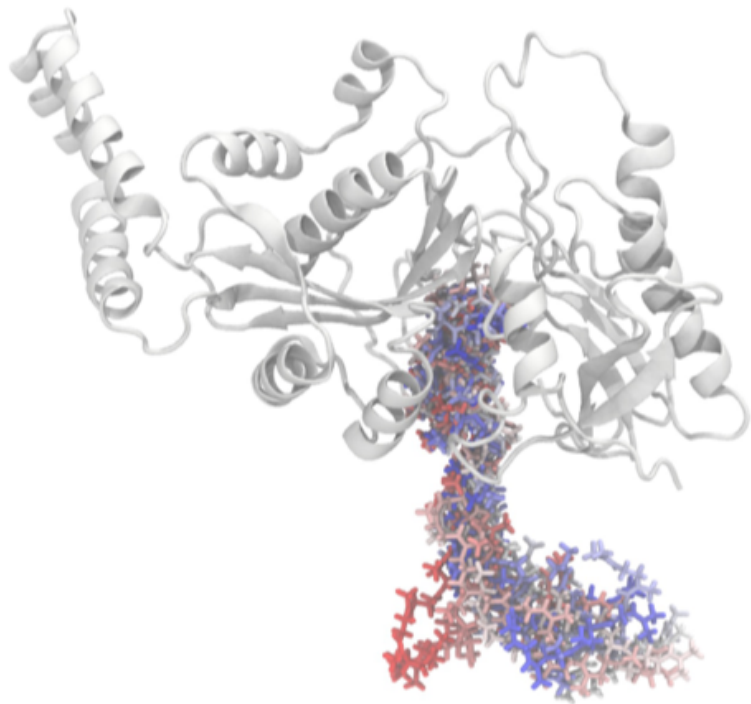


Figure
A



B

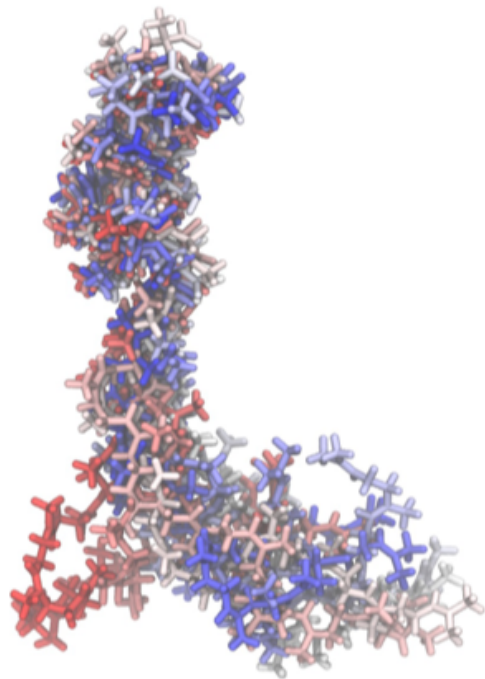
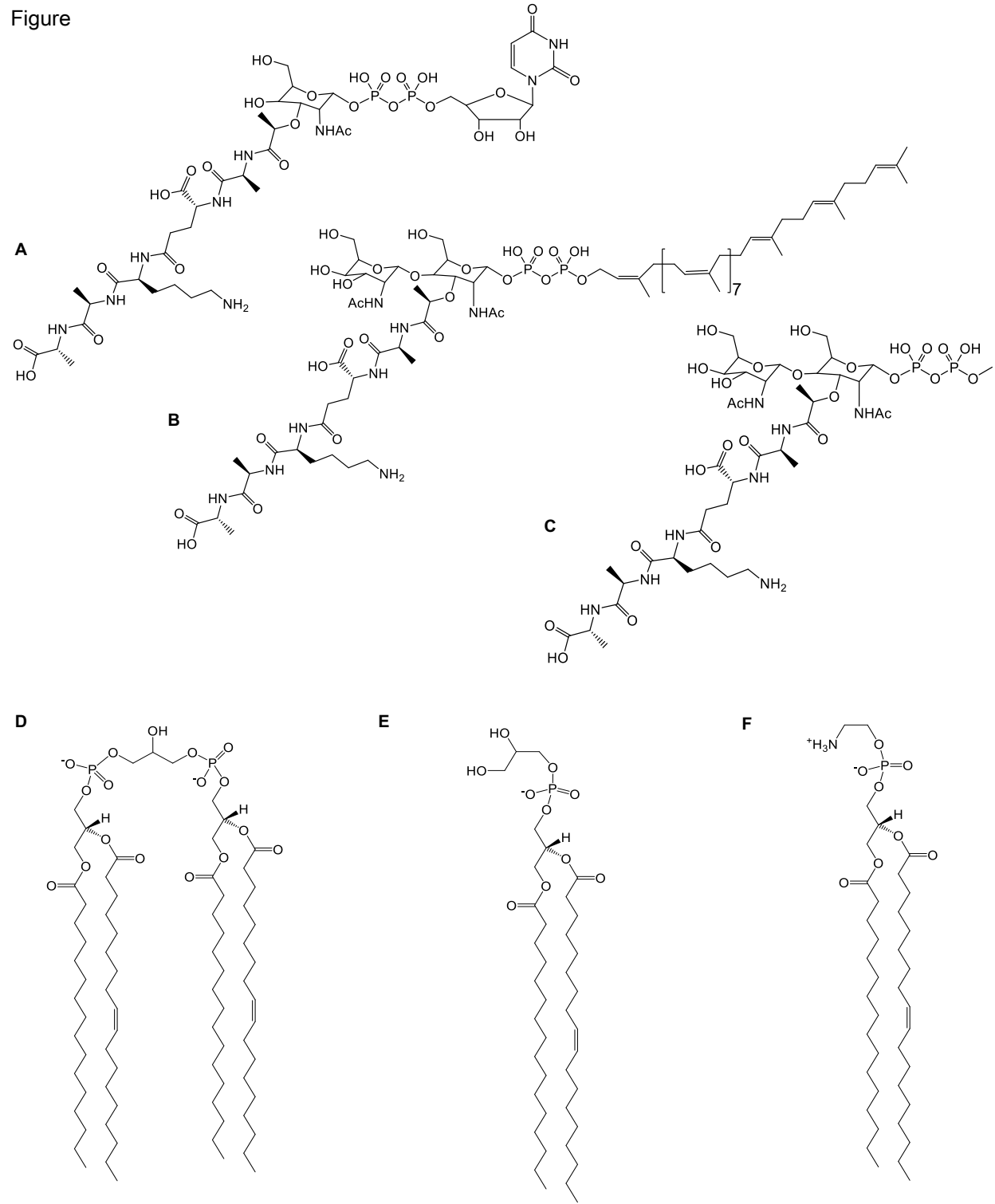
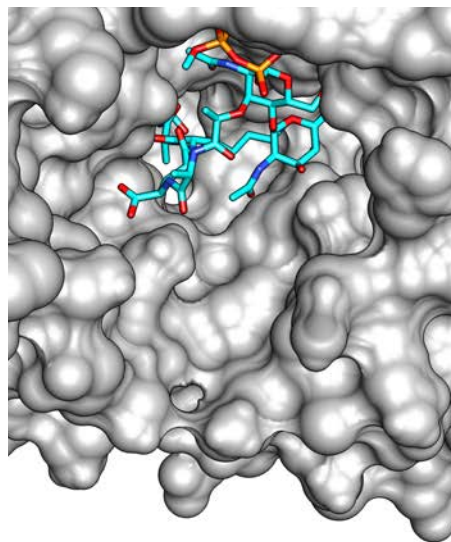


Figure		
W.vi_FemX	--MPVLNLNDPQAVERYEEFMRQSPYQVQTQDLGWAKVK--NNWEPVDVYLEDQGAIIA	56
S.pn_MurM	MYRYQLG----IPLSEYDGFVKEHPMVNLLQSSAWEKV--SD--NHERLGVYEGE-NLLA	53
S.au_FemA	--MKFTN----LTAKEFGAFTDSMPYSHFTQTVGHYELKLAEGYETHLVGIKNN--NNEV	52
S.au_FemX	--MEKMH----ITNQEHDAFVKSHPNGDLLQLTKWAETKKLTGWYARRIAVGRDG-EVQG	53
	... * . * .. * : * .: : : .	
W.vi_FemX	AMSMLLGDTPT--DKKFAYASKGPVMDVTDVDLLDRLVDEAVKA-LDGRAYVLRFDPEVA	113
S.pn_MurM	VASILIKSLPL--GYKMFYIPRGPILDYRDELLKFVLQSIKSYARSKRAVFVTFDPSIC	111
S.au_FemA	IAACLLTAVPVMKVFKYFYSNRGPVIDYENQELVHFFFNELSKYVKKHRCLYLHIDPYLP	112
S.au_FemX	VAQLLFKKVKPL-PYTLCYISRGFVVDYSNKEALNALDLSAKEITAKAEKAYAIIKIDPDVE	112
	*: * . * :*: *: : :. :. : :*: :	
W.vi_FemX	YSDEFNT-----TLQDHGYVTRNRNVADAGMHATIQPRLNMVLDLTKFPDAKTT	162
S.pn_MurM	LSQHLVNQDKREYPENLAIVEILGQLGVKWSGRTIEMDDTIQPRIQAKIYKENFEEDKL-	170
S.au_FemA	YQYLNHDGEITGNAGNDWFFDKMSNLGFEHTGFHKGFDPVLQIRYHSVLDLKDKTADDI-	171
S.au_FemX	V-----DKGTD-ALQNLKALGFKHKGFKEGLSKDYIQPRMTMITPIDKNDEL-	159
	.: : : . :	
W.vi_FemX	LDLYPSKTSKSIKRPFRDGEVHSGNSATELDEFFKTYTTMAERHGITHRPIEYFORMQA	222
S.pn_MurM	----SKSTRQAIARTARNKGLEIQYGG-LELLDSFSELMKKTEKRKEIHIRNEAYYKLLD	225
S.au_FemA	IKNMDGLRKRNTKKVKKNGVKVRFLS-EEELPIFRSFMEDTSEKAFADRDCKFYFNRLK	230
S.au_FemX	LNSFERRNRSKVRLALKRGTTVERSD-REGLKTFaelmkITGERDGFLTRDISYFENIYD	218
	: : . * :. . * * . :. : * :.:	
W.vi_FemX	AFDADTMRIF-----	232
S.pn_MurM	NFKEDSYITLTSL--DVSKRLRELEEQLEKNRVVAEKF-ND-----ATRSSKVQ	271
S.au_FemA	YYKDRVLVPLAYI--NFDEYIKELNEERDILNKDLNKALKDIEKR-PENKKAHNKRDNLQ	287
S.au_FemX	ALHEDGDAELFLVKLDPKENIAKVNQELNELHAEIAKWQQKMETSEKQAKKAQNMINDAQ	278
	. :	
W.vi_FemX	-----VAEREGKLLSTGIALKYGRKIWYMYAGSMDG-NTYYAPYA	271
S.pn_MurM	ENIKEKERLKEEIDFLQGYMMGKSNIPLAATLSLEFGNTSVNLYAGMDDDFKRYNAPIL	331
S.au_FemA	QQLDANEQKIEEGKRLQ--EEHGNELPIsagFFFINPFEVYVYAGGTSNAFRHFAGSYA	344
S.au_FemX	NKIAKNEDLKRDLALE---KEHPGEGIYLSGALLMFAGSKSYLYLGASSNEFRDPLPNHH	335
	. : : : . . : . :	
W.vi_FemX	VQSEMIQWALDNTDLYDLGGIESESTD---DSLYVFKHVFKVDAPREYIGEIDKVLDP	327
S.pn_MurM	TWYETARYAFERGMVWQNLLGGVENS-----LNGGLYQFKEKFNp-TIEEYLGEFTMPT-H	384
S.au_FemA	VQWEMINYALNHGIDRYNFYGVSGKFTEDAEDAGVVFKFKGYNA-EIIEYVGDFIKPINK	403
S.au_FemX	MQYTMMKYAREHGATTYDFGGTDNDPDKDSEHYGLWAFKKVWGT-YLSEKIGEFDYILNQ	394
	:* : . : : *: **. : * :*::	
W.vi_FemX	EVYAELVKD-----	336
S.pn_MurM	PLYPLRLALDFRKTTLRKKHRK	406
S.au_FemA	PVYAAYTALKKVKDRIF----	420
S.au_FemX	PLYQLIEQ-----	402
	:*	

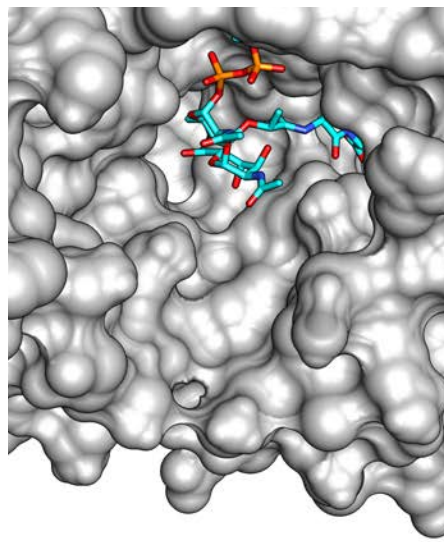
Figure



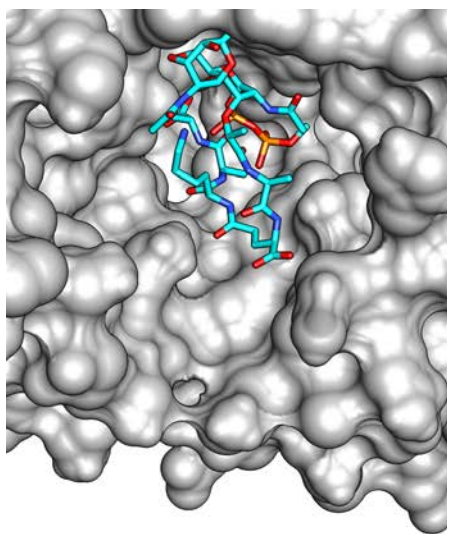
Figure



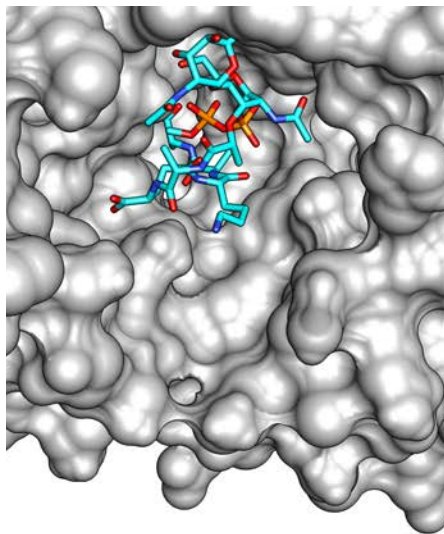
B



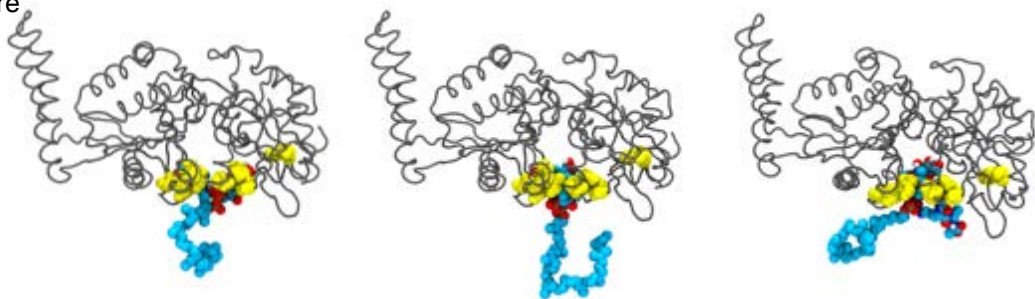
C



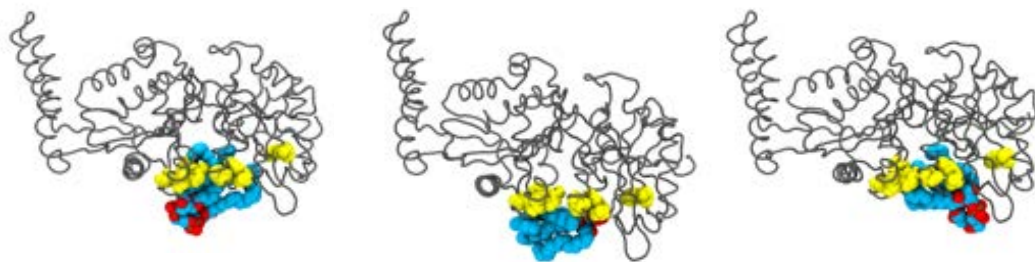
D



Figure



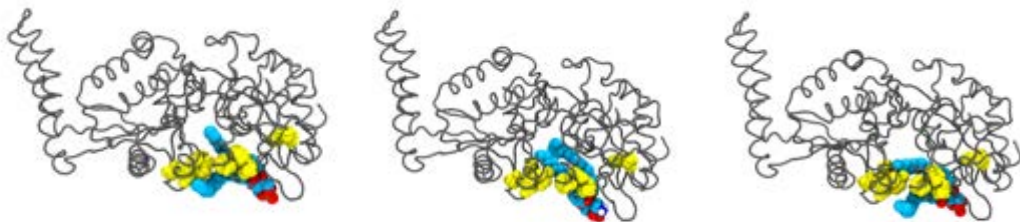
B



C



D



Figure

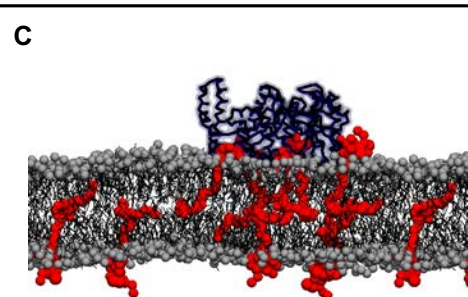
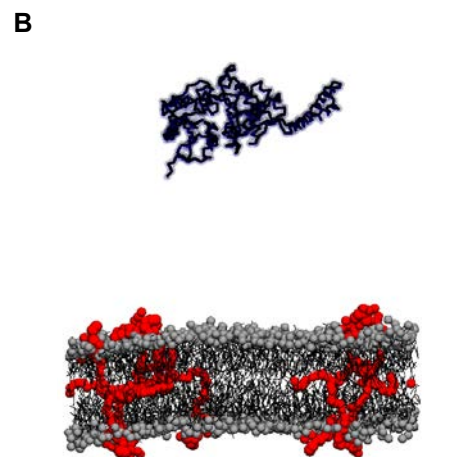
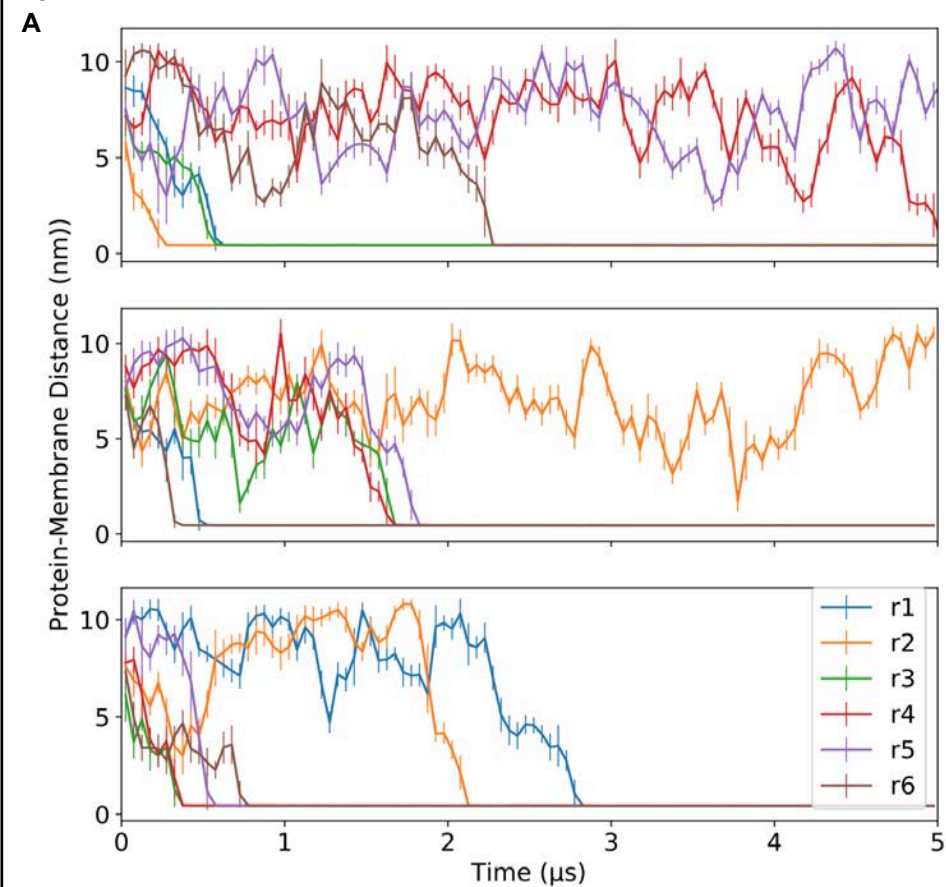
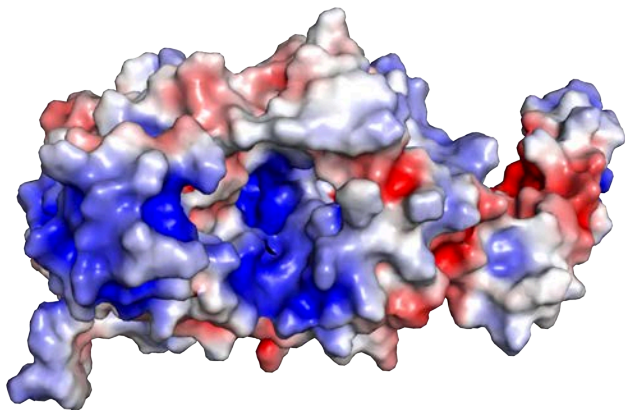
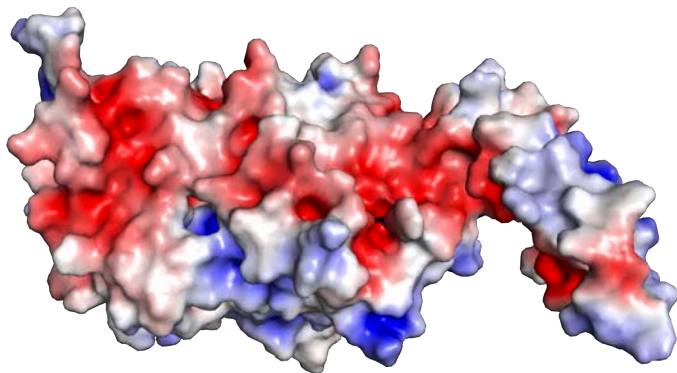


Figure
A



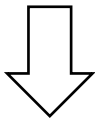
B



Figure

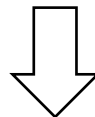
Molecular docking 1:

Docking of a truncated Lipid II to identify plausible Lipid II binding sites



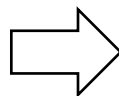
Molecular docking 2:

Docking of full length Lipid II, cardiolipin, phosphatidylglycerol and phosphatidylethanolamine to the putative MurM binding site in order to confirm specificity of lipid binding



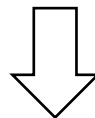
Coarse Grained (CG) MD simulations:

Orientations in which MurM adheres to the membrane, and any orientations which permit Lipid II binding are identified



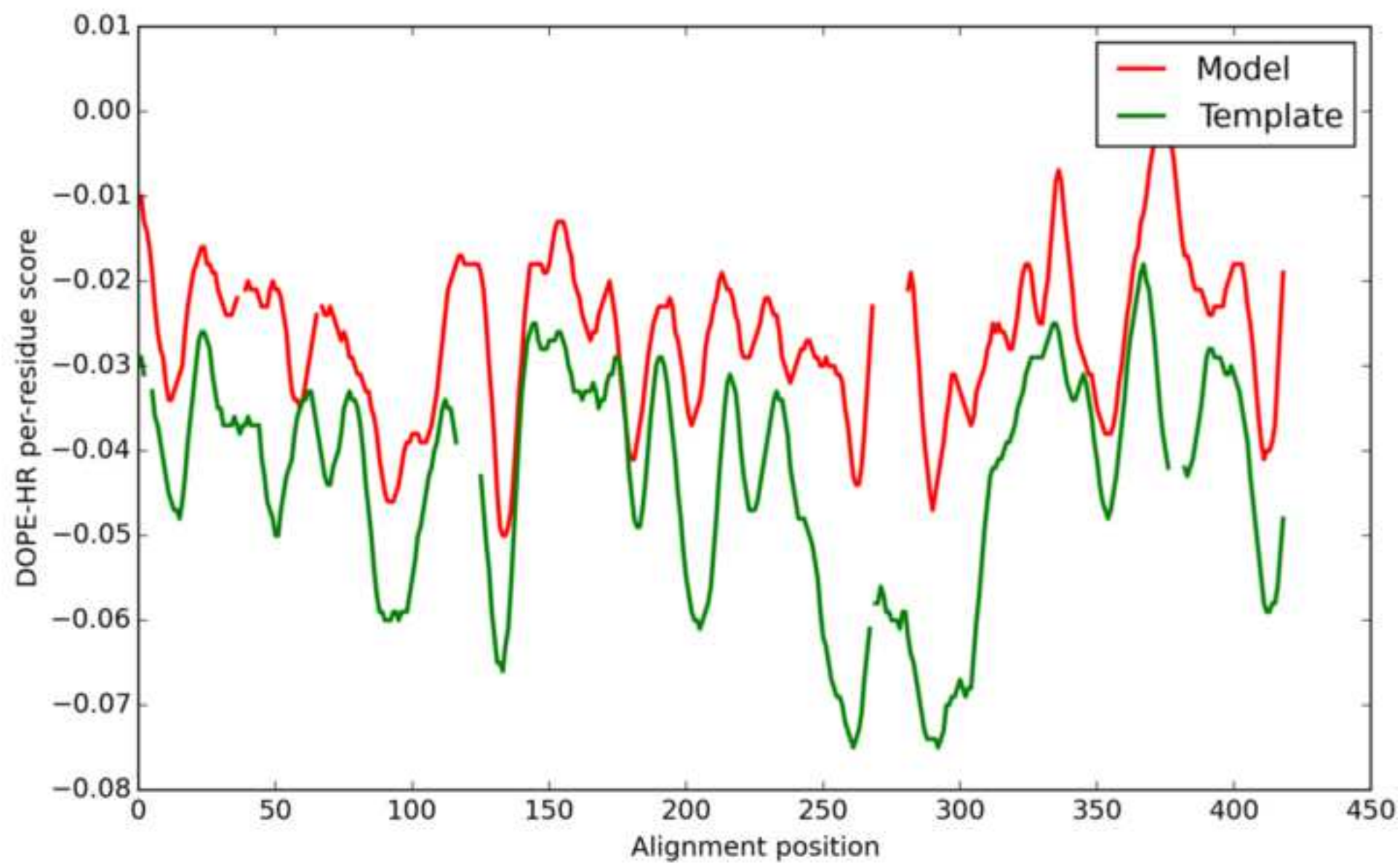
Coarse Grained (CG) MD simulations:

The impact of MurM binding upon the local membrane environment is investigated



Atomistic MD simulations:

Atomistic MD simulations are employed to refine the Lipid II-MurM complex obtained from docking and CG MD



REAGENT or RESOURCE	SOURCE	IDENTIFIER
Bacterial and Virus Strains		
<i>E. coli</i> BL21 Star (DE3): F ⁻ <i>ompT hsdS_B</i> (r _B ⁻ m _B ⁻) <i>gal dcm rne131</i> (DE3)	Invitrogen	C601003
<i>E. coli</i> B834 (DE3) - F ⁻ <i>ompT hsdS_B</i> (r _B ⁻ m _B ⁻) <i>gal dcm met</i> (DE3)	Novagen	69401
<i>E. coli</i> BL21 Star pRARE (DE3) - F ⁻ <i>ompT hsdS_B</i> (r _B ⁻ m _B ⁻) <i>gal dcm rne131 pRARE</i> (DE3)	Lloyd <i>et al.</i> (2008)	N/A
<i>E. coli</i> C41 (DE3) (a derivative of BL21(DE3) [F ⁻ <i>ampT hsdS8</i> (r8m8) <i>gal dcm</i> DE3]) pRIL (Cam ^R)	Lloyd <i>et al.</i> (2008)	N/A
<i>E. coli</i> BL21 Star pRARE (DE3) - F ⁻ <i>ompT hsdS_B</i> (r _B ⁻ m _B ⁻) <i>gal dcm rne131 pRARE2</i> (DE3)	This study	N/A
<i>E. coli</i> B834 pRARE2 (DE3) - F ⁻ <i>ompT hsdS_B</i> (r _B ⁻ m _B ⁻) <i>gal dcm met pRARE2</i> (DE3)	This study	N/A
<i>M. flavus</i> (<i>M. luteus</i>) (Stanley130.21)	NCIMB	NCIMB 8166
Chemicals, Peptides, and Recombinant Proteins		
Poly(ethylene glycol) 8000	Fluka	81272
L-Alanine, [2,3-3H]	Moravek	MT-886
Lipid II (Lys)	BACWAN/Lloyd <i>et al.</i> (2008)	C55-LII-5K
Phosphatidylglycerol L-alpha-Phosphatidyl-DL-glycerol sodium salt from egg yolk lecithin, =99% (TLC), lyophilized powder	MERCK LIFE SCIENCE UK LTD	P8318
Cardiolipin Cardiolipin sodium salt from bovine heart, =98% (TLC), lyophilized powder	MERCK LIFE SCIENCE UK LTD	C0563
JCSG-plus™ crystallization screen	Molecular Dimensions	MD1-37
PACT premier™ crystallization screen	Molecular Dimensions	MD1-29
Morpheus® crystallization screen	Molecular Dimensions	MD1-46
Cobalt TALON resin	Takara	635502
Nickel- Chelating Sepharose	Cytiva	17526801
Superdex 75 Size exclusion media	Cytiva	17104404
Sephacryl S200 size exclusion media	Cytiva	17058401
Selenomethionine	Acros Organics	259960025
Tomato etch virus (TEV) Protease	D. Roper, Structural Biology Laboratory, SLS, Warwick University.	N/A
<i>Bsa</i> I	New England Biolabs	R0535S
<i>Xho</i> I	New England Biolabs	R0146S
Hen egg white lysozyme	MERCK LIFE SCIENCE UK LTD	L6976
Deposited Data		
<i>S. aureus</i> FemX	PDB, this study	PDB: 6SNR
Oligonucleotides		

FemX Forward TTTGCGGGTGGTCTCCCATGGAAAAGATGCATATCA CTAATCAGG	IDT DNA	N/A
<i>S. aureus</i> FemX Reverse TTTGCGCTCGAGGCCCTGAAAATACAGGTTTTCTTT TCGTTTTAATTTACGAGATATTTTAATTTTAGC	IDT DNA	N/A
Recombinant DNA		
pRARE (purified from <i>Escherichia coli</i> Rosetta™ 2 (DE3))	Novagen	70954
pRARE2 (purified from <i>Escherichia coli</i> Rosetta™ 2 (DE3))	Novagen	71397
pET28a(+)	Novagen	69864
pET21b::MurM ₁₅₉	Lloyd et al., (2008)	N/A
pET26b::alaRS	Lloyd et al., (2008)	N/A
pET28::FemX	This study	N/A
Software and Algorithms		
GraphPad Prism Version 8.4.1.	GraphPad Software, San Diego, CA, USA.	www.graphpad.com
Xia2	Winter (2010)	https://xia2.github.io/
XDS package	Kabsch (2010)	http://xds.mpimf-heidelberg.mpg.de
SHELX suite	Sheldrick (2010)	https://www.shelxle.org/shelx/eingabe.php
ARP/wARP	Langer et al., (2008)	https://www.embl-hamburg.de/ARP/
REFMAC	Vagin et al., (2004)	https://www2.mrc-lmb.cam.ac.uk/groups/murshudov/content/refmac/refmac.html
COOT	Emsley et al., (2010)	https://www2.mrc-lmb.cam.ac.uk/personal/pemsley/coot/
MODELLER	Eswar et al., (2006); Marti-Renom et al., (2000); Sali and Blundell (1993); Fiser et al., (2000)	https://salilab.org/modeller/
Chimera (Version 1.13.1)		https://www.cgl.ucsf.edu/chimera/
Discrete Optimized Protein Energy (DOPE-HR)	Shen and Sali (2006)	
Statistically Optimized Atomic Potentials (SOAP)	Dong et al., (2013)	https://github.com/salilab/SOAP
PyMOL (Version 2.2.0)		https://pymol.org/2/#download

Avogadro2 software	Hanwell <i>et al.</i> , (2012)	https://www.openchemistry.org/downloads/
AutoDock Vina	Trott and Olson., (2010)	http://vina.scripps.edu/download.html
HADDOCK web server	Van Zundert et al., (2016)	https://bianca.science.uu.nl/haddock2.4/
GROMACS package (Version 2018)	Abraham et al., (2015)	http://www.gromacs.org/
Auto-mated topology builder (ATB) web-interface		https://atb.uq.edu.au/
PyCGTOOL		https://pypi.org/project/pycgtool/
CHARMM-GUI web interface	Jo et al., (2017)	http://charmm-gui.org/
backward script	Wassenaar et al., (2014)	http://www.cgmartin.nl/index.php/downloads/tools/240-backward
Particle mesh Ewald (PME) algorithm	Darden et al., (1993)	
Visual Molecular Dynamics (VMD)		https://www.ks.uiuc.edu/Research/vmd/
Other		

Table S1. Summary of course grained simulations

System	Membrane size (nm)	Time (μs)	Membrane % Composition		
			PE	PhG	CL
1	16.1x16.1	6x5	75	25	0
2	16.1x16.1	6x5	76	16	8
3	16.3x16.3	6x5	72	12	16

Table S2. Summary of atomistic simulations.

CG label refers to the coarse grained system (Table S1) from which the simulations was constructed.

System	Time (μs)	CG Label
4	2x0.25	1 r1
5	2x0.25	1 r2
6	2x0.25	2 r1
7	2x0.25	2 r6
8	2x0.25	3 r1
9	2x0.25	3 r4

W.vi_FemX	--MPVLNLNDPQAVERYEEFMRQSPYQVTDQLGWAKVK--NNWEPVDVYLEDDQGAIIA	56
S.pn_MurM	MYRYQLG----IPLSEYDGFVKEHPMVNLLQSSAWEKVK--SDNNHERLGVYEGE-NLLA	53
S.au_FemA	--MKFTN----LTAKEFGAFTDSMPYSHFTQTGVGHYELKLAEGYETHLVGIKNN--NNEV	52
S.au_FemX	--MEKMH----ITNQEHDAFVKSHPNGDLLQLTKWAETKKLTGWYARRIAVGRDG-EVQG	53
	... * . * .. * : * .: : : .	
W.vi_FemX	AMSMMLGDTPT--DKKFAYASKGPVMDVTDVLLDRLVDEAVKA-LDGRAYVLRFDPEVA	113
S.pn_MurM	VASILIKSLPL--GYKMFYIPRGPILDYRDTELLKFVLQSIKSYARSKRAVFTFDPSIC	111
S.au_FemA	IAACLLTAVPVMKVFKYFYSNRGPVIDYENQELVHFFFNELSKYVKKHRCCLYLHIDPYLP	112
S.au_FemX	VAQLLFKKVPKL-PYTLCYISRGFVVDYSNKEALNALDSAKEIAKAEKAYAIIKIDPDVE	112
	*: * . * :*: : : : : : ** :	
W.vi_FemX	YSDEFNT-----TLQDHGYVTRNRNVADAGMHATIQPRLNMVLDLTKFPDAKTT	162
S.pn_MurM	LSQHLVNQDKREYPENLAIVEILGQLGVKWSGRTIEMDDTIQPRIQAKIYKENFEEDKL-	170
S.au_FemA	YQYLNHDGEITGNAGNDWFFDKMSNLGFEHTGFHKGFDPVLQIRYHSVLDLKDKTADDI-	171
S.au_FemX	V-----DKGTD-ALQNLKALGFKHKGFKGLSKDYIQPRMTMITPIDKNDEL-	159
	: : : . : : . .	
W.vi_FemX	LDLYPSKTKSKIKRPFDRGVEVHSGNSATELDEFFKTYTTMAERHGITHRPIEYFQRMQA	222
S.pn_MurM	----SKSTRQAIRTARNKGLEIQYGG-LELLDSFSELMKKTEKRKEIHIENEAYYKKLLD	225
S.au_FemA	IKNMDGLRKRNTKKVKKNGVKVRFSL-EEELPIFRSFMEDTSESKAFAADRDCKFYFNRLK	230
S.au_FemX	LNSFERRNRSKVRLLALKRGTTVERSD-REGLKTFaelMKITGERDGFLLTRDISYFENIYD	218
	: : . * :. . * * . : . : * : : .	
W.vi_FemX	AFDADTMRIF-----	232
S.pn_MurM	NFKEDSYITLTSL--DVKRLRELEEQLKNRVVAEKF-ND-----ATRSSKVQ	271
S.au_FemA	YYKDRVLVPLAYI--NFDEYIKELNEERDILNKDLNKALKDIEKR-PENKKAHNKRDNLQ	287
S.au_FemX	ALHEDGDAELFLVKLDPKENIAKVNQELNELHAEIAKWQQKMETSEKQAKKAQNMINDAQ	278
	. :	
W.vi_FemX	-----VAEREGKLLSTGIALKYGRKIWYMYAGSMDG-NTYYAPYA	271
S.pn_MurM	ENIKEKERLKEEIDFLQGYMMNGKSNIPLAATLSLEFGNTSVNLYAGMDDDFKRYNAPIL	331
S.au_FemA	QQLDANEQKLEEGKRLQ---EEHGNELPISAGFFFINPFEVYVYAGGTSNAFRHFAGSYA	344
S.au_FemX	NKIAKNEDLKRDLALEA---KEHPEGIYLSGALLMFAGSKSYLYGASSNEFRDFLPNHH	335
	. : : : . . : . :	
W.vi_FemX	VQSEMIQWALDTNTDLYDLGGIESESTD---DSLIVFKHVFKVDAPREYIGEIDKVLDP	327
S.pn_MurM	TWYETARYAFERGMVWQNLGGVENS-----LNGGLYQFKEKFNPTIEEYLGEFTMPT-H	384
S.au_FemA	VQWEMINYALNHGIDRYNFYGVSGKFTEDAEDAGVVKFKKGYNA-EIIEYVGDFIKPINK	403
S.au_FemX	MQYTMMKYAREHGATTYDFGGTDNDPDKDSEHYGLWAFKKVWGT-YLSEKIGEFDYILNQ	394
	.* : . : : * . . . : : ** . : * :*::	
W.vi_FemX	EVYAEELVKD-----	336
S.pn_MurM	PLYPLRLALDFRKTLRKKHRK	406
S.au_FemA	PVYAAYTALKKVKDRIF-----	420
S.au_FemX	PLYQLIEQ-----	402
	: *	

Figure S1. Sequence alignment showing putative MurM binding site residues. Alignment of *Weissella viridescens* FemX, *Streptococcus pneumoniae* MurM, *Staphylococcus aureus* FemA and *Staphylococcus aureus* FemX using CLUSTAL Omega (1.2.4). The sequence identity between MurM and *Staphylococcus aureus* FemA, *Staphylococcus aureus* FemX and *Weissella viridescens* FemX was 20.25 %, 26.93 % and 24.38 % respectively. Residues of the putative MurM binding site, proposed to interact with the Lipid II substrate are indicated by red boxes.

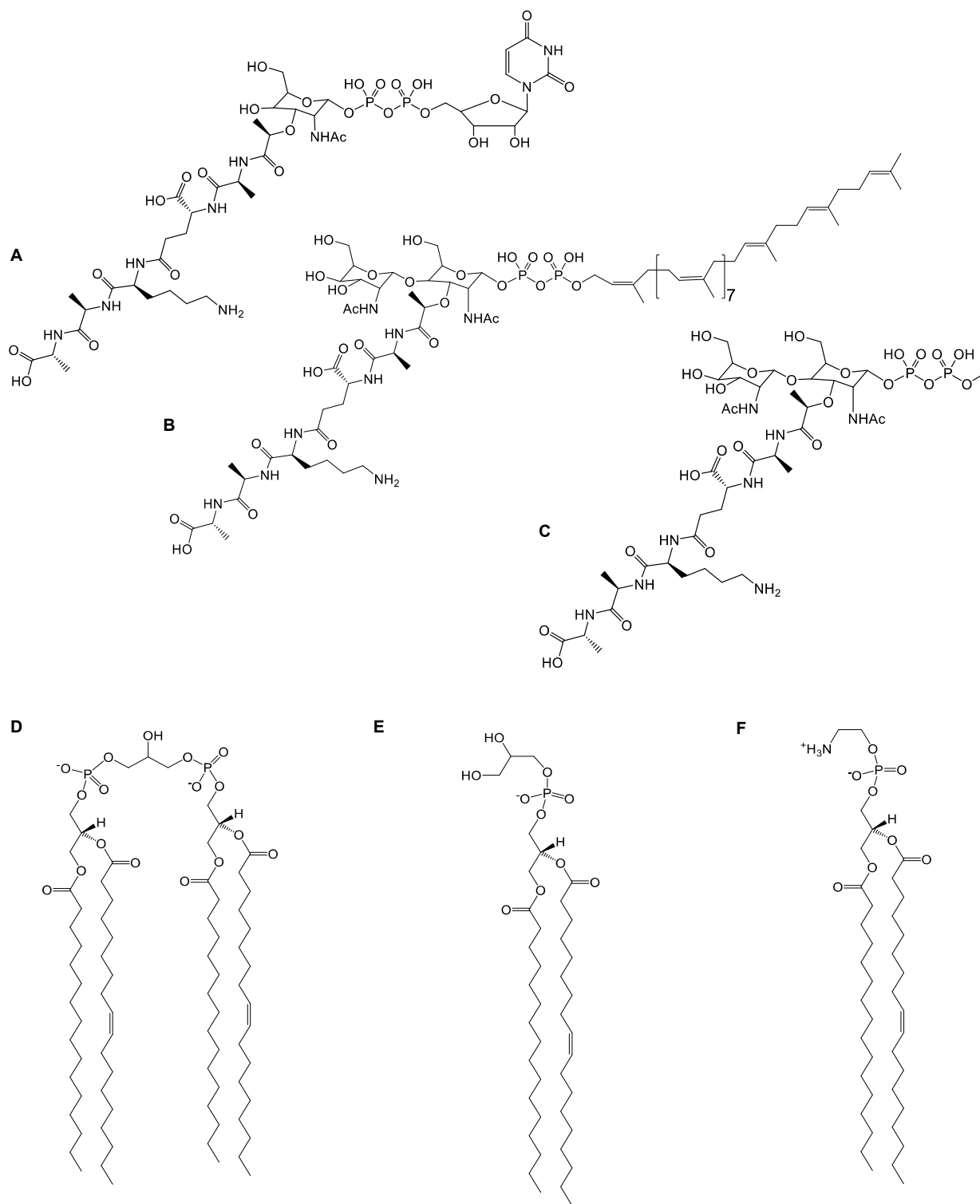


Figure S2: Structures of lipids investigated in these studies. A) UDP-MurNAc-pentapeptide (Lysine variant), B) Lipid II, C) Truncated Lipid II structure where the C55 prenyl chain has been replaced with a methyl group, D) Cardiolipin, E) Phosphatidylglycerol and F) Phosphatidylethanolamine. All Lipid II precursors and variants contain L-Lysine at the third position of the pentapeptide chain. Structures produced in ChemDraw (Version 19.1).

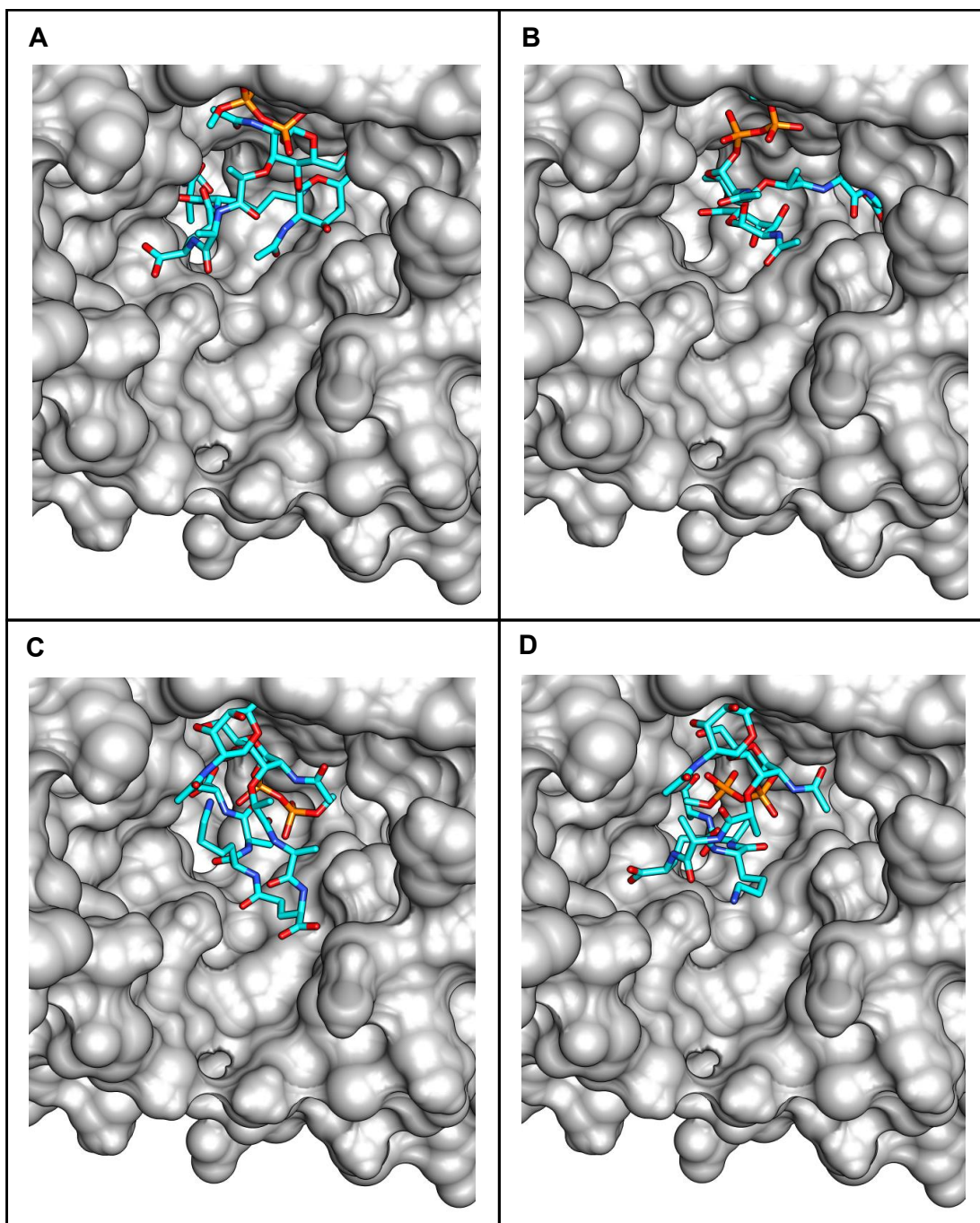


Figure S3. The remaining four highest scoring poses from molecular docking of truncated Lipid II to MurM using AutoDock Vina. All possessed identical binding affinities of -7.3 kcal.mol⁻¹. A) and B) show the phosphate group located near the entrance of the cavity, with the pentapeptide located deeper into the pocket. C) and D) show orientations that are not considered possible, since the phosphate group would be linked to the membrane embedded Lipid II, and this would prevent the phosphate from being located deep in the binding site as shown.

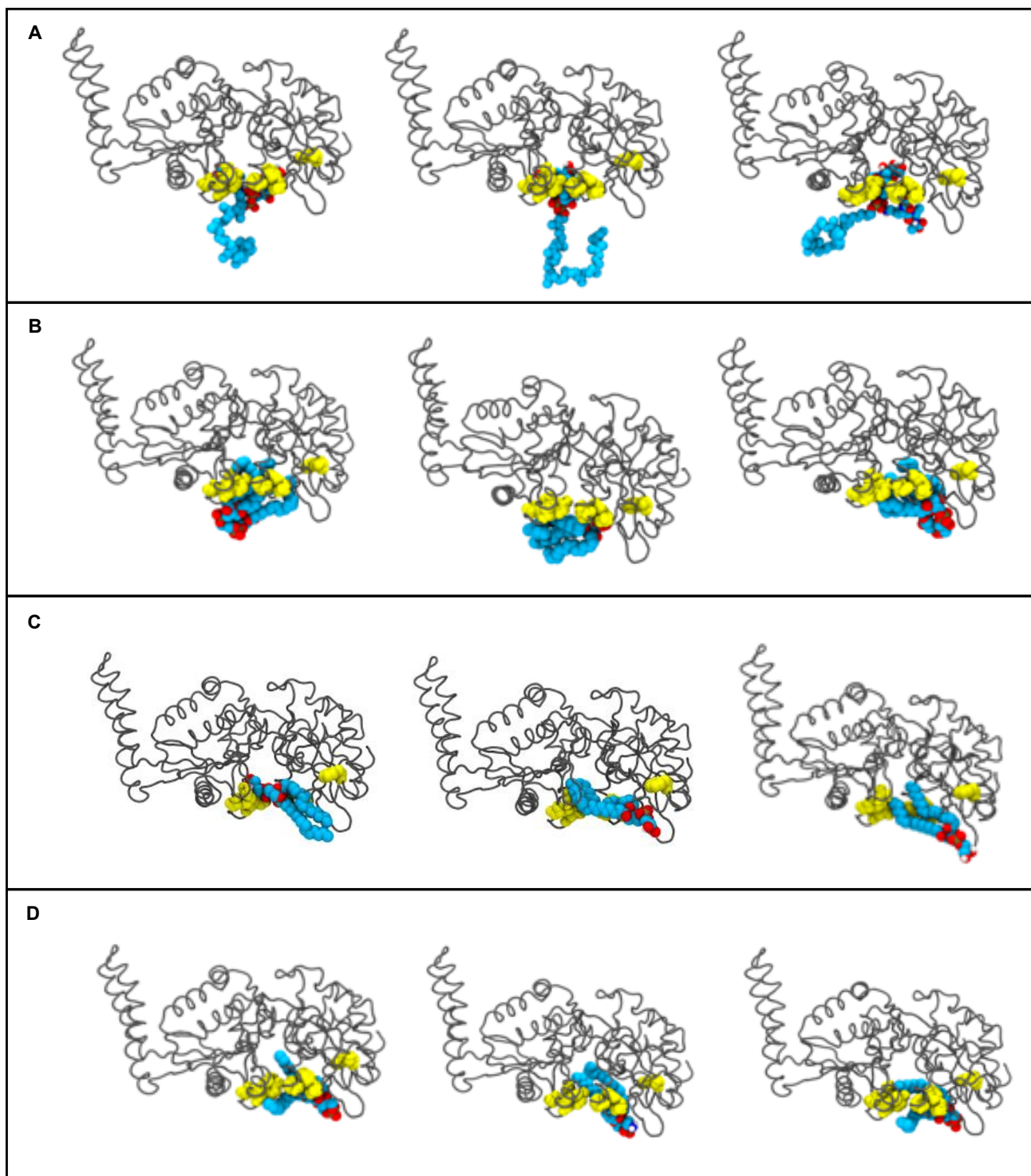


Figure S4. Top 3 binding poses for the docking of different lipids to the MurM binding site. Docking of A) Lipid II, B) Cardiolipin, C) Phosphatidylglycerol and D) Phosphatidylethanolamine to the MurM binding site, where residues F103, K35, W38, R215 and Y219 are shown in yellow.

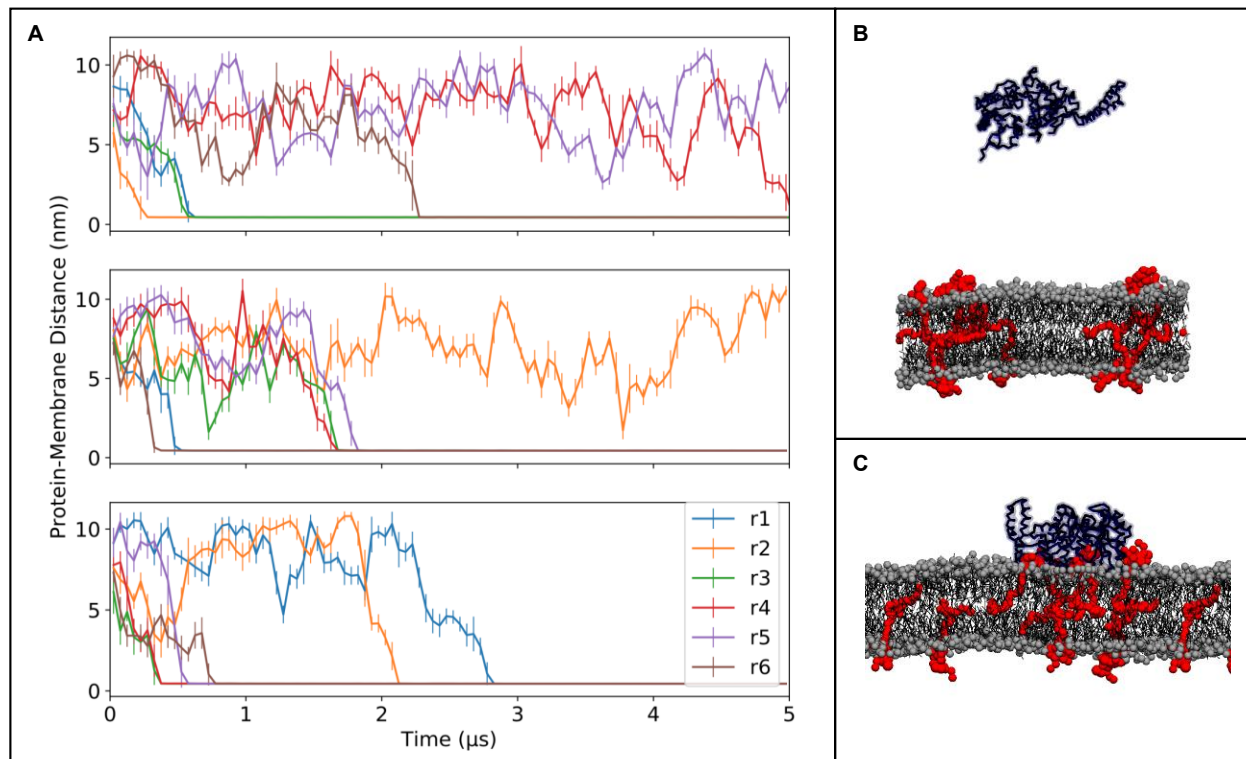


Figure S5. The association of coarse-grained MurM to the surface of the membrane. A) The minimum distance between MurM and the membrane surface for System 1 (top), System 2 (middle) and System 3 (bottom). Snapshots taken of the B) first and C) last frame of repeat 2 (r2), for System 1 (Supplemental Information: Table S1) Colour key: red = Lipid II, blue = protein, and grey = membrane.

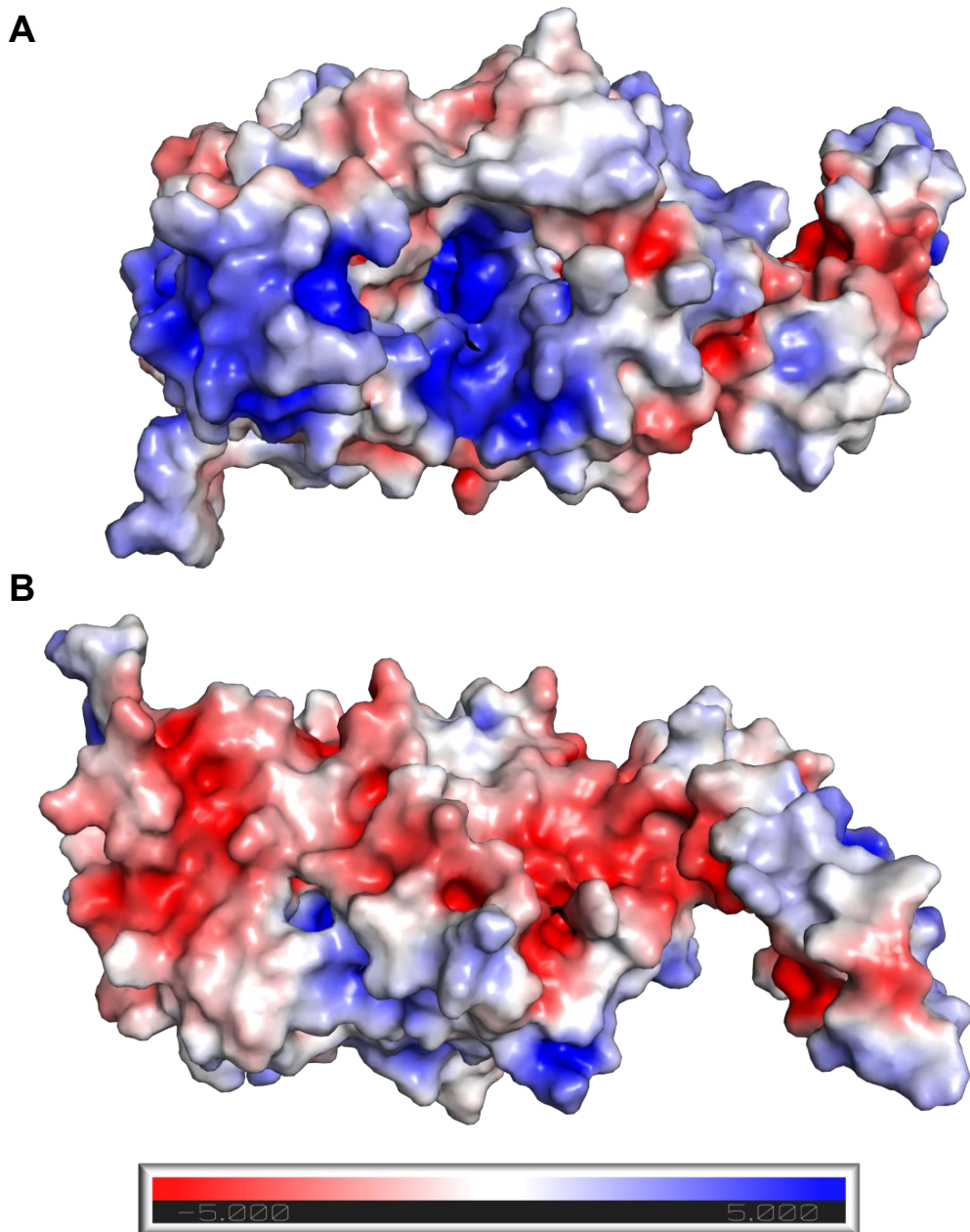


Figure S6. Electrostatic surface representation of MurM. A) MurM showing the proposed Lipid II binding site to be positively charged (blue) B) MurM rotated 180°, showing a negatively charged surface patch. Figure prepared in PyMOL (Version 2.2.0) using the APBS Electrostatics Pluggin.

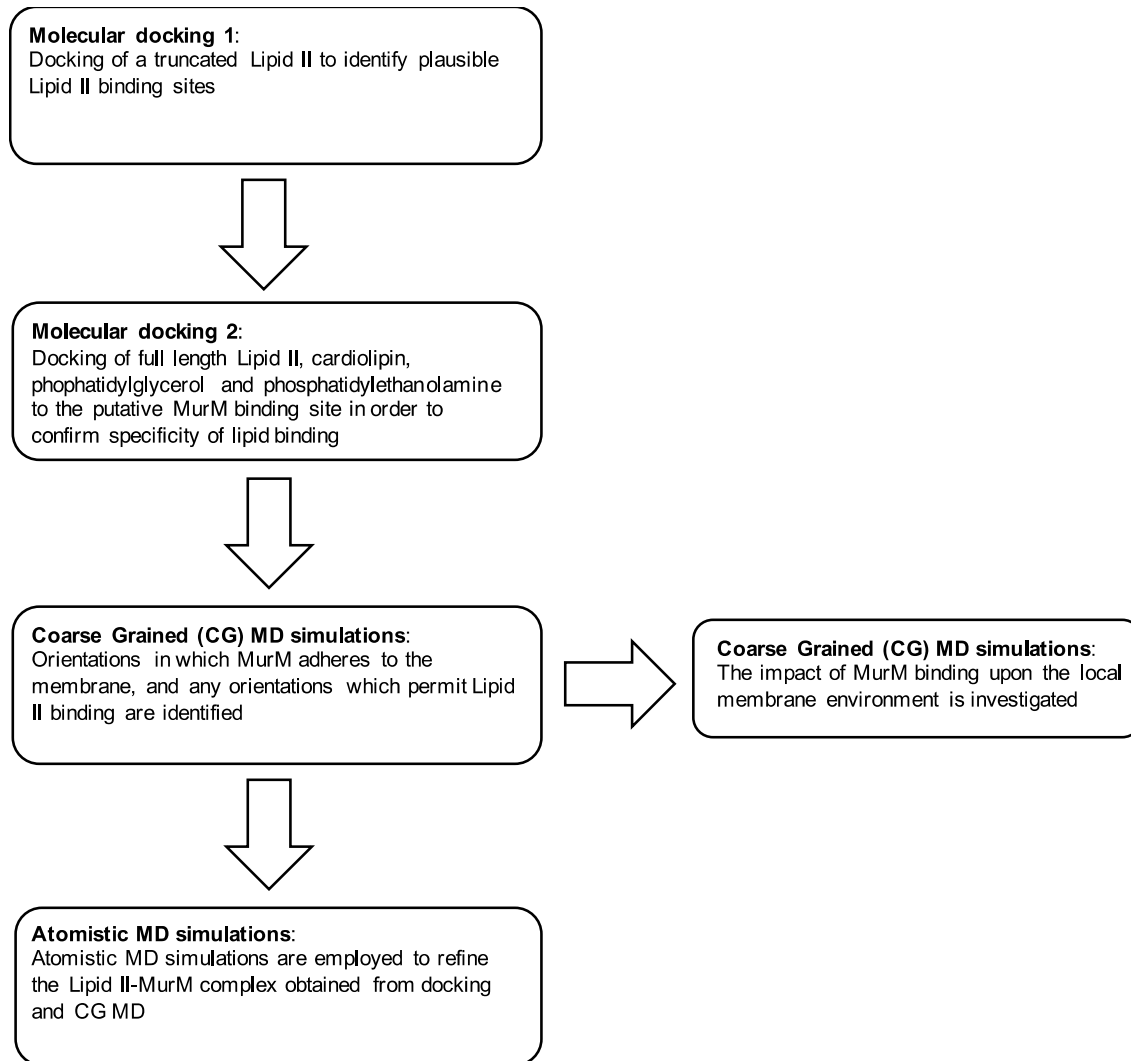


Figure S7. Flow chart showing the logistics of the computational studies

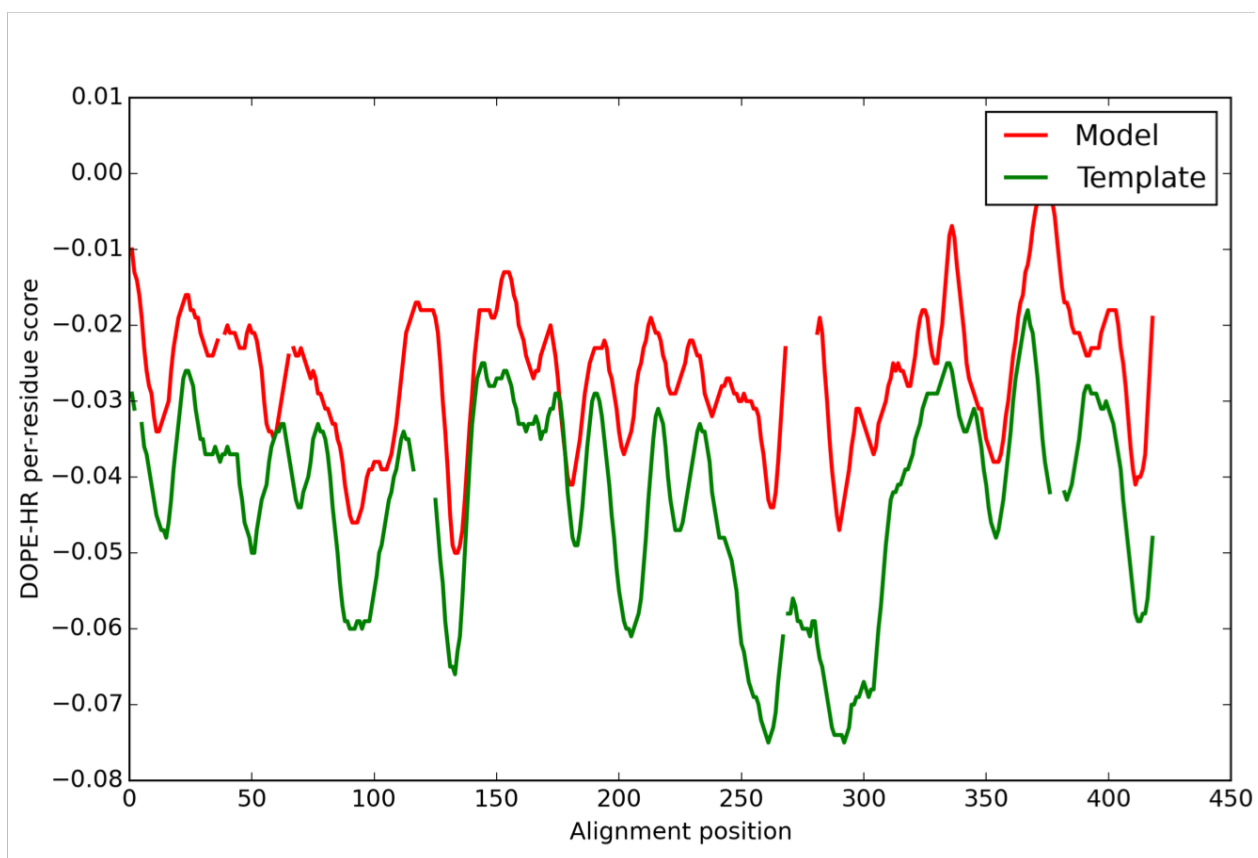


Figure S8. Discrete Optimized Protein Energy Profile for MurM and FemX. Comparison of DOPE-HR profiles for MurM model (red) and FemX template (green).



Full wwPDB X-ray Structure Validation Report ⓘ

Aug 27, 2019 – 02:41 pm BST

PDB ID : 6SNR
Title : Crystal structure of FemX
Deposited on : 2019-08-27
Resolution : 1.62 Å(reported)

This is a Full wwPDB X-ray Structure Validation Report.

This report is produced by the wwPDB biocuration pipeline after annotation of the structure.

We welcome your comments at validation@mail.wwpdb.org

A user guide is available at

<https://www.wwpdb.org/validation/2017/XrayValidationReportHelp>

with specific help available everywhere you see the ⓘ symbol.

The following versions of software and data (see [references ⓘ](#)) were used in the production of this report:

MolProbity : 4.02b-467
Xtriage (Phenix) : 1.13
EDS : 2.4
Percentile statistics : 20171227.v01 (using entries in the PDB archive December 27th 2017)
Refmac : 5.8.0158
CCP4 : 7.0 (Gargrove)
Ideal geometry (proteins) : Engh & Huber (2001)
Ideal geometry (DNA, RNA) : Parkinson et al. (1996)
Validation Pipeline (wwPDB-VP) : 2.4

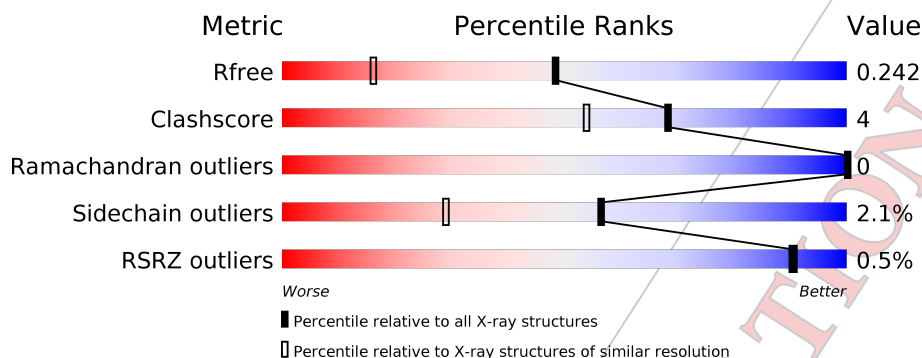
1 Overall quality at a glance ⓘ

The following experimental techniques were used to determine the structure:

X-RAY DIFFRACTION

The reported resolution of this entry is 1.62 Å.

Percentile scores (ranging between 0-100) for global validation metrics of the entry are shown in the following graphic. The table shows the number of entries on which the scores are based.



Metric	Whole archive (#Entries)	Similar resolution (#Entries, resolution range(Å))
R_{free}	111664	3975 (1.64-1.60)
Clashscore	122126	4258 (1.64-1.60)
Ramachandran outliers	120053	4162 (1.64-1.60)
Sidechain outliers	120020	4161 (1.64-1.60)
RSRZ outliers	108989	3894 (1.64-1.60)

The table below summarises the geometric issues observed across the polymeric chains and their fit to the electron density. The red, orange, yellow and green segments on the lower bar indicate the fraction of residues that contain outliers for ≥ 3 , 2, 1 and 0 types of geometric quality criteria. A grey segment represents the fraction of residues that are not modelled. The numeric value for each fraction is indicated below the corresponding segment, with a dot representing fractions $\leq 5\%$. The upper red bar (where present) indicates the fraction of residues that have poor fit to the electron density. The numeric value is given above the bar.

Mol	Chain	Length	Quality of chain
1	A	420	

2 Entry composition [i](#)

There are 2 unique types of molecules in this entry. The entry contains 3397 atoms, of which 0 are hydrogens and 0 are deuteriums.

In the tables below, the ZeroOcc column contains the number of atoms modelled with zero occupancy, the AltConf column contains the number of residues with at least one atom in alternate conformation and the Trace column contains the number of residues modelled with at most 2 atoms.

- Molecule 1 is a protein called Lipid II:glycine glycytransferase.

Mol	Chain	Residues	Atoms					ZeroOcc	AltConf	Trace
			Total	C	N	O	S			
1	A	402	3220	2039	554	615	12	0	0	0

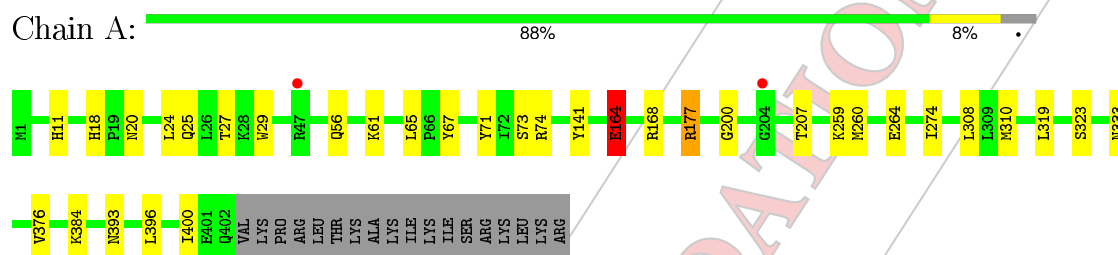
- Molecule 2 is water.

Mol	Chain	Residues	Atoms		ZeroOcc	AltConf
2	A	177	Total	O	0	0
			177	177		

3 Residue-property plots

These plots are drawn for all protein, RNA and DNA chains in the entry. The first graphic for a chain summarises the proportions of the various outlier classes displayed in the second graphic. The second graphic shows the sequence view annotated by issues in geometry and electron density. Residues are color-coded according to the number of geometric quality criteria for which they contain at least one outlier: green = 0, yellow = 1, orange = 2 and red = 3 or more. A red dot above a residue indicates a poor fit to the electron density ($RSRZ > 2$). Stretches of 2 or more consecutive residues without any outlier are shown as a green connector. Residues present in the sample, but not in the model, are shown in grey.

- Molecule 1: Lipid II:glycine glycytransferase



4 Data and refinement statistics

Property	Value	Source
Space group	P 21 21 21	Depositor
Cell constants a, b, c, α , β , γ	45.01Å 83.62Å 133.93Å 90.00° 90.00° 90.00°	Depositor
Resolution (Å)	52.27 – 1.62 52.27 – 1.62	Depositor EDS
% Data completeness (in resolution range)	99.7 (52.27-1.62) 99.7 (52.27-1.62)	Depositor EDS
R_{merge}	0.07	Depositor
R_{sym}	0.07	Depositor
$\langle I/\sigma(I) \rangle$ ¹	2.48 (at 1.62Å)	Xtriage
Refinement program	REFMAC 5.7.0032	Depositor
R, R_{free}	0.221 , 0.237 0.224 , 0.242	Depositor DCC
R_{free} test set	3294 reflections (5.07%)	wwPDB-VP
Wilson B-factor (Å ²)	20.7	Xtriage
Anisotropy	0.451	Xtriage
Bulk solvent k_{sol} (e/Å ³), B_{sol} (Å ²)	0.32 , 37.6	EDS
L-test for twinning ²	$\langle L \rangle = 0.43$, $\langle L^2 \rangle = 0.26$	Xtriage
Estimated twinning fraction	No twinning to report.	Xtriage
F_o, F_c correlation	0.94	EDS
Total number of atoms	3397	wwPDB-VP
Average B, all atoms (Å ²)	26.0	wwPDB-VP

Xtriage's analysis on translational NCS is as follows: *The largest off-origin peak in the Patterson function is 5.02% of the height of the origin peak. No significant pseudotranslation is detected.*

¹ Intensities estimated from amplitudes.

² Theoretical values of $\langle |L| \rangle$, $\langle L^2 \rangle$ for acentric reflections are 0.5, 0.333 respectively for untwinned datasets, and 0.375, 0.2 for perfectly twinned datasets.

5 Model quality [i](#)

5.1 Standard geometry [i](#)

The Z score for a bond length (or angle) is the number of standard deviations the observed value is removed from the expected value. A bond length (or angle) with $|Z| > 5$ is considered an outlier worth inspection. RMSZ is the root-mean-square of all Z scores of the bond lengths (or angles).

Mol	Chain	Bond lengths		Bond angles	
		RMSZ	$\# Z > 5$	RMSZ	$\# Z > 5$
1	A	0.68	2/3285 (0.1%)	0.84	4/4425 (0.1%)

All (2) bond length outliers are listed below:

Mol	Chain	Res	Type	Atoms	Z	Observed(Å)	Ideal(Å)
1	A	164	GLU	CD-OE2	5.91	1.32	1.25
1	A	164	GLU	CD-OE1	-5.20	1.20	1.25

All (4) bond angle outliers are listed below:

Mol	Chain	Res	Type	Atoms	Z	Observed(°)	Ideal(°)
1	A	177	ARG	NE-CZ-NH2	7.18	123.89	120.30
1	A	74	ARG	NE-CZ-NH2	-6.50	117.05	120.30
1	A	177	ARG	NE-CZ-NH1	-5.38	117.61	120.30
1	A	168	ARG	NE-CZ-NH1	5.37	122.98	120.30

There are no chirality outliers.

There are no planarity outliers.

5.2 Too-close contacts [i](#)

In the following table, the Non-H and H(model) columns list the number of non-hydrogen atoms and hydrogen atoms in the chain respectively. The H(added) column lists the number of hydrogen atoms added and optimized by MolProbity. The Clashes column lists the number of clashes within the asymmetric unit, whereas Symm-Clashes lists symmetry related clashes.

Mol	Chain	Non-H	H(model)	H(added)	Clashes	Symm-Clashes
1	A	3220	0	3146	26	0
2	A	177	0	0	2	0
All	All	3397	0	3146	26	0

The all-atom clashscore is defined as the number of clashes found per 1000 atoms (including hydrogen atoms). The all-atom clashscore for this structure is 4.

All (26) close contacts within the same asymmetric unit are listed below, sorted by their clash magnitude.

Atom-1	Atom-2	Interatomic distance (Å)	Clash overlap (Å)
1:A:67:TYR:CZ	1:A:396:LEU:HD11	2.06	0.91
1:A:18:HIS:HD2	1:A:20:ASN:H	1.20	0.86
1:A:25:GLN:HE22	1:A:56:GLN:H	1.28	0.82
1:A:67:TYR:CE1	1:A:396:LEU:HD11	2.25	0.72
1:A:67:TYR:CZ	1:A:396:LEU:CD1	2.73	0.71
1:A:308:LEU:HB3	1:A:310:MET:HE3	1.75	0.69
1:A:27:THR:HA	1:A:56:GLN:HE22	1.58	0.67
1:A:18:HIS:CD2	1:A:20:ASN:H	2.10	0.65
1:A:65:LEU:HD22	1:A:400:ILE:HD11	1.79	0.63
1:A:11:HIS:HE1	1:A:25:GLN:O	1.81	0.63
1:A:308:LEU:HB3	1:A:310:MET:CE	2.29	0.62
1:A:164:GLU:HG3	1:A:376:VAL:HB	1.85	0.59
1:A:61:LYS:HD2	2:A:511:HOH:O	2.05	0.56
1:A:67:TYR:CE1	1:A:396:LEU:CD1	2.90	0.53
1:A:25:GLN:NE2	1:A:56:GLN:H	2.03	0.51
1:A:67:TYR:CE2	1:A:396:LEU:CD1	2.95	0.49
1:A:260:MET:HE1	1:A:274:ILE:HD12	1.93	0.48
1:A:200:GLY:HA3	1:A:207:THR:HG23	1.96	0.48
1:A:323:SER:HB3	1:A:333:ASN:HD21	1.81	0.45
1:A:164:GLU:HG2	1:A:376:VAL:HG12	1.97	0.45
1:A:24:LEU:HD22	1:A:29:TRP:CE2	2.53	0.44
1:A:260:MET:CE	1:A:274:ILE:HD12	2.48	0.44
1:A:200:GLY:HA3	1:A:207:THR:CG2	2.48	0.43
1:A:71:TYR:CE2	1:A:73:SER:HB3	2.54	0.43
1:A:11:HIS:HD2	2:A:636:HOH:O	2.01	0.43
1:A:393:ASN:CG	1:A:396:LEU:HD12	2.40	0.42

There are no symmetry-related clashes.

5.3 Torsion angles [i](#)

5.3.1 Protein backbone [i](#)

In the following table, the Percentiles column shows the percent Ramachandran outliers of the chain as a percentile score with respect to all X-ray entries followed by that with respect to entries of similar resolution.

The Analysed column shows the number of residues for which the backbone conformation was analysed, and the total number of residues.

Mol	Chain	Analysed	Favoured	Allowed	Outliers	Percentiles	
1	A	400/420 (95%)	392 (98%)	8 (2%)	0	100	100

There are no Ramachandran outliers to report.

5.3.2 Protein sidechains ⓘ

In the following table, the Percentiles column shows the percent sidechain outliers of the chain as a percentile score with respect to all X-ray entries followed by that with respect to entries of similar resolution.

The Analysed column shows the number of residues for which the sidechain conformation was analysed, and the total number of residues.

Mol	Chain	Analysed	Rotameric	Outliers	Percentiles	
1	A	335/362 (92%)	328 (98%)	7 (2%)	56	29

All (7) residues with a non-rotameric sidechain are listed below:

Mol	Chain	Res	Type
1	A	141	TYR
1	A	164	GLU
1	A	177	ARG
1	A	259	LYS
1	A	264	GLU
1	A	319	LEU
1	A	384	LYS

Some sidechains can be flipped to improve hydrogen bonding and reduce clashes. All (9) such sidechains are listed below:

Mol	Chain	Res	Type
1	A	11	HIS
1	A	18	HIS
1	A	25	GLN
1	A	56	GLN
1	A	244	GLN
1	A	271	GLN
1	A	325	ASN
1	A	333	ASN
1	A	402	GLN

5.3.3 RNA [i](#)

There are no RNA molecules in this entry.

5.4 Non-standard residues in protein, DNA, RNA chains [i](#)

There are no non-standard protein/DNA/RNA residues in this entry.

5.5 Carbohydrates [i](#)

There are no carbohydrates in this entry.

5.6 Ligand geometry [i](#)

There are no ligands in this entry.

5.7 Other polymers [i](#)

There are no such residues in this entry.

5.8 Polymer linkage issues [i](#)

There are no chain breaks in this entry.

6 Fit of model and data [i](#)

6.1 Protein, DNA and RNA chains [i](#)

In the following table, the column labelled '#RSRZ > 2' contains the number (and percentage) of RSRZ outliers, followed by percent RSRZ outliers for the chain as percentile scores relative to all X-ray entries and entries of similar resolution. The OWAB column contains the minimum, median, 95th percentile and maximum values of the occupancy-weighted average B-factor per residue. The column labelled 'Q < 0.9' lists the number of (and percentage) of residues with an average occupancy less than 0.9.

Mol	Chain	Analysed	<RSRZ>	#RSRZ > 2	OWAB(Å ²)	Q < 0.9
1	A	402/420 (95%)	-0.15	2 (0%) 90 90	15, 24, 41, 68	0

All (2) RSRZ outliers are listed below:

Mol	Chain	Res	Type	RSRZ
1	A	204	GLY	4.6
1	A	47	ARG	2.1

6.2 Non-standard residues in protein, DNA, RNA chains [i](#)

There are no non-standard protein/DNA/RNA residues in this entry.

6.3 Carbohydrates [i](#)

There are no carbohydrates in this entry.

6.4 Ligands [i](#)

There are no ligands in this entry.

6.5 Other polymers [i](#)

There are no such residues in this entry.



[Click here to access/download](#)

3D Molecular Models (.PDB, .PSE, .MOL, .MOL2)
SpMurM_Model.pdb

